A trapped-ion phonon laser and the detection of ultra-weak forces

Sebastian Knünz

München 2010

A trapped-ion phonon laser and the detection of ultra-weak forces

Sebastian Knünz

Dissertation
an der Fakultät der Physik
der Ludwig–Maximilians–Universität
München

vorgelegt von
Sebastian Knünz
aus München

München, den 13. 12. 2010

Erstgutachter: Prof. Dr. Theodor W. Hänsch
Zweitgutachter: Prof. Dr. Hermann E. Gaub
Tag der mündlichen Prüfung: 4. Februar 2011

Zusammenfassung

Im Rahmen der vorliegenden Dissertation wurde an einem einzelnen gespeicherten Ion ein mechanisches Analogon zu einem optischen Laser, ein sogenannter "Phononenlaser" demonstriert. Darüber hinaus konnte gezeigt werden, dass die Dynamik des oszillierenden Ions äußerst empfindlich auf elektrische Felder reagiert. Die Beobachtung von Phasensynchronisationseffekten ("injection locking") erlaubte es, kleinste Kräfte von nur 5 yN (yocto=10^{-24}) nachzuweisen. Die enorme Sensitivität dieses neuartigen Kraft- bzw. Felddetektors verspricht erstmalig den Kernspin eines einzelnen Atoms bzw. Moleküls nachweisen zu können.

Im Experiment wurde die Bewegung eines in einer Radiofrequenz-Ionenfalle gefangenen Magnesium Ions von einem relativ zu einem atomaren Übergang blauverstimmten Laser verstärkt, und von einem zweiten, rotverstimmten Laser gedämpft. In einem gewissen Parameterbereich beginnt das Ion aus dem Rauschen heraus zu oszillieren. Diese Oszillation ist aufgrund der Sättigung der Kräfte auf das Ion stabil und wird ähnlich wie bei einem Laser, durch die kontinuierliche stimulierte Erzeugung weiterer Phononen aufrechterhalten. Die Einfachheit dieses Systems erlaubt eine genaue theoretische Beschreibung die sehr gut mit unseren Beobachtungen übereinstimmt. Damit haben wir zum ersten Mal ein mechanisches Analogon zu einem optischen Laser demonstriert, einen Phononenlaser.

Dieser Einzel-Ionen Phononenlaser emittiert keine Phononen. Um das System dennoch kohärent mit der Außenwelt zu verbinden, haben wir die Phasensynchronisation mit einem externen Signal untersucht. Dieses als "Injection locking" bekannte Phänomen besitzt viele Anwendungen, unter anderem wird es zur Übertragung von Stabilität bei optischen Lasern verwendet. Mit von uns entwickelten Techniken ist es möglich, diesen Oszillator sehr genau zu untersuchen. So erhalten wir Bewegungsspektren mittels einer Methode zur räumlich aufgelösten Fourier-Analyse der Ankunftszeiten der Fluoreszenzphotonen des Ions und analysieren die Phase zwischen dem injizierten Signal und dem oszillierenden Ion durch stroboskopische Abbildung. In beiden Fällen beobachten wir sehr gute Übereinstimmung zwischen Experiment und Theorie, und erhalten einen faszinierenden Einblick in die zugrundeliegenden Mechanismen.

Die Kräfte, die diese Phasensynchronisation bewirken sind sehr klein. Zum Vergleich: die kleinste von uns beobachtete Kraft von 5 yN würde das Ion nur um etwa einen Nanometer auslenken. Das ist 2000 mal weniger als das Auflösungsvermögen unserer Optik oder als die Ausdehnung der thermischen Bewegung des Ions. Daher denken wir, dass dieses System als hochempfindlicher Kraftdetektor verwendet werden könnte. Vorstellbar wäre unter anderem der Nachweis des Kernspins eines einzelnen Ions.

Abstract

This dissertation reports on the demonstration of a mechanical analogue to an optical laser, a "phonon laser", using a single trapped ion. Furthermore, we show that the dynamics of this system are surprisingly sensitive to external fields; we demonstrate phase synchronization ("injection locking") to an external signal by applying forces as weak as 5 yN (yocto=10^{-24}). This enormous sensitivity might allow the detection of the nuclear spin of a single atom or molecule.

A single magnesium ion is trapped in a linear radio-frequency ion trap and illuminated by two laser beams. One is tuned slightly above an atomic transition, blue-detuned, and amplifies an existing motion. A second, red-detuned laser beam damps the motion. For certain parameters, the ion starts to oscillate from noise. The forces on the ion saturate, so it oscillates with a stable amplitude. This oscillation is sustained by the stimulated generation of phonons similar to an optical laser. The simplicity of this system allows an in-depth theoretical description which precisely matches our observations. Thus, we report on the first mechanical analogue to an optical laser, a trapped-ion phonon laser.

In contrast to an optical laser, our single trapped-ion phonon laser does not emit phonons. In order to coherently manipulate this system from outside, we demonstrate phase synchronization, also known as injection locking, to an external signal. This is a technologically important phenomenon, e.g., used to transfer stability in optical lasers. We have developed two techniques to investigate the injection locking dynamics: We analyze the motional spectrum of the ion with a spatially selective Fourier transform method and retrieve the phase between the injected signal and the oscillator using stroboscopic imaging. In both cases we find excellent agreement between theory and experiment, and obtain unique insight into the underlying mechanisms.

The forces which induce phase synchronization are minute–the smallest force we observed is 5 yN. In comparison: This displaces the ion by one nanometer only, which is 2000 times less than the resolution of our imaging system or the extent of the thermal motion of the ion. Therefore, we conclude that this system appears promising for the detection of ultra-weak forces. Conceivable would be the detection of nuclear spin flips of a single trapped atomic or molecular ion.

Contents

Introduction xi

1. Basic technologies 1
1.1. Linear radio frequency traps . . . 1
1.1.1. Radial confinement . . . 2
1.1.2. Axial confinement . . . 5
1.2. Laser cooling . . . 5

2. Experimental setup and evaluation tools 9
2.1. Ion traps . . . 10
2.1.1. The ”endcap trap” . . . 10
2.1.2. The ”4-rod trap” . . . 11
2.1.3. Electronics . . . 16
2.1.4. Vacuum system and other components . . . 18
2.2. Laser systems . . . 19
2.2.1. Photo ionization lasers . . . 19
2.2.2. Cooling/gain laser systems . . . 20
2.2.3. A simple but stable reference cavity . . . 21
2.3. Fluorescence detection and analysis . . . 26
2.3.1. Imaging system . . . 26
2.3.2. Position sensitive camera readout . . . 28
2.3.3. Phase sensitive (stroboscopic) camera readout . . . 28
2.4. Data acquisition and evaluation . . . 29
2.4.1. DAQ system . . . 29
2.4.2. Data analysis software suite . . . 31

3. A trapped-ion phonon laser 33
3.1. Theory . . . 34
3.1.1. One laser . . . 34
3.1.2. Two lasers . . . 36
3.1.3. Dynamical regimes . . . 37
3.1.4. Domain $\mathcal{A}$ . . . 37
3.1.5. Domain $\mathcal{B}$ . . . 39
3.2. Thermal distribution . . . 39

3.3. Observation of laser-driven ion oscillations . . . 43
3.3.1. Experimental procedures . . . 43
3.3.2. Experimental data . . . 43
3.3.3. Hysteresis . . . 45
3.4. A trapped-ion phonon laser . . . 46

4. Injection locking and the detection of ultra-weak forces 51
4.1. Injection locking of a trapped-ion phonon laser . . . 51
4.1.1. General theory of injection locking . . . 51
4.1.2. Theory of injection locking of a trapped-ion phonon laser . . . 54
4.1.3. Experimental procedures . . . 57
4.1.4. Oscillation spectra . . . 58
4.1.5. Phase analysis of the ion's motion . . . 60
4.2. Force detection . . . 63
4.2.1. Force calibration . . . 63
4.2.2. Detecting the weakest forces . . . 64
4.2.3. Measurement of ultraweak forces . . . 67

5. Outlook 69
5.1. Detection of nuclear spin flips of a single charged particle . . . 69
5.2. Conclusions . . . 72

A. Fundamental constants and Magnesium data 75

B. Mass spectrometry with a trapped-ion phonon laser 77

C. Electronics and software 79
C.1. Position discriminator . . . 79
C.2. Bias-tee . . . 80
C.3. Camera readout software . . . 81
C.4. Measurement software . . . 81

Bibliography I

Introduction

The possibility to study a single ion or atom has long been a mesmerizing goal for physics. However, only since the last century this dream has become reality. Apart from the aesthetic and philosophical aspects, a single trapped ion constitutes a very pure representation of a harmonic oscillator and allows to measure the internal atomic structure to unprecedented precision.

While much attention has been paid to spectroscopy of electronic transitions, e.g. for optical atomic clocks, also the motional dynamics find important applications. By addressing an atomic transition, e.g. by optical lasers, such a single trapped-ion harmonic oscillator can be exactly controlled from the outside. For example, single motional quanta of groundstate cooled ions are used as a bus system in quantum logic operations which gave rise to quantum simulations, state of the art optical clocks, and might enable quantum computation.

Apart from that, advances in the development of gravitational wave detectors and in microfabrication have renewed interest in the interaction of mechanical motion and light. This gave rise to a rich field of experiments with micromechanical oscillators such as cantilevers, toroids or nanospheres. Here techniques that have been developed for the manipulation of trapped ions are employed to control these much larger and complex oscillators. In this context, a single trapped ion constitutes a simple, lightweight, isolated, and well controllable toy system.

In this work, we consider a single trapped Mg^+ ion as an essentially ideal harmonic oscillator and demonstrate a mechanical analogue to an optical laser, a phonon laser. We illuminate the ion with two laser beams: a blue-detuned laser which amplifies an existing motion, and a second, red-detuned laser which provides damping. For a certain set of parameters, regenerative oscillations start from noise. The laser powers transfered to the ion saturate and give rise to stable oscillations which are sustained by stimulated generation of motional quanta, phonons. Based on the simplicity of the system we are able to formulate a theory which perfectly matches our observations. We conclude that this system constitutes a mechanical analogue to an optical laser, a phonon laser. Note that rather than simply heating, a blue-detuned laser can give rise to rich dynamics.

Our phonon laser differs from its optical counterpart in that it does not emit phonons. We therefore studied techniques to coherently manipulate this system from outside. To this end, we investigated the phase synchronization behavior when the phonon laser is exposed to an auxiliary signal. Most likely Christiaan Huygens could not imagine injection locking of the motion of a single ion when he first observed this

phase synchronization phenomenon in neighboring mechanical clocks back in 1665. In fact, injection locking plays an important role in nature as well as in science and technology. In the field of optical laser technology, for example, it has become a standard technique to transfer laser stability. In our case, the external signal is a weak rf signal which slightly tickles the ion's motion. If its frequency is close enough to the free-running frequency of the ion, the oscillator phase synchronizes with the injected signal. We have developed two measurement techniques: a spatially selective Fourier analysis method to study the oscillator spectrum, and stroboscopic imaging to obtain the phase between the injected signal and the ion oscillator. In both cases, we find excellent agreement with injection locking theory in and outside the locking range and observe effects like frequency and phase pulling of the oscillator close to the locking range.

The fields and forces necessary to injection lock the motion of a single trapped ion are very small. We detected forces as small as $5(1) \cdot 10^{-24}$ N (10^{-24} =yocto). Only ten times larger than the force of gravity on a single Mg atom at Earth's surface, this force displaces our trapped ion by merely 1 nm from the trap center. This is 2000 times less than the resolution of our imaging system or the thermal distribution of the ion. Compared to other force detectors, this novel, atomic scale force sensor may not be the most sensitive but it is nondestructive, isolated, located, and well controllable. What could we use it for, specifically? Our idea is to detect nuclear spin flips of a single trapped ion by the force on it in an inhomogeneous magnetic field. This could be an independent measurement apart from the detection e.g. via shelving of the hyperfine structure or in large ensembles.

Organization of this thesis

This thesis is organized in five chapters. In the **first chapter**, we introduce the fundamentals of ion trapping. Then, we outline our apparatus, data acquisition, and evaluation tools in the **second chapter**. We present experimental results on our trapped-ion phonon laser in the **third chapter**, on injection locking of this system and the detection of ultra-weak forces in the **fourth chapter**, and discuss possible applications and improvements in the **fifth chapter**.

Work on precision spectroscopy

Besides the work presented in this thesis, the author also contributed to another project, the precision spectroscopy of weakly bound ions. This work is covered in the publications listed below ([1, 2]) and in [3].

Manuscripts in peer-reviewed journals

- **Injection locking of a trapped-ion phonon laser** [4]
  S. Knünz, M. Herrmann, V. Batteiger, G. Saathoff, T.W. Hänsch, K. Vahala and Th. Udem
  Physical Review Letters **105**, 013004 (2010) (selected as editor's suggestion)
  Press release by the Max Planck Institute of Quantum Optics for this publication
  http://www.mpq.mpg.de/cms/mpq/en/news/press/10_08_04.html

- **A phonon laser** [5]
  K. Vahala, M. Herrmann, S. Knünz, V. Batteiger, G. Saathoff, T.W. Hänsch and Th. Udem
  Nature Physics **5**, 682 (2009)
  Press release by the Max Planck Institute of Quantum Optics for this publication
  http://www.mpq.mpg.de/cms/mpq/en/news/press/archiv/2009/09_08_25.html

- **Precision spectroscopy of the 3s-3p fine structure doublet in Mg^+** [1]
  V. Batteiger, S. Knünz, M. Herrmann, G. Saathoff, H.A. Schüssler, B. Bernhardt, T. Wilken, R. Holzwarth, T.W. Hänsch and Th. Udem
  Physical Review A **80**, 022503 (2009)

- **Feasibility of coherent xuv spectroscopy on the 1s-2s transition in singly ionized helium** [6]
  M. Herrmann, M. Haas, U.D. Jentschura, F. Kottmann, D. Leibfried, G. Saathoff, C. Gohle, A. Ozawa, V. Batteiger, S. Knünz, N. Kolachevsky, H.A. Schüssler, T.W. Hänsch and Th. Udem
  Physical Review A **79**, 052505 (2009)

- **Frequency metrology on single trapped ions in the weak binding limit: The $3s_{1/2} - 3p_{3/2}$ transition in $^{24}Mg^+$** [2]
  M. Herrmann, V. Batteiger, S. Knünz, G. Saathoff, Th. Udem and T.W. Hänsch
  Physical Review Letters **102**, 013006 (2009)

1. Basic technologies

Based on quadrupole mass filter technology used in particle physics, Wolfgang Paul and others have developed the radio frequency ion trap or Paul trap in the 50's of the past century [7]. They showed that ions can be stored with appropriate oscillating electric quadrupole fields. The trapping potentials here can have depths equivalent to an ion temperature of $\sim 50'000$ K. This enormous trap depth is due to the fact that the method makes use of the electric charge of the atom which is orders of magnitude larger than for neutral atom traps e.g. the magnetic moment. Placed in a vacuum chamber, unperturbed by the environment in a minimum of the electric and magnetic field, ion traps allow to store millions as well as single ions. These developments cumulated in the Nobel Prize in physics 1989 for W. Paul and Hans G. Dehmelt [8]. The second basic technology employed in this work, laser cooling, has been proposed simultaneously for atoms by Theodor W. Hänsch [9] and for ions by David J. Wineland [10]. This technique, demonstrated shortly afterwards [11, 12], allowed to drastically reduce the kinetic energy of the trapped ions. Further improvements of the cooling techniques allowed to reach the motional ground state [13]. This paved the way for many applications like quantum computation [14], quantum simulation [15], and optical clocks [16].

Excellent and rather complete overviews on ion trapping and (laser)-cooling methods are given in [17] and [18]. In this chapter, we review some of the most relevant features.

1.1. Linear radio frequency traps

Radio frequency ion trapping relies on the nonlinearity of electric multipole fields. The oscillating fields do not average to zero but generate an effective, time-averaged potential. For a characteristic range of parameters this implies an average force towards the trapping center which confines charged particles in the central, field-free region. In the case of a Paul trap this rapidly oscillating field is quadrupolar (Fig. 1.1) and the potential reads

$$\phi(x, y, z) = \frac{1}{2}(U_{dc} + U_{rf}\cos(\Omega t))(\alpha x^2 + \beta y^2 + \gamma z^2) \tag{1.1}$$

with the amplitude U_{rf} and the frequency Ω of the rf field, and the static dc quadrupolar field component U_{dc}. In order to satisfy the Laplace equation $\Delta\phi = 0$,

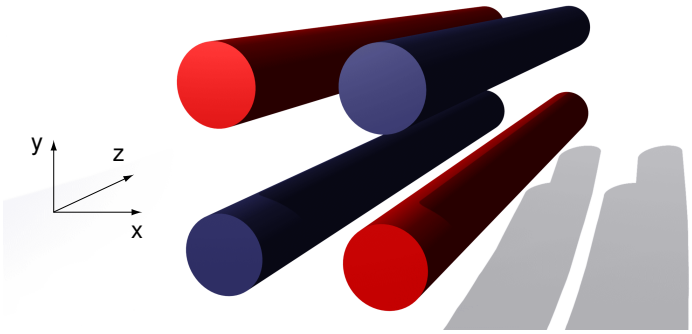

Figure 1.1.: Sketch of a linear Paul trap. Opposing rods are on equal potential.

the following restrictions are imposed on α, β and γ

$$\alpha + \beta + \gamma = 0. \tag{1.2}$$

In the following we restrict our discussion to linear traps which do not confine in z-direction. Therefore, $\gamma = 0$ and $\alpha = -\beta$. Inserting the potential into Newton's equation, we obtain the equations of motion for a trapped particle of charge Q and mass m

$$\ddot{x} = -\frac{Q}{m}\frac{\partial \phi}{\partial x} = -\frac{\alpha Q}{m}(U_{dc} + U_{rf}\cos(\Omega t))\ x \tag{1.3}$$

$$\ddot{y} = -\frac{Q}{m}\frac{\partial \phi}{\partial y} = \frac{\alpha Q}{m}(U_{dc} + U_{rf}\cos(\Omega t))\ y \tag{1.4}$$

$$\ddot{z} = -\frac{Q}{m}\frac{\partial \phi}{\partial z} = 0. \tag{1.5}$$

The ion's motion in radial direction (Eqs. 1.3 and 1.4) depends on several parameters while the motion in z-direction (Eq. 1.5) is not restricted. The parameter α reads $\alpha = \kappa/2r_0^2$ where r_0 denotes the distance from the trap center to the electrode surfaces and κ is a geometry factor which is 1 for hyperbolic electrodes and decreases as the electrode structure deviates from the ideal equipotential hyperbolic shape (Sec. 2.1.2). Note that decreasing κ implies an increase of the anharmonicity of the potential. Since hyperbolic electrodes do not allow for a good access to the trapping zone, four-rod electrode structures (Fig. 1.1) are frequently used in ion trap designs. They constitute a tradeoff between low anharmonicities/large κ [19] and good optical access.

1.1.1. Radial confinement

By introducing the following dimensionless parameters a, q and ξ

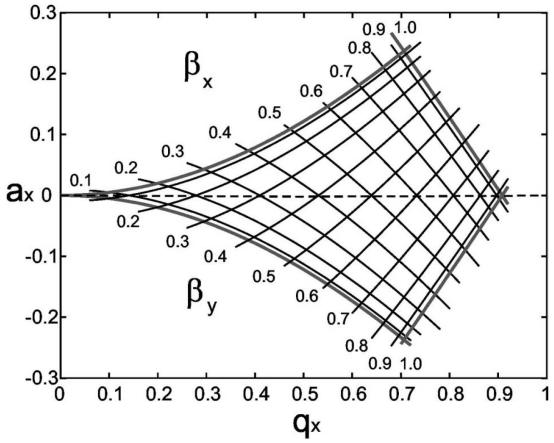

Figure 1.2.: Stability diagram of a linear ion trap in radial direction taken from [17]. The stability region has the following corners: (a, q)=(0, 0), (±0.237, 0.706) and (0, 0.908).

$$a_x = -a_y = a := \frac{4\kappa Q U_{dc}}{m\Omega^2 r_0^2} \qquad q_x = -q_y = q := \frac{2\kappa Q U_{rf}}{m\Omega^2 r_0^2} \qquad \xi := \frac{\Omega t}{2} \tag{1.6}$$

the decoupled equations of motion in the radial direction can be transformed to a so-called Mathieu equation [7]:

$$m\frac{d^2\rho}{d\xi^2} + (a_i - 2q_i \cos 2\xi)\rho = 0 \qquad \rho \in \{x, y\}. \tag{1.7}$$

Since the coefficients of this differential equation are periodic, the Floquet theorem gives the following general solution

$$\rho(\xi) = Ae^{i\beta_\rho \xi} \sum_{n=-\infty}^{\infty} C_{2n} e^{i2n\xi} + Be^{-i\beta_\rho \xi} \sum_{n=-\infty}^{\infty} C_{2n} e^{-i2n\xi}. \tag{1.8}$$

Here β is the so-called "Mathieu characteristic exponent" and the C_{2n} can be obtained in a recursion expansion by substituting the solution into the Mathieu equation (Eq. 1.7). These C_{2n} depend on a and q only, while A and B incorporate the initial conditions. In order to obtain finite solutions, hence stable ion trajectories, we require that $\beta \in]0, 1[$. This is fulfilled for an infinite number of regions in the a, q-plane. Figure 1.2 shows the region containing $a, q = 0$ commonly used in ion trapping. Assuming $a = 0$, stable trajectories exist for $q \in]0, 0.908]$.

For $(|a|, q^2) \ll 1$, the Mathieu exponent can be approximated as

$$\beta \cong \sqrt{a + q^2/2}. \tag{1.9}$$

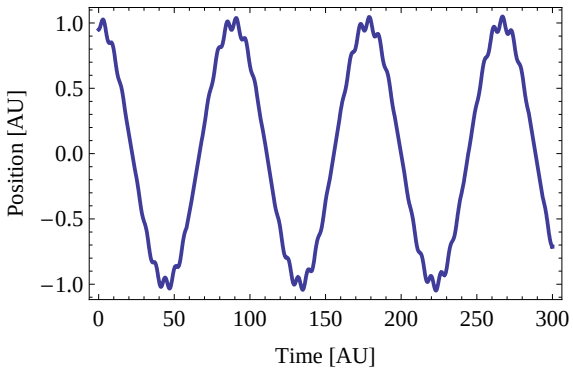

Figure 1.3.: Ion motion (Eq. 1.11) for $a = 0$ and $q = 0.1$. The faster micromotion is superimposed on the slower secular motion.

With this the general solution (Eq. 1.8) can be simplified to

$$\rho(t) = \rho_0[1 - \frac{q}{2}\cos(\Omega t)]\cos(\omega_r t) \tag{1.10}$$

with the so-called "secular frequency"

$$\omega_r = \frac{1}{2}\beta\Omega = \frac{1}{2}\sqrt{a + q^2/2}\ \Omega. \tag{1.11}$$

The motion of a trapped particle according to Eq. 1.10 for $a = 0$ and $q = 0.1$ is plotted in Fig. 1.3. The ion oscillates with a frequency ω_r, the "secular motion", which is superimposed by a faster, so-called "micromotion" at the trap frequency Ω. Throughout this work $a \approx 0$, thus the secular frequency can be written as

$$\omega_r \approx \frac{q\Omega}{\sqrt{8}}. \tag{1.12}$$

These results can be interpreted as the motion in a harmonic pseudo potential Φ [18, 20], generated by the rf field

$$\Phi = \frac{1}{2}m\omega_r^2 x^2. \tag{1.13}$$

The maximal kinetic energy an ion can have in this potential without touching the electrodes, the "trap depth", reads

$$D = \frac{1}{2}m\omega_r^2 r_0^2 = \frac{QqU_{rf}}{8}. \tag{1.14}$$

Usually trap depths are on the order of several eV corresponding to temperatures of several 10'000 K.

1.1.2. Axial confinement

The assumption that $\gamma = 0$, which has been made in the beginning of this section, holds only for electrodes of infinite length. In the case of finite electrode length, a residual oscillating quadrupolar field component in the axial direction has to be taken into account. If the field of the electrode structure is evaluated numerically, the axial component can be estimated quantitatively by comparing the axial and radial potentials [21] (Sec. 2.1). Usually this confinement is relatively weak and not independently tunable. Therefore, in most linear ion traps axial confinement is obtained by additional dc voltages U_{ax}, applied to neighboring electrodes, which repel the ion. The resulting axial potential is to first order harmonic, and the following equation holds [18]

$$\frac{1}{2}m\omega_z^2 z_0^2 = \kappa_z Q U_{ax}. \tag{1.15}$$

Here z_0 denotes the distance from the dc electrode to the trap center and κ_z a geometric factor depending on the electrode structure. In experiment, usually the following formula is utilized

$$\omega_z = k\sqrt{\frac{QU_{ax}}{m}} \tag{1.16}$$

where the constant k, which can be determined experimentally, incorporates the constant parameters. Note that in this case the axial oscillation frequency can be tuned independent from its radial counterpart by changing the voltage U_{ax}.

1.2. Laser cooling

The general idea in laser cooling is to reduce the kinetic energy of a particle by radiation pressure. If a laser interacts with an optical transition of an atom or ion (Fig. 1.4), two processes have to be considered: absorption of laser photons and spontaneous emission. For laser cooling, the laser is detuned such that absorption of laser photons is more likely to occur if the ion moves towards the laser (negative or "red"-detuning). Due to the Doppler shift, for an ion moving towards the red-detuned laser, the frequency of the laser is closer to resonance which implies a higher photon absorption probability. Consequently, the laser frequency is further off resonance for an ion moving away from it. Hence, the recoil kicks from the absorptions decelerate the ion on average. The atom in the excited state decays by spontaneous emission of a photon in random direction and therefore on average does not change the ion's momentum. Accordingly, together with the absorption, the total momentum change is negative, so the ion decelerates.

In contrast, if the laser is detuned to the blue side of the atomic transition, absorption is more likely when the ion is moving away from the laser, and the atom is

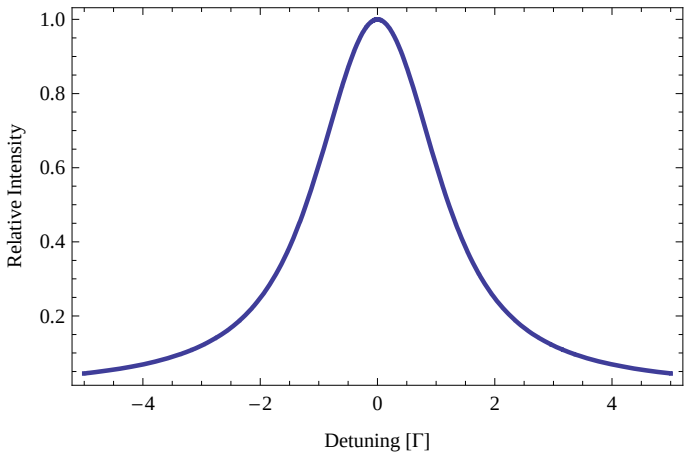

Figure 1.4.: Typical Voigt profile of an atomic transition. It is a convolution of a Lorentzian (due to the upper state lifetime) of width $\Gamma_L = \Gamma$ with a Gaussian (thermal contribution) of width Γ_G. Here, $\Gamma_G = \Gamma/2$.

accelerated. This is not advantageous for most applications but nonetheless can be of great interest as we report in Chapter 3.

To quantify the laser cooling dynamics of particles confined in a trap, two regimes need to be distinguished, that depend on the ratio of the transition linewidth Γ to the ion's secular frequency ω. Since the trapped ions are in motion, the absorption line profile, seen in the laboratory frame, is modulated by the ion's oscillation frequency, and sidebands at $\nu_{sb} = \nu_{transition} \pm n\omega/2\pi$ are generated. Two regimes are identified: First, when $\Gamma \ll \omega$, the sidebands are resolved, the "strong binding" regime [17]. With a (narrow) laser tuned on the sideband on the "red" side, the ion can be cooled to the motional ground state. This is because the sideband will disappear if the ion is in the motional ground state and stop scattering photons whose recoil could heat it up again. Second, if $\Gamma \gg \omega$, the regime of Doppler cooling or "weak binding" [17], the sidebands are not resolved and laser cooling is similar to Doppler cooling of free particles. If an ion hypothetically reaches the motional ground state, it will still scatter photons since the Voigt profile has a considerable absorption probability even at zero temperature (Fig. 1.4). Each spontaneous emission will add the energy of a photon recoil $\delta p = \hbar k$ to the ion. This process is a random walk in momentum space similar to Brownian motion. Therefore, this recoil energy constitutes a limit for the minimal temperature in this regime.

The notion "temperature" usually assumes the thermodynamic limit, i.e. an infinite number of particles. For a single particle/trapped ion this is to be understood in the following way: After laser cooling the ion populates the energy levels $E_n = (n + 1/2)\hbar\omega$ according to a thermal distribution. Thus, assuming the laser cooled ion is ergodic, a temperature can be assigned to the ion [22].

A feature of Doppler cooling we utilize is that an ion scatters enough photons to

be observed with an imaging system. All experiments presented in this thesis were conducted in this regime which we review in detail in the following.

Neglecting micromotion (Sec. 1.1.1), the ion, moving at a velocity $v = v_0 \cos(\omega t)$ in the direction of the wavevector $\vec{k}$ of the cooling laser, sees the detuning $\Delta = 2\pi(\nu_{laser} - \nu_{transition})$ modulated by the Doppler effect

$$\delta_{eff} = \Delta - \vec{k} \cdot \vec{v} = \Delta - k v_0 \cos(\omega t). \tag{1.17}$$

Photons are scattered at rate

$$g(s, \delta) = \frac{\Gamma s/2}{1 + s + (2\delta/\Gamma)^2} \tag{1.18}$$

where s is the saturation parameter which denotes the laser intensity in units of the saturation intensity [20]. This scattering induces an average force on the ion

$$\langle F \rangle_\omega = \langle \dot{p} \rangle_\omega = \langle \hbar k g(s, \delta) \rangle_\omega. \tag{1.19}$$

The heating or cooling power averaged over one oscillation cycle of the ion's secular motion therefore reads [23]

$$\langle P_a \rangle_\omega = \langle F v \rangle_\omega = \langle \hbar k g(s, \delta_{eff}(t)) v_0 \cos(\omega t) \rangle_\omega. \tag{1.20}$$

Spontaneous emission in contrast, on average, always implies an increase in motional energy by [17]

$$\langle P_s \rangle_\omega = \langle (1 + \xi) \frac{\hbar^2 k^2}{2m} g(s, \delta_{eff}(t)) \rangle_\omega. \tag{1.21}$$

Here $\xi = 2/5$ is a factor taking into account the emission pattern of the dipole radiation and m denotes the ion's mass. For the steady state cooling and heating balance, $P_a = P_s$, and the ion's temperature $T = m\langle v^2 \rangle / 2k_b$ can be calculated with $\langle v^2 \rangle = v_0^2/2$ for a harmonic oscillation. For small temperatures, a simple analytic expression can be found which reads [17]

$$T = \frac{\hbar \Gamma}{8 k_b} (1 + \xi) \left((1 + s) \frac{\Gamma}{2\Delta} + \frac{2\Delta}{\Gamma} \right). \tag{1.22}$$

Figure 1.5 shows an exemplary plot of this equation with $\Gamma = 2\pi \cdot 41.8$ MHz for $s \to 0$ and $s = 1$, while an experimental measurement is presented in Section 3.2. The minimal temperature is obtained for

$$\Delta = \Gamma \sqrt{1 + s}/2 \tag{1.23}$$

and reads

$$T_{min} = \frac{\hbar \Gamma (1 + \xi)}{4 k_b} \sqrt{1 + s} > \frac{7\hbar}{20 k_b} \Gamma. \tag{1.24}$$

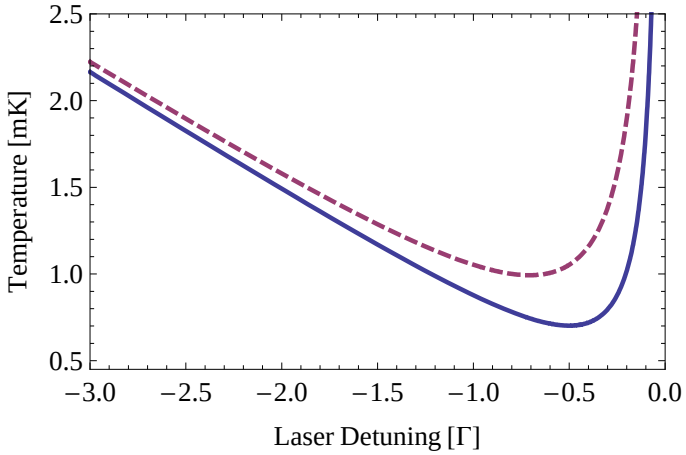

Figure 1.5.: Minimal (Doppler) temperature according to Eq. 1.22, for $\Gamma = 2\pi \cdot 41.8$ MHz ($^{24}Mg^{+}$ D2 cooling transition), $s \to 0$ (full), and $s = 1$ (dashed). For $s \to 0$ the minimal temperature is obtained for $\Gamma/2$ (Eq. 1.23).

It depends on the natural linewidth only. Typical values are on the order of mK. For the $^{24}Mg^{+}$ D2 transition ($3s_{1/2} - 3p_{3/2}$) used in this work (Appendix A), the Doppler limit is 0.7 mK ($\Gamma = 2\pi \cdot 41.8$ MHz [2]).

2. Experimental setup and evaluation tools

This chapter gives an overview of the experimental apparatus.

Figure 2.1 shows the basic building blocks of our experiment. Mg^+-ions are trapped in a linear ion trap which is integrated into an ultra-high vacuum (UHV) apparatus. UV light near 280 nm as required for cooling/manipulation of the ions is generated by a frequency-doubled dye laser or a quadrupled fiber laser. For metrology and improved control, the laser systems are stabilized to a reference cavity and monitored using a frequency comb. We observe our ions using a low-noise, high-resolution imaging system. Further, we use two laser systems at 285 nm for photoionization of neutral Mg atoms. The DAQ system as well as the data analysis software suite are introduced in the last section.

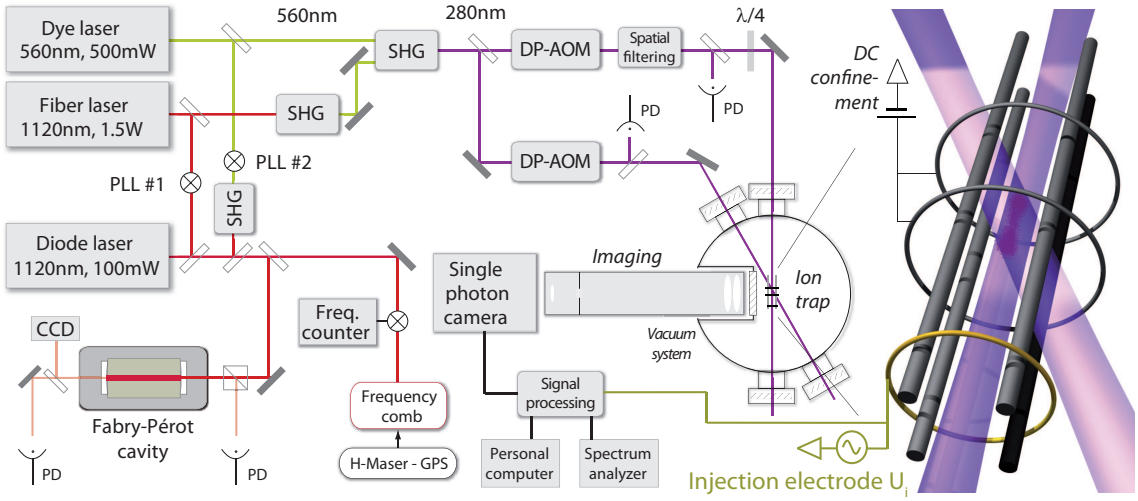

Figure 2.1.: Experimental setup. Using a frequency-doubled dye laser or a frequency-quadrupled fiber laser and double-pass AOMs, we generate two independently tunable UV laser beams near 280 nm, which address the cooling/manipulation transition of trapped Mg^+-ions. Both lasers are locked to a diode laser that is stabilized to a Fabry-Pérot cavity and referenced to a frequency comb. The ion trap is located in a UHV chamber. Axial confinement is generated with a DC voltage on two rings. An external rf-signal can be applied using a third ring electrode. The trapped ion is observed with a single-photon camera.

2.1. Ion traps

Two ion traps were used in this work. First, a segmented endcap trap, designed by M. Herrmann for precision spectroscopy of single He^+ ions [24] was used for the first phonon laser measurements (Chapter 3). The second, a 4-rod trap optimized for parameters more relevant for this work like tunable axial confinement, was used in the injection locking and force detection measurements (Chapter 4). Both traps were housed in the same vacuum system and equipped with similar rf electronics.

2.1.1. The "endcap trap"

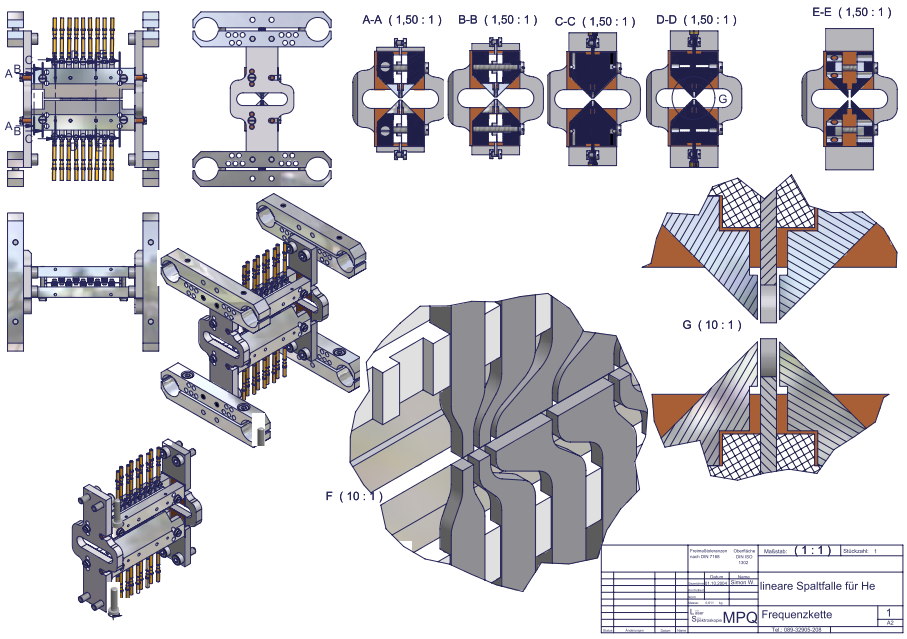

Figure 2.2.: Technical drawing of the endcap trap. The two outlines show the radial and the axial electrode structure.

The segmented endcap trap (Fig. 2.2) offers seven trapping zones and excellent optical access. The electrode structure in radial direction consists of six parts. Two rf-leading electrodes face each other in the middle while the usually two ground electrodes are split into four triangular parts in total and arranged close to the rf electrodes (compare to Fig. 1.1). With this trick we obtain a large angle for optical access of 90°. The rf electrodes are separated by 1 mm and therefore $r_0 = 0.5$ mm. Axially, the ground electrodes consist of one piece each, while the rf electrodes are divided into nine segments, each separated by 0.5 mm. The segment length is 1 mm for short and 5 mm for long ones. Each segment holds the same rf-voltage with an individual dc offset added for ion shuttling and axial confinement if the same dc

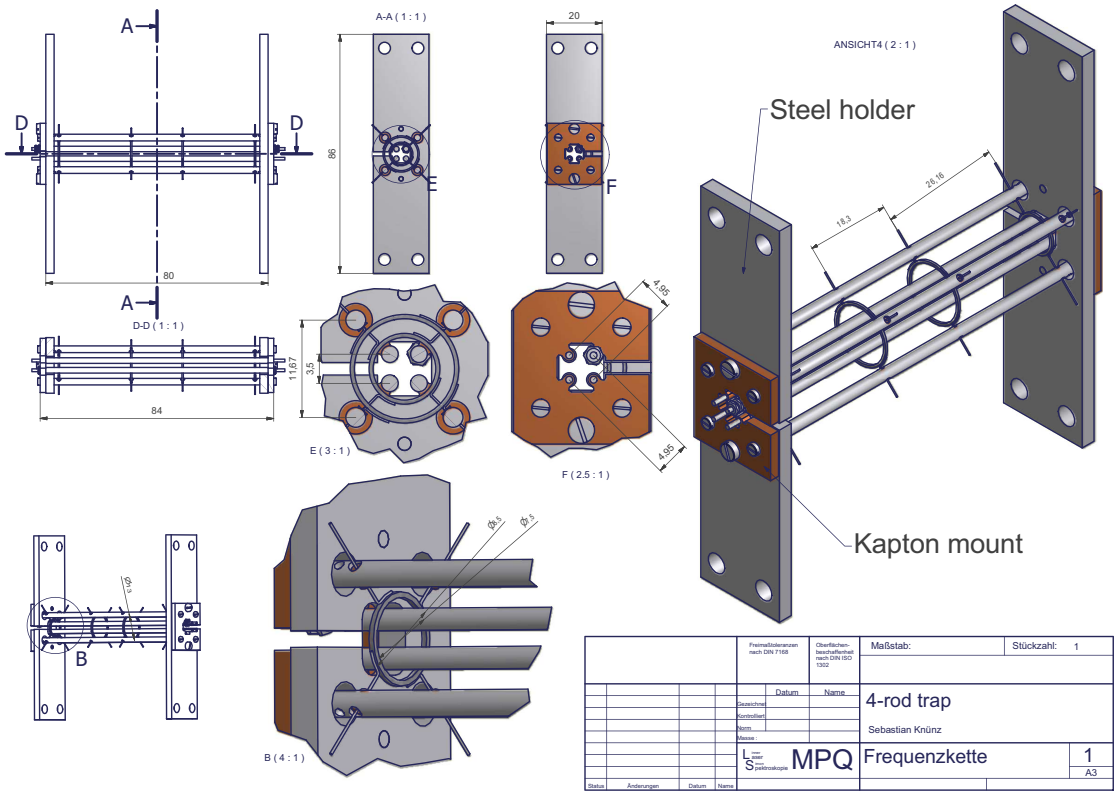

Figure 2.3.: Technical drawing of the four-rod trap. It is mounted to Kapton plates which provide electrical isolation. The mounts itself are screwed onto larger stainless steel frame plates. Axial confinement can be generated with four ring electrodes which are held by four additional rod electrodes. These four rods also increase the stability of the structure and are used to apply micromotion compensation voltages.

voltage is applied to both neighboring segments (see Sec. 1.1.2). In this work we used one of the longer segments. A trap efficiency κ of 34% is found for this trap using boundary element simulations [24]. Axial rf confinement here is simulated to be considerably small [24]. In experiment, however, for radial secular frequencies of 1 MHz, the axial rf confinement frequency is $\approx$ 60 kHz while the simulation predicted $\approx$ 5 kHz. This disagreement is most likely due to electrode misalignment.

2.1.2. The "4-rod trap"

For the demonstration of injection locking, we designed and built a new ion trap. The design goals were:

- Small anharmonicities of the rf field
- Low rf electrode misalignment probability

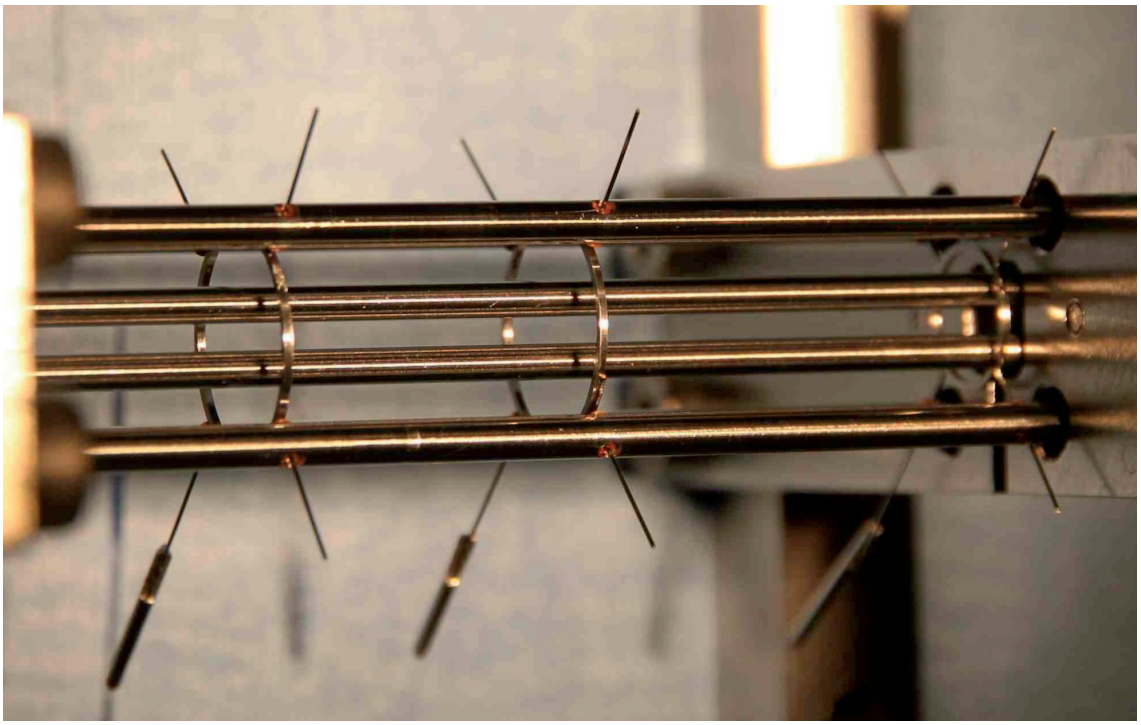

Figure 2.4.: Image of the 4-rod trap from above. One of the stainless steel holders is visible on the right side. Note the good shielding of the Kapton mount behind the holder. Three of the rings are visible with their mounting hulls inside the outer electrodes which hold and isolate them.

- No insulators close to the trapped ions
- Dc and rf wiring are separated
- Rf axial confinement is small
- The new trap should be implemented into the existing apparatus

The anharmonicities are minimized using a traditional 4-rod electrode structure (see Figs. 2.3 and 2.4) with a rod diameter of 2 mm and a distance from the electrode surface to the trap center of $r_0 = 1.475$ mm. These values are very close to the "ideal" 4-rod trap values of $r/r_0 = 1.16$ [19] but still allow for $f/2$ imaging.

The 80 mm long electrodes are made of tungsten. Their relatively long extension helps to minimize both the misalignment and the residual axial rf-field. They are mounted on two pieces of Kapton[1] which are shielded from the ions by attachment to the backsides of two stainless steel holders. The Kapton pieces are designed such that no line of sight towards the ions exists. Apart from the advantages that long

[1]Kapton is a polyimide film developed by DuPont

electrodes have concerning misalignment and low axial rf-confinement, the absence of segmentation does not allow to create the axial trapping potential by applying dc voltages to neighboring segments. This problem is overcome with four ring electrodes centered around the rf-rods which define three segments. The vacuum vessel allows optical access for laser beams on axis (axial beam) and at an angle of 10° to 19° (radial beam). According to these specifications, the two inner rings are designed to be larger than the outer two so that the radial beam can pass outside the outer ring and inside the inner ring to address ions in the trap center. With a quadratic cross section of thickness 0.5 mm, the rings have a diameter of 12.5 mm (inner rings) and 8 mm (outer rings). They are separated by 18.5 mm and 70 mm, respectively.

To mount the rings, four wires are spot-welded to each of them. The wires are fed through isolation hulls made of Kapton which are clamped into holes inside of four stainless steel mounting rods of identical shape as the rf electrodes (Figs. 2.3 and 2.4). The rods are each located in the shadow of a trap electrode, 8.05 mm from the trap axis and have no electrical contact to neither the rings nor any other structure in the trap since they are mounted on the two Kapton holders as well (Fig. 2.3). These rods are also used to apply micromotion compensation voltages, to offset the ion's position [25], and to apply fields for the excitation of the ion's radial motion. Since rf and dc voltages are separated in this trap design, the wire/s for the rf can be fed into the vacuum using an independent, optimized feed-through. This minimizes pick-up of the rf signal by the other wires leading into the vacuum, and the feed-through's capacity (compare to Sec. 2.1.3). In the present implementation of the trap, the rf ground electrodes are connected to the inside of the vacuum vessel. Therefore, only a single coaxial feedthrough is used.

Numerical field calculations

Numerical simulations for several trap layouts have been carried out to optimize and modify the design ideas and requirements. In this work, a finite element method software package, Comsol 3.4[2] has been used.

The radial pseudo potential is obtained by building a two dimensional model (Fig. 2.5 a) with a (dc) voltage of 1 V applied to the two rf electrodes and grounding the two others. From the resulting potential between each electrode pair the curvatures $c_{2,i}$ are determined from a fit of the function

$$\phi_i = c_{0,i} + c_{2,i}x^2 \tag{2.1}$$

to the simulation data. Comparing this result to an ideal potential where $c_2 = U_{rf}/2r_0^2$ (Eq. 1.14), the geometric or trap efficiency factor is obtained. Figure 2.5 b and c show the results. From this we determine $\kappa = 0.98(1)$, our trap geometry is very close to the ideal case [18].

[2] http://www.comsol.com

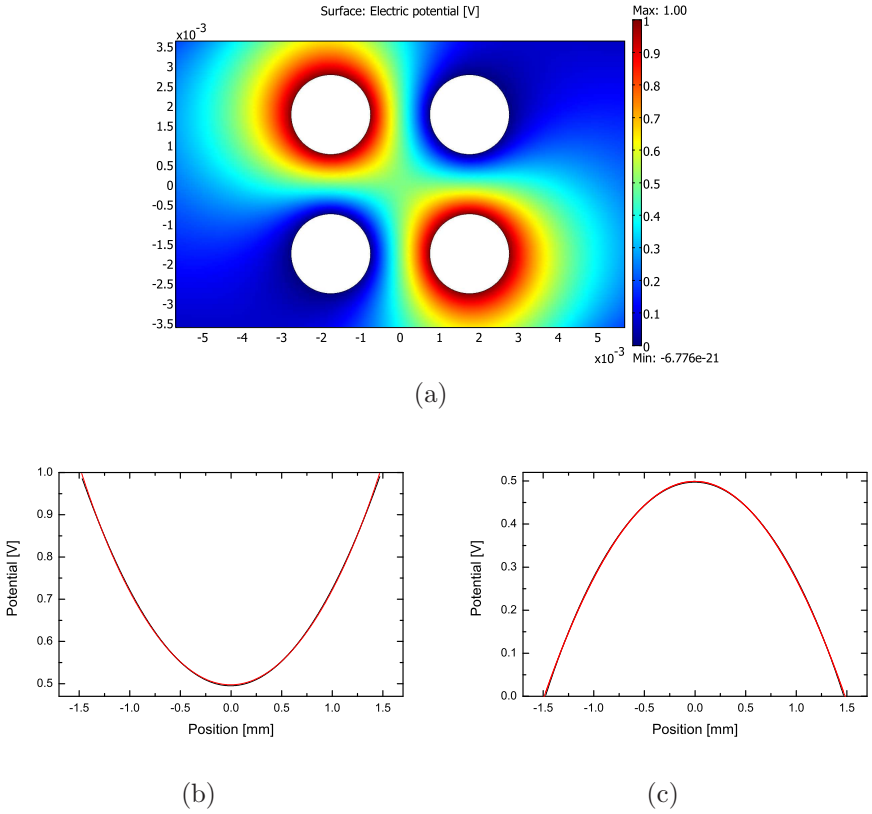

(a)

(b) (c)

Figure 2.5.: Simulated radial potential with 1 V applied to the rf electrodes. (a) Results of the simulation. (b) and (c): Cross-section of the potential between the rf (b) and the ground (c) electrodes. The lines are fits of Eq. 2.1 to the data. The slight mismatch is due to the simulation's finite accuracy.

In order to obtain an approximation for the field in axial direction, a three dimensional model is created. Due to the complexity of the model we expect approximate results only. From comparisons of the radial field obtained by the 2D and 3D models, we estimate an error of $\approx 20\%$ between the full and the 2D model. Figure 2.6 shows the resulting field on the trap axis with 1000 V applied to each of the four ring electrodes. The ring positions are clearly identifiable as potential maxima in Fig. 2.6 a and b. A fit of Eq. 2.1 to the field at the trap center (Fig. 2.6 c) gives the curvature of the axial field. From Eq. 1.15 and the curvature ($\kappa_z U/z^2$) where z is the radial position, we obtain an axial oscillation frequency of 120 kHz. This is about 40% larger than the value determined experimentally. The simulation accuracy is the main source for this deviation. Nonetheless, the agreement is sufficient to obtain qualitative values. Using the same procedures sketched above we determine the residual axial rf confinement to be ≈ 500 times weaker than the radial rf confinement.

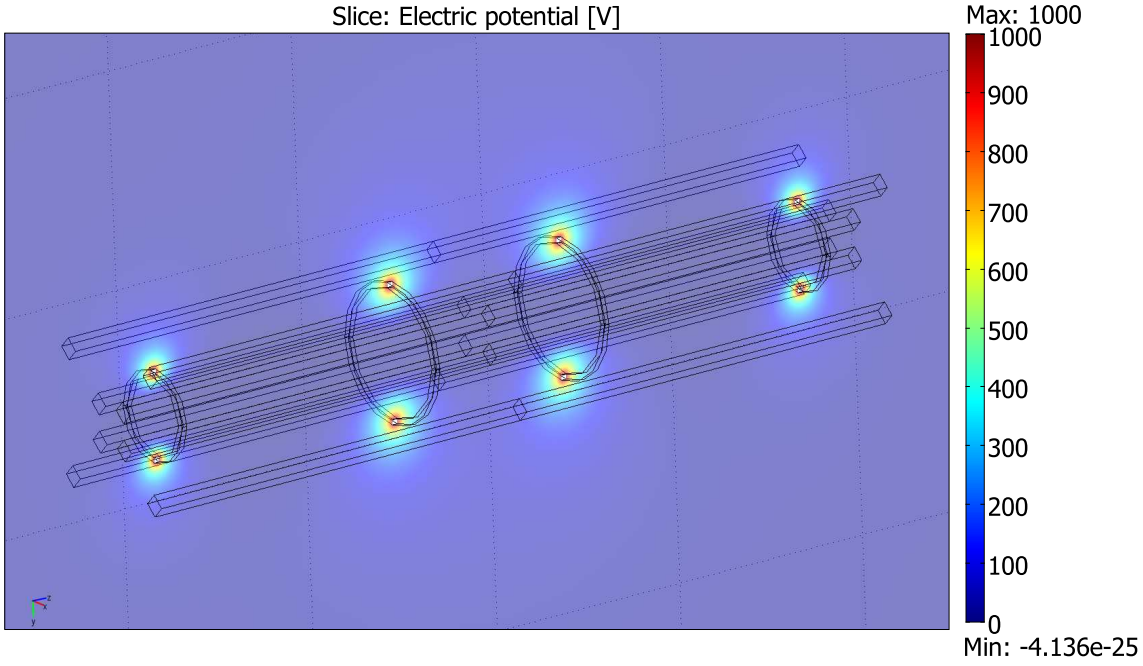

(a)

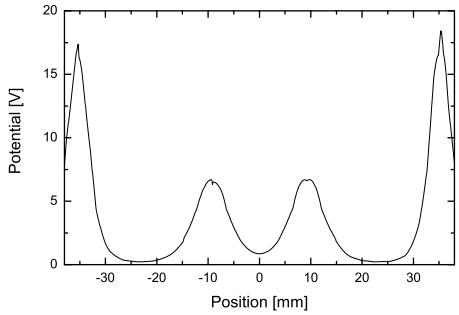

(b)

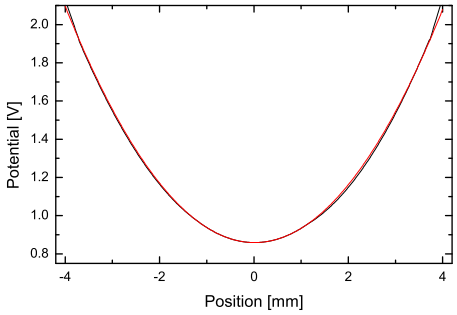

(c)

Figure 2.6.: Axial field with 1000 V on each ring electrode, all other parts are grounded. (a) Slice of the field along the x/z-axis with the simulation model (black lines). (b) Potential on the trap axis over the full trap length. The positions of the rings are visible as potential maxima. (c) Zoom into (b) in the trap center with a fit of Eq. 2.1 to the data. Mismatch and spikes in the plots are due to numerical imperfections.

2.1.3. Electronics

The rf field is generated and filtered to avoid disturbances in the trapping potential. DC voltages for axial confinement are applied to the rings. Compensation voltages on the outer rods are used to minimize micromotion [25]. If needed, we add an additional rf voltage to the outer rods to excite the secular motion of unwanted ions.

Rf electronics

Rf ion traps usually operate at frequencies of $5-50$ MHz and amplitudes of several hundred volts. Such voltages are hard to be obtained directly from a signal source since $P_{in} = U_1^2/2Z$. With $U_1 = 500$ V and $Z = 50\ \Omega$, the consumed power will be 2.5 kW. Also, the impedance of the ion trap will most likely not match the 50 Ω of most signal sources and amplifiers. Both problems can be solved with an electrical "tank-circuit" which resonantly enhances the power and ensures impedance matching [20].

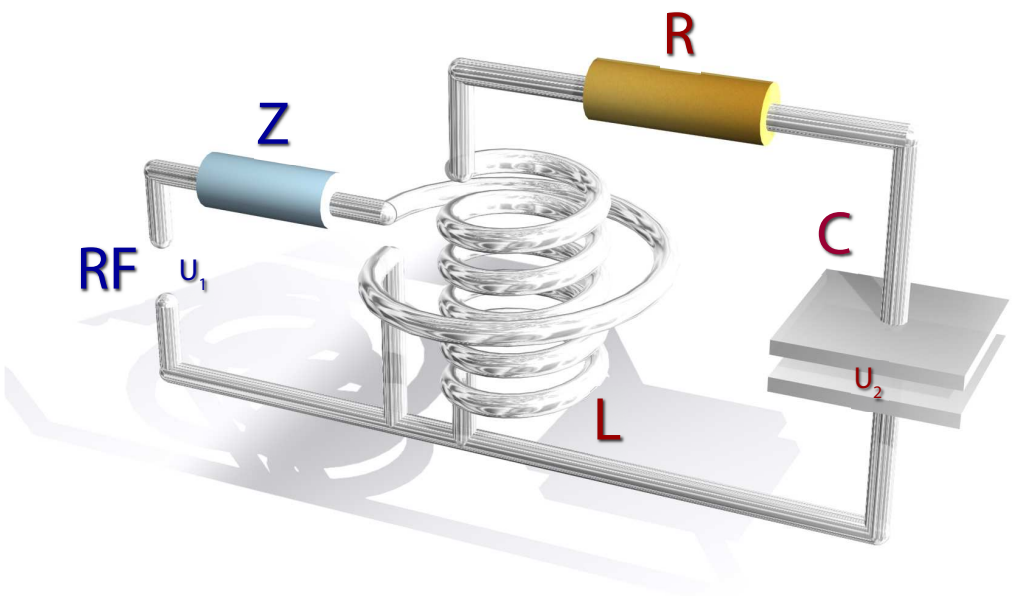

Figure 2.7.: Sketch of a LCR circuit including a signal source of impedance Z and the incoupling loop.

This resonant circuit incorporates the ion trap and is equivalent to a LCR-circuit (Fig. 2.7). The inductance L is a coil, the capacity C is the trap and the resistance R are Ohmic and radiation losses. Such circuits have a resonance frequency and power enhancement factor which reads

$$\omega_{res} = \sqrt{\frac{1}{LC} - \left(\frac{R}{2L}\right)^2} \tag{2.2}$$

$$Q = 2\pi \frac{\text{stored energy}}{\text{dissipated energy per cycle}} = \frac{1}{R}\sqrt{\frac{L}{C}}. \tag{2.3}$$

If the stored energy in the steady state (in the case of perfect impedance matching)

$$W_s = \frac{1}{2} C U_2^2 \tag{2.4}$$

is equal to the input power, the circuit dissipates an energy of

$$W_d = P\tau = \frac{U_1^2}{2Zf} \tag{2.5}$$

per cycle. By inserting the last two equations into Eq. 2.3, the voltage enhancement factor η is found

$$\eta = \frac{U_2}{U_1} = \sqrt{\frac{Q_{crit}\omega_0 L}{Z}} = \sqrt{\frac{\sqrt{4L^2 - CLR^2}}{4CRZ}} \tag{2.6}$$

where Q_{crit} is the "critical" Q-factor, because we assume perfect impedance matching in Eq. 2.5. For perfect impedance matching Q_{crit} equals half of the unloaded Q. Note that the unloaded Q can be measured in the strongly undercoupled regime. From Eq. 2.6 follows that apart from minimizing (Ohmic) losses, small capacity and high inductance of the tank circuit are beneficial to obtain a large voltage enhancement. The same applies to the filtering capabilities of the circuit where the performance is given by the Q-factor, Eq. 2.3.

In our setup, the rf signal is generated by a Marconi 2020A synthesizer, amplified to $\approx$ 5 W with a Mini-Circuits ZHL-5W-1 amplifier, and bandpass filtered. The trap's capacity, together with a coil of $L = 3.39$ μH, made of a wire wound around a Teflon tube, forms the tank circuit. Incoupling of the rf signal to the tank circuit coil is performed with an adjustable wire loop. The coupling is monitored using the reflected rf signal with a directional coupler [20]. The resonance frequency of the endcap trap is $\Omega = 2\pi \cdot 15.8$ MHz while for the 4-rod trap it is $\Omega = 2\pi \cdot 22.6$ MHz. Voltage enhancement is determined to be $\eta = 18$ and $\eta = 24$, respectively. This implies that we operate the traps with a voltage of $250 - 500$ V where we obtain a radial secular frequency of $\omega \approx 2\pi \cdot 0.8$ MHz in the endcap trap and $\omega \approx 2\pi \cdot 1.4$ MHz for the 4-rod trap.

Dc electronics

The filtering of the various dc electrodes is done as follows; the inner dc rings are filtered by a RC low-pass with a time constant of < 1 Hz and connected to a high voltage (HV) power supply to generate the axial confinement. One of the outer dc rings, the "injection ring", is connected to a Stanford Research DS345 synthesizer or another HV supply. A device supplied with a HV allows to generate four independently tunable compensation voltages (one for each outer rod) with four 1 MΩ potentiometers. Each output is low pass filtered. If both rf and dc voltages are to be applied to an electrode simultaneously, we use a bias tee (details in Appendix C.2).

2.1.4. Vacuum system and other components

The ion traps introduced above were both housed in a vacuum system whose main component is a CF150 double cross which is pumped by a Varian VacIon Plus 300 combined ion and titanium-sublimation pump [24] (Fig. 2.8). Initial evacuation is provided with a turbo pump and a scroll pump. On two opposing sides of the cross, the trap and the windows for the laser beams in axial direction and at an angle of 10° to 19° to the trap axis are mounted. A re-entry window facing the trap is attached to image the ions. With the help of elaborate cleaning and baking of the vacuum chamber, we reach pressures of $< 10^{-11}$ mbar with this system.

Two atom ovens [20] are mounted close to the ion trap. They can generate an atomic beam of neutral Mg atoms which are either photo ionized (Sec. 2.2.1) or ionized by electron impact. Each oven consists of a tantalum tube of 1 mm diameter with a piece of magnesium wire inside. The assembly is heated by running a current through a thinner wire also made of tantalum, which contacts the tube. An aperture generates a collimated beam of atoms directed towards the center of the left segment (seen from the camera). One oven encloses an angle of 90° with the trap axis and allows for isotope selective ion loading [20]. The second oven is directed towards the trap axis at an angle of $\approx 45°$. The source of electrons of our electron gun [20] is a tungsten filament which, if heated by running a current through it, constitutes a thermal source of electrons. The filament is held at a potential of $-100 > U > -1000$ V. Focused by a Wehnelt cylinder (the housing which surrounds the filament and is held at a slightly higher potential), the electrons are accelerated through an aperture held at ground potential. However, in this work we did not use the electron gun but produced the magnesium ions by photo ionization (Sec. 2.2.1).

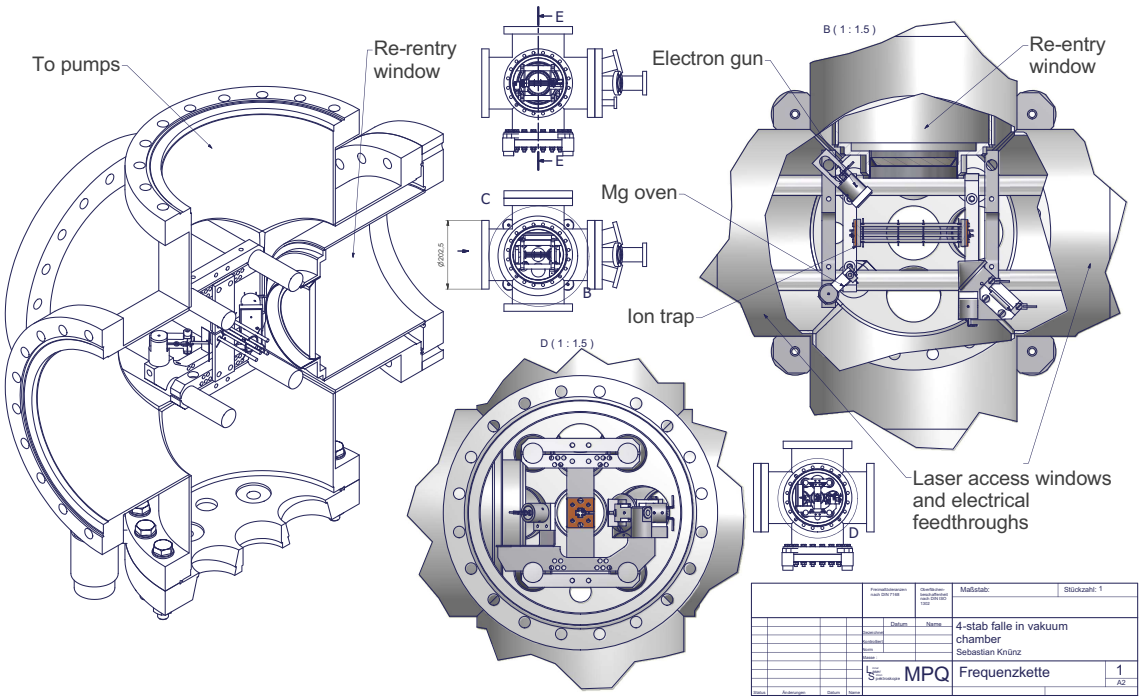

Figure 2.8.: Sketch of the vacuum chamber together with the ion trap, oven and electron gun.

2.2. Laser systems

The laser systems used in this experiment have been built and modified over the last five years [26, 20, 2, 1, 27, 3]. Here we review some basic features of the systems. Due to the failure of a first ytterbium fiber laser system, two dye laser systems have become the workhorses of the experiment. The first dye laser is used for photo ionization, the second for laser cooling. The latter as well as the fiber laser can be locked or referenced to a frequency comb. Recently, a pulsed dye laser which needs far less maintenance work has proven suitable for photo ionization. Moreover, a stable reference cavity has been constructed in order to reduce the linewidth of the phase-locked fiber laser.

2.2.1. Photo ionization lasers

There are two widespread ways of ionizing atoms [20]. The first, traditional way is electron bombardment. Here accelerated electrons knock off an electron from the Mg atoms. The second method is photo ionization where an electron is removed by a single or several photons. Compared to electron bombardment, photo ionization is much more efficient, selective, and does not disturb the trap environment since no electrons can accumulate on isolators and generate an electrical field. Addition-

ally, the requirements for the laser system in accuracy and stability are rather low. Accordingly, photo ionization has become a very important technique to create ions.

In order to photoionize ^{24}Mg atoms, we choose a two-step process: First, we excite the transition from the ground state $3s$ to the $3p$ state ($\Gamma = 2\pi \cdot 78$ MHz) with light at 285 nm. From the $3p$ level, another photon from the 285 nm laser or a photon from our cooling laser at 280 nm (Sec. 2.2.2) ionizes the atom.

One way we generate laser light at 285 nm is frequency doubling a continuous wave Coherent 699 Rhodamine 19 dye laser operating at 570 nm which is pumped by an Argon ion laser. Frequency doubling is performed in a Hänsch-Couillaud locked bow-tie enhancement cavity with a BBO nonlinear crystal [26]. The output power at 285 nm is several hundred μW. This is sufficient to saturate the first step (saturation intensity $I_{sat} = 4402$ W/m^2).

The other laser system, developed by Valentin Batteiger and Camille Estienne, is a pulsed dye laser [27, 3]. Here, the pump laser is a frequency-doubled Nd:YAG which emits nanosecond pulses with a wavelength of 532 nm. This laser pumps a simple home built Rhodamine 6G dye laser. The output is single-pass frequency-doubled by focusing it through a BBO crystal. We obtain a performance similar to the much more complex continuous wave dye laser system.

2.2.2. Cooling/gain laser systems

Compared to the photo ionization laser systems, the requirements for the cooling and gain lasers are considerably higher. The lasers have to be both stable and accurate in frequency to < 100 kHz. Additionally, the intensity has to be stabilized. Accordingly, we have constructed and used two laser systems. The laser cooling transition we use is the D2 ($3s_{1/2} - 3p_{3/2}$) transition at 280 nm in ^{24}Mg$^+$ (linewidth $\Gamma = 2\pi \cdot 41.8$ MHz, $I_{sat} = 2474$ W/m^2).

One laser system is based on a Verdi V10 pumped Rhodamine 19 dye laser operating at 560 nm [1, 3]. The linewidth of the dye laser is about 500 kHz. It is frequency-doubled in a bow-tie cavity with a BBO nonlinear crystal. The output of the frequency-doubled dye laser at 280 nm is usually ≈ 5 mW in the TEM00 mode.

Since we don't have light from the frequency comb at 560 nm, we use an external cavity diode laser at 1118 nm (see also Sec. 2.2.3) as transfer oscillator to phase lock or reference the dye laser to a frequency comb. The diode laser is single-pass frequency-doubled in a LBO crystal. We phase lock the dye laser to the transfer oscillator using an optical beat note between the dye laser and the frequency-doubled diode laser. A frequency offset between the two allows to tune the dye laser in-loop by changing the offset frequency [1, 24, 3]. This technique is called "offset lock". The transfer oscillator diode laser is locked or referenced to an erbium frequency comb via another optical beat note. This way the dye laser, which is phase locked to the transfer oscillator, is phase locked or referenced to the frequency comb. The frequency comb is locked to a GPS disciplined hydrogen maser [1].

The second laser system is based on a ytterbium fiber laser (Koheras Boostik) and delivers about 1.5 W of light at 1118 nm. It has a specified linewidth of < 80 kHz and is tunable over ≈ 20 GHz with an internal piezo actuator which changes the length of the fiber oscillator. This laser is frequency-doubled twice in bow-tie cavities with a LBO and then a BBO nonlinear crystal [26]. The output power is similar to the dye laser system. In order to phase lock the fiber laser frequency, a fiber based optical beat note between the transfer oscillator introduced above and the fiber laser is taken [28]. We add a tunable frequency offset in the beat note (offset lock) in order to tune the frequency of the locked fiber laser.

Note that the radiation characteristics of both laser systems are more or less similar. The main differences between the two systems are the laser linewidth and the tuneability–the dye laser can be tuned to the Mg^+ D1 transition which was important for spectroscopy [3, 1]. The fiber laser system requires little maintenance only but faced serious problems with the built-in high-power amplifier. In contrast, the dye laser system needs everyday care but is robust and very reliable. For the phonon laser work both lasers are used while the results on injection locking were obtained with the low linewidth fiber laser system only.

In order to generate two independent UV laser beams which address the ions, we split the UV output into two equal parts (Fig. 2.1). Each one is sent through a double-pass acousto-optic modulator (AOM). With a beam splitter we take part of each beam to monitor the intensities with silicon carbide UV photo diodes [1, 24]. The photo diode signals are utilized to intensity-lock each laser beam with a PI control loop. This way we generate two laser beams at 280 nm each independently tunable in frequency and amplitude.

2.2.3. A simple but stable reference cavity

Current commercially available frequency combs are accurate but not very stable. This means that their absolute frequency if averaged over some time can be very accurate but the comb lines jitter on a short timescale. This is most prominently due to acoustic noise of the built-in laser oscillator. The time-averaged (> 1 ms) comb mode linewidths of our Menlo Systems erbium fiber combs with a repetition rate of 100 MHz and 250 MHz are ≈ 500 kHz. If we phase lock a laser to one mode of the comb, we increase its linewidth accordingly. A solution to overcome this problem is to lock one of the lasers to a reference cavity which is stable on short timescales but does not give an accurate absolute frequency. The accuracy is introduced by referencing the stable laser to the frequency comb by counting the frequency difference to a comb mode with an optical beat note. A laser locked to the reference cavity is stable (small linewidth) while still the accuracy from the frequency comb is preserved.

A reference cavity usually consists of two (curved, radius R) mirrors separated by a spacer of length L [29]. Crucial for the performance is the material of the spacer

which should have a small coefficient of linear thermal expansion α. Its length changes proportional to the temperature $\Delta L/L = \alpha \Delta T$. The free spectral range (FSR) of a Fabry-Pérot cavity reads $\Delta f = c/2nL$ where n is the refractive index and c is the speed of light in vacuum. With the FSR, the length variation can be rewritten into a change in frequency

$$\frac{\Delta f}{f} = \frac{\Delta L}{L} = \alpha \Delta T. \tag{2.7}$$

Typical thermal expansion coefficients are in the range of $\alpha \approx 10^{-6}/\mathrm{K}$. This implies a frequency change of ≈ 100 kHz per mK temperature change at optical frequencies. Special glasses like ULE[3] [30] have expansion coefficients $< 10^{-12}/\mathrm{K}$ for a certain "zero expansion" temperature [30]. Therefore, if well isolated from thermal and acoustic noise, such systems constitute very stable frequency references. Isolation is achieved by placing the cavity in high vacuum where heat transport is dominantly mediated by radiation. Vibration isolation is provided by suspending the cavity vertically at its mid plane [30]. At this configuration, the gravitational sag lowering the upper part and stretching the lower part largely cancel each other so that vertical noise and vibrations are suppressed.

Design

The requirements for a reference cavity for our experiments are as follows: it should not drift more than 10 kHz/s and a laser locked to it should have a linewidth of < 50 kHz. Another design goal is that all components are low priced and available from stock. The cavity setup was designed and built in collaboration with Janis Alnis.

We decided to use a spacer (Fig. 2.9 a) with a length $L = 115$ mm made of Zerodur[4] with a linear thermal expansion coefficient $\alpha \approx 0.02 \cdot 10^{-6}/\mathrm{K}$. With this, we expect a frequency change of ≈ 2 kHz per mK temperature change. We use one inch mirrors from Layertec[5] of radius $R = 300$ mm which are broadband coated for femtosecond applications. They have a reflectivity of $> 99.9\%$ for wave lengths of $650 - 1100$ nm. At 1118 nm the specified reflectivity is 99.95%. Note that the backsides of the mirrors are not antireflection coated. With this specifications we calculate a FSR of 1.303 GHz, a Finesse of ≈ 6000 and a cavity mode linewidth of ≈ 250 kHz. From similar cavities (Sec. 2.2.2) we know that the laser linewidth can be stabilized to within 1% of the cavity linewidth. Therefore the mirrors meet our requirements in this point as well.

The spacer is suspended on three screws at half of its height (Fig. 2.9 a). The screws are held by an aluminum container (Fig. 2.9 b), which shields the cavity from

[3] http://www.corning.com/specialtymaterials/products_capabilities/ULE.aspx
[4] http://www.schott.com/advanced_optics/english/our_products/zerodur/zerodur.html
[5] http://www.layertec.de/Home.1.0.html

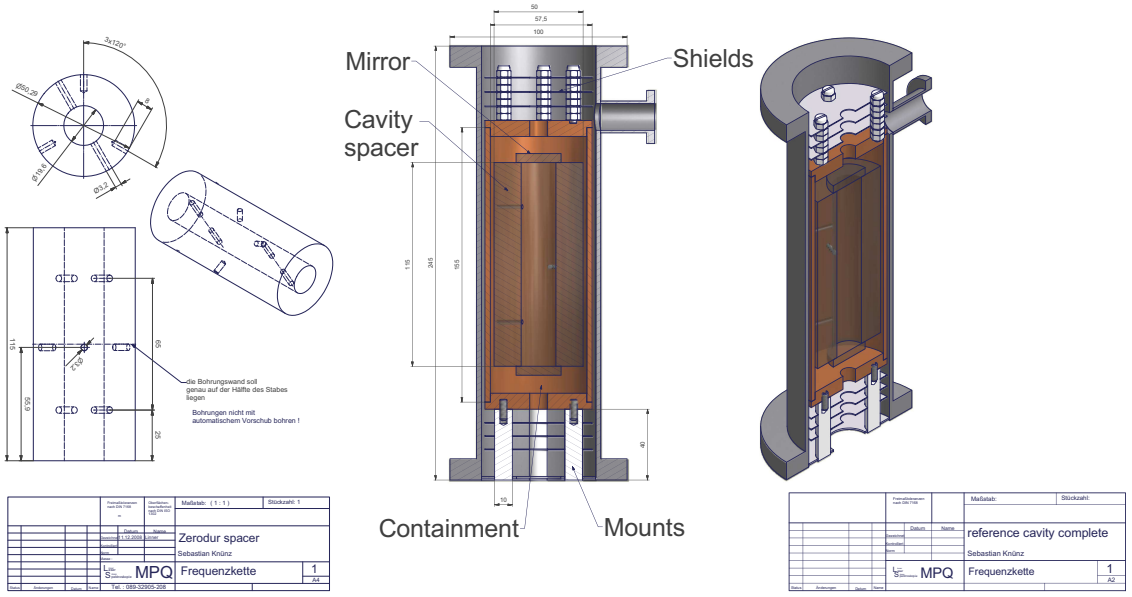

(a) (b)

Figure 2.9.: (a) Technical drawing of the cavity spacer. Three mounting holes are located right below half of the spacer length. Four other holes ventilate the cylindrical space inside. (b) Technical drawing of the cavity setup: the spacer is held inside of an Aluminium container. The container is temperature regulated with a heating wire wound around it. Shields on top and bottom of the cylinder improve the thermal isolation. The container with the cavity inside stands on four Teflon spacers in a vacuum chamber.

ambient thermal radiation. The temperature of the container is regulated with a temperature controller which heats a Kapton isolated copper wire that is wound its outside. The in-loop temperature sensor is attached to the side of the aluminum container, a control temperature sensor is located on top of it. Several layers of metallic foil shield thermal radiation in the vertical direction. The whole assembly stands on four Teflon rods in a vacuum chamber with wedged windows for laser access. The pressure in the vacuum chamber is $3 \cdot 10^{-7}$ mbar sustained by a small ion pump while initial evacuation was performed with a turbo and a scroll pump.

The laser we stabilize is a home-built external cavity diode laser at 1118 nm (Fig. 2.10), which has a free-running linewidth of ≈ 200 kHz. It is utilized as transfer oscillator (Sec. 2.2.2). Protection from back-reflections is ensured with an optical isolator. With an optical fiber we transport the light to a small optical breadboard with the optical cavity. A part of the beam is split off and fed into an optical wavelength meter and the beat note with the fiber laser (Sec. 2.2.2). The remaining light is sent through another optical isolator and focused into the cavity with a $f = 300$ mm mode matching lens. Behind the cavity we observe the transmitted

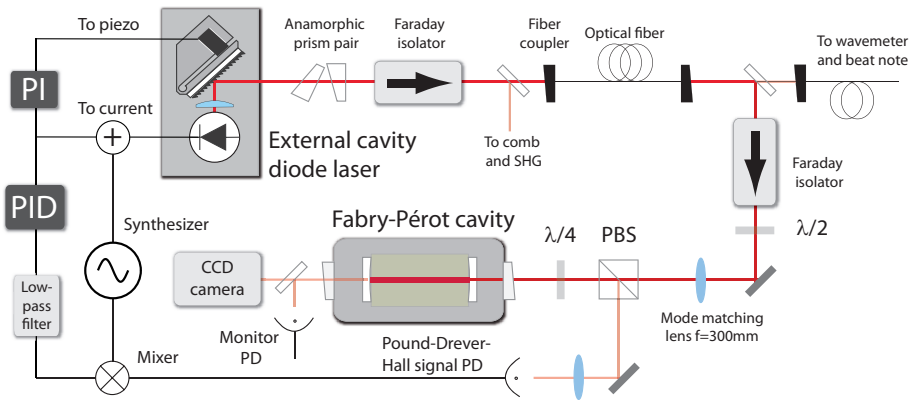

Figure 2.10.: Sketch of the reference cavity setup. The light from an external cavity diode laser is sent via an optical fiber into a Fabry-Pérot cavity. The transmitted light is analyzed with a camera and a photo diode. The Pound-Drever-Hall signal is detected with another photo diode. The signal is mixed with a rf signal which also modulates the diode laser current. Using a PID and a PI controller the error signal is fed back onto the laser current (fast feedback) and the piezo crystal which tilts the grating (slow feedback) to lock the diode laser to the cavity.

light with a photo diode and a CCD-camera (Fig. 2.10). We employ the Pound-Drever-Hall (PDH) method [31] to lock the laser to the cavity. For this, the laser frequency needs to be modulated, which we implemented by adding a 9 MHz signal to the current of the diode laser. The PDH scheme requires three additional optical components: a polarizing beam splitter (PBS), a $\lambda/4$ plate between the PBS and the cavity, and a fast photo detector on the PBS port with the reflected light of the cavity (Fig. 2.10). If the photo diode signal is mixed with the modulation signal, a voltage proportional to the laser frequency detuning from a cavity resonance is generated. This signal is fed back onto the current (fast feedback) using a PID controller and the grating tilting piezo (slow feedback) with a PI controller (Fig. 2.10).

Results

The system was characterized in absolute frequency by counting the beat note between the stabilized diode laser and the frequency comb. A typical result is shown in Fig. 2.11. Here spikes mark times where the diode laser is not locked to the cavity. The maximum drift here is ≈ 15 Hz/s. The drifts of the cavity are mainly due to temperature changes in the laboratory induced by the air conditioning since we have only one stage of temperature regulation and shielding. For improved performance, several containers, each stabilized in temperature could be employed. The maximum observed drift under typical laboratory conditions is < 50 Hz/s. The air conditioning cycles and oscillations of the temperature controller cause the cavity frequency to oscillate with an amplitude of < 1 MHz with a time constant of approximately

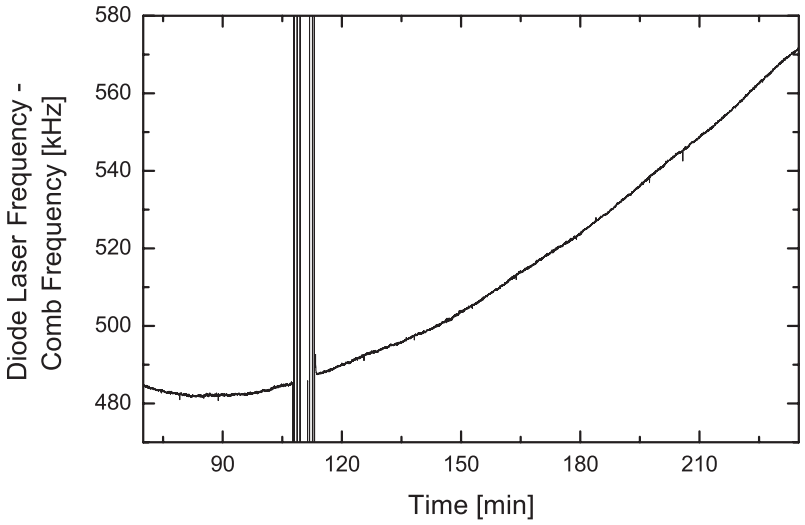

Figure 2.11.: Exemplary measurement of the beat note between cavity and frequency comb. The spikes mark times where the laser is not locked to the cavity. Here the maximal cavity drift is ≈ 15 Hz/s.

one day.

To observe the linewidth of the locked laser, a narrower reference laser or more elaborate methods are necessary. In this wavelength region only the fiber laser was available. Therefore, we obtain an upper limit from the beat note between the stabilized diode laser and the fiber laser. Figure 2.12 a shows the result. The characteristic pedestal of the diode laser is visible. Figure 2.12 b is a zoom into the spectrum with a fit to the central peak which reveals a linewidth of ≈ 59 kHz. Since the fiber laser is specified to have a linewidth on the order of < 80 kHz and the beat note is a convolution of the individual linewidths, we attribute most of the width to the fiber laser. From a beat note of a laser at a slightly different wavelength of 972 nm locked to this cavity with a laser locked to an ultra stable ULE cavity [30] with a drift and linewidth of < 1 Hz/s, we obtain a linewidth of ≈ 10 kHz. Better isolation of the diode laser from acoustic noise reduced the linewidth to ≈ 2 kHz.

In conclusion, this simple reference cavity made of standard components performs well and is much better than the requirements of our experiment as well as of many applications in the field of quantum optics. Several follow up copies of this cavity have been built[6].

[6] J. Alnis at the MPQ, and in the Kippenberg group at the EPFL in Lausanne, Switzerland

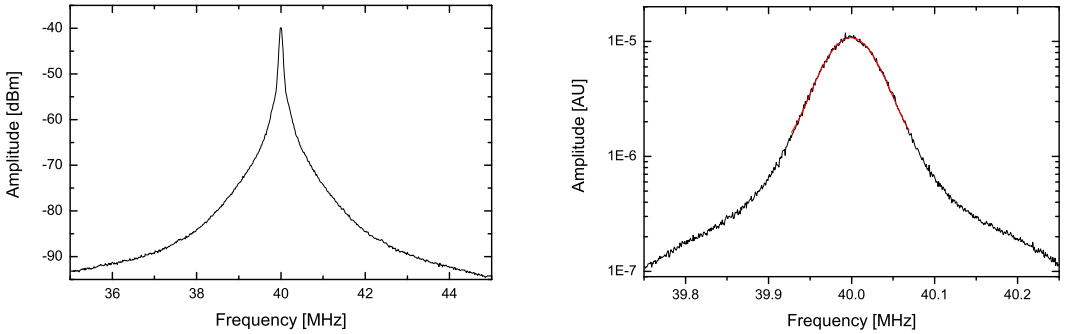

(a) (b)

Figure 2.12.: Beat note between the fiber laser and the stabilized diode laser (resolution bandwidth 1 kHz). (a) Full spectrum with the characteristic noise pedestal of the diode laser. (b) Zoom into the spectrum. The line is a Gaussian fit to the approximately Gaussian peak in the spectrum, the linewidth is ≈ 59 kHz.

2.3. Fluorescence detection and analysis

One of the most important parts in this work is an imaging system with a single-photon camera (SPC) (Quantar Mepsicron II). It indicates each detected photon individually. In contrast, EMCCD cameras forward complete images. For the experiments in Chapter 4, we implemented two SPC photon signal analysis schemes that allow to measure the spectrum of the oscillator in situ and the phase relative to an external signal.

2.3.1. Imaging system

The imaging system consists of three parts (Fig. 2.13). A four lens $f/2$ condenser collects the light from the ions and magnifies it by a factor of five. With an additional microscope objective, an overall magnification of ≈ 100 is achieved. The photons are detected with a single-photon camera (SPC) (Quantar Mepsicron II). Its detector is based on a multi channel plate and has a circular shape with a diameter of 25 mm and a spatial resolution of 56 μm. The dark count rate of the SPC is < 50 Hz for the whole detector. Detected photons are indicated by a trigger signal of 10 μs length with a timing resolution of 100 ps. This 10 μs non-paralyzable dead time[7] together with several other sources of dead times in the camera electronics limit the maximal count rate to ≈ 54 kHz. Simultaneously with the trigger signal, the x and y positions

[7] A non-paralyzable dead time is not restarted by events within the dead time interval. In contrast, a paralyzable dead time restarts with an event within this interval so that a detector can be "paralyzed", it does not indicate events any more [32].

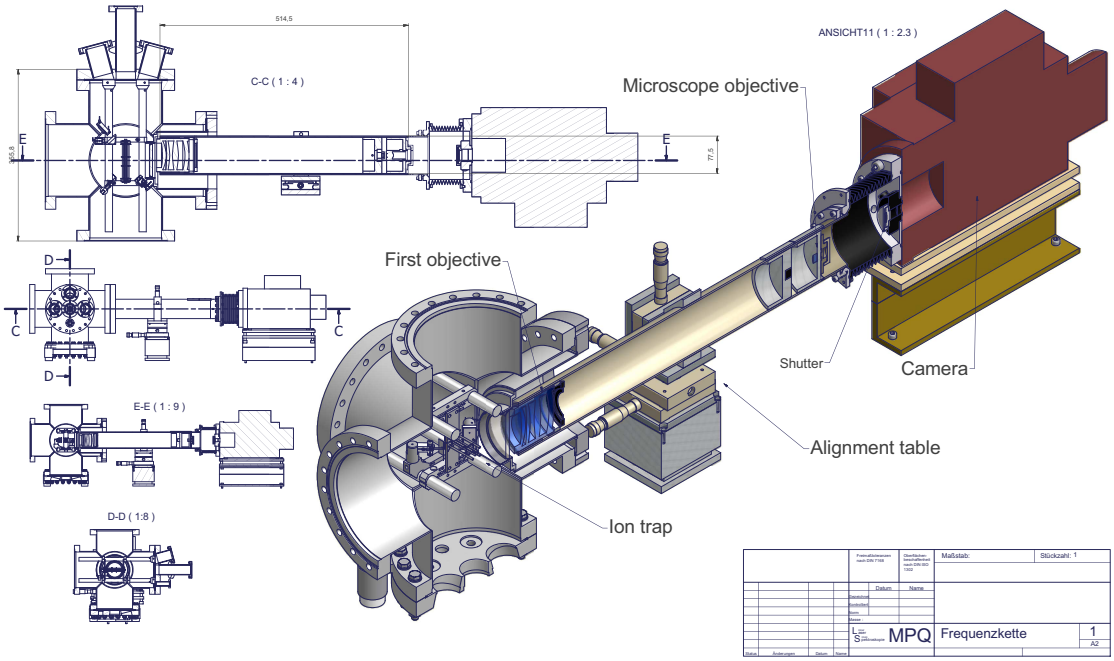

Figure 2.13.: Imaging system used in this work. The trap in the vacuum system is visible on the left. Fluorescent light is captured by a four-lens condenser and further magnified with a microscope objective onto a single photon camera.

of the arrived photons are encoded in two voltages. We slightly oversample these signals by digitizing them with a resolution of 512×512 pixels using a commercial A/D-board.

Camera calibration

Two simultaneously trapped ions on one hand repel each other since they are equally charged and on the other hand are pushed together by the trapping potential. Following [33], the equilibrium distance is

$$\Delta x_{pixels} = B \sqrt[3]{\frac{e^2}{2\pi\epsilon_0 m}} \omega_z^{-2/3} \tag{2.8}$$

where B is a constant factor to transform the pixel scale of the images into μm. By measuring the ion-ion distance for several axial frequencies ω_z, B can be extracted with a fit to the data. Using this scheme, we determined that 1 pixel on our images corresponds to 0.526(4) μm in the trap. The resolution of the imaging system is measured to be ≈ 2 μm (for details see Sec. 3.2).

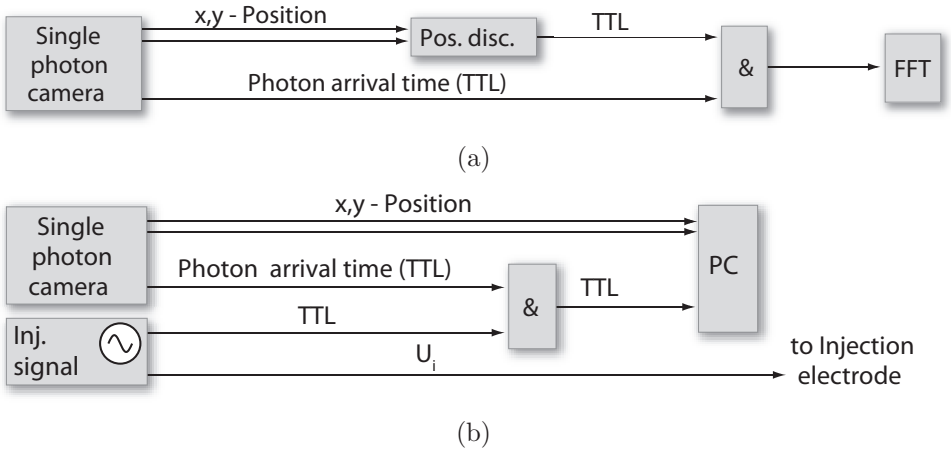

Figure 2.14.: Signal processing schemes of the single-photon camera. (a) Position resolved selection of the camera trigger signals to analyze the timing spectrum of the detected photons (pos. disc.: position discriminator). (b) Phase sensitive, stroboscopic detection. Here the photons are only forwarded if they arrived within a certain phase window relative to the injected signal.

2.3.2. Position sensitive camera readout

For position sensitive readout (Fig. 2.14 a), we have built a position discriminator which forwards the photon trigger signal if it arrived in a certain region of the camera only (Sec. C.1). The region of interest is chosen by selecting four voltages from $0-5$ V with four potentiometers which select the respective acceptance regions for the x and y values from the camera. Four electronic comparator units each fed with a selection voltage and the x or y signal generate logic signals. All signals are combined using AND electric circuits and conjuncted with the photon trigger signal. The selected signal is then forwarded to an Agilent E4445A spectrum analyzer.

2.3.3. Phase sensitive (stroboscopic) camera readout

Phase sensitive readout or stroboscopic detection is done by forwarding only the trigger signals of photons which arrived in a certain phase window relative to an external signal (Fig. 2.14 b). A phase window is selected with a delay generator (Stanford Research DG535) which, if triggered by the injected signal, forwards a short pulse. The phase window has a size of $\approx 13°$. The camera trigger signal is transformed into a short pulse in the same way. Both signals are conjuncted in a logic AND electrical circuit (compare to Appendix C.1) and forwarded to the A/D-card trigger input. This way photons are only picked up by the computer if they arrived within a certain phase window relative to an external signal, and stroboscopic images are generated.

2.4. Data acquisition and evaluation

Two computers, equipped with several data acquisition tools control the experiments. One takes the camera data, the second controls all other devices and performs the measurements. Both computers communicate using a home-built parallel communication bus and are each run by a program written in Delphi[8]. An additional software suite also developed in Delphi is used for off-line data analysis. The backbone of these systems was developed for the magnesium spectroscopy [2, 24, 1] but since then further optimized and significantly extended in functionality.

2.4.1. DAQ system

First, we present the camera readout system, then the main DAQ part, and finally the communication bus.

Camera DAQ

The computer acquiring the SPC signals is used like a camera, taking pictures of the ions on command and saving them, while transmitting reduced image data (count rate in a region of interest) to a second computer. It is based on a Meilhaus[9] ME4610 card which provides 16 single ended 16 bit A/D channels and 32 TTL-I/Os. Controlled by a Delphi-written software (Sec. C.3), the A/D channels are operated in the "triggered mode". The trigger input is connected to the photon arrival trigger signal of the SPC. If triggered, the x and y position voltages of the arrived photons are measured. The voltages are translated into an image of 512×512 pixels and displayed. The images are saved in a matrix form, in the slaved mode outlined below also including a small header with an image number and the integration time obtained with the computer's high precision timer (accuracy better than 1 μs). A real-time video mode with a selectable frame rate can be chosen for alignment and monitoring purposes. The measuring mode slaves the software to the bus, where image acquisition and integration time are triggered over the communication bus. A circular region of interest can be selected whose count rate will be directly transmitted over the bus. Furthermore, a real-time histogram window with a Gaussian fit routine and a region of interest magnification window can be shown for alignment purposes. More details and a screenshot of the software are given in Appendix C.3.

The system is characterized and tested to perform well up to a photon count rate of 50 kHz with an uncertainty of $\approx 1‰$ at an integration time of 1 s, due to the timing accuracy of 1 ms.

[8] http://www.embarcadero.com/products/delphi
[9] http://www.meilhaus.de/en/home/

Main DAQ

The main computer controls counters and synthesizers used in this experiment via a GPIB card. Further, it houses two Measurement Computing[10] USB-1208FS devices. These USB devices offer each 4 A/D input and 2 D/A output 12 bit channels as well as 16 TTL-I/O channels. A software package (Sec. C.4) written in Delphi controls all devices. The frequencies of the laser beams are set via the offset (local oscillator) frequencies of their phase locks, the AOM frequencies using synthesizers or the D/A outputs. If the reference cavity is used, the absolute frequency of the lasers is maintained by determining the beat frequency between the diode laser and the frequency comb. With this, a compensation value for the offset synthesizer frequency is calculated and set. This way the laser frequencies are automatically kept at constant detunings with respect to the Mg^+ cooling transition. Apart from the laser frequencies, the statuses of the laser intensity locks are monitored.

All measurements which involve scans of certain parameters are implemented using this software. After each measurement, an extensive data file is written including all parameters and the measurement data. A screenshot of the software and more details can be found in Appendix C.4.

Home-built data bus

Both computers transfer information using a simple communication bus consisting of 16 parallel TTL signal cables to exchange data (the count rate of a selected region of interest) and four more TTL lines for communication purposes. On the camera computer side the cables are connected to the Meilhaus card, on the main DAQ computer side to the USB-1208FS devices. This bus system can send the following commands:

- Switch the camera computer into the experiment mode. This implies stopping all other processes and waiting for further instructions
- Start and stop taking an image
- Discard the image if something went wrong
- Transmit two parallel 16 bit data blocks

The bus works very reliably. It is independent of problems e.g. in the network when using TCP/IP based communication, and the measurement computers do not have to be connected to the Internet. Meanwhile, a single computer would be sufficient for these purposes now.

2.4.2. Data analysis software suite

Since a large amount of data is generated in this experiment, an evaluation software suite (Fig. 2.15) has been written for automated data processing. Each scan consists of a datafile and a set of images. The datafile incorporates the statuses and settings of all devices together with the scan data which consists of synthesizer settings and the data from several frequency counters. The file tree is displayed in the left panel. A mouse click here selects and loads a datafile or changes the directory. In the following, the corresponding images can be browsed and e.g. the counts in a region of interest of the image can be extracted and plotted versus the scan data. The images are shown on the bottom while the data is plotted on the top panel. The panels on the right show file and evaluation data. Several numerical tools, e.g. Levenberg Marquardt and Simplex least square fitting methods taken from Numerical Recipes [34] are implemented to analyze the data. Several sets of data can be selected, saved, and compared. Further processing of the images can be performed using histograms of full images or image regions. Centroid, root-mean-square spread, and a Gaussian fit are calculated in the histogram. Buttons allow to determine, plot, and save the centroid (center of gravity) or Gaussian width of all images in a scan.

[10] http://www.mccdaq.com/

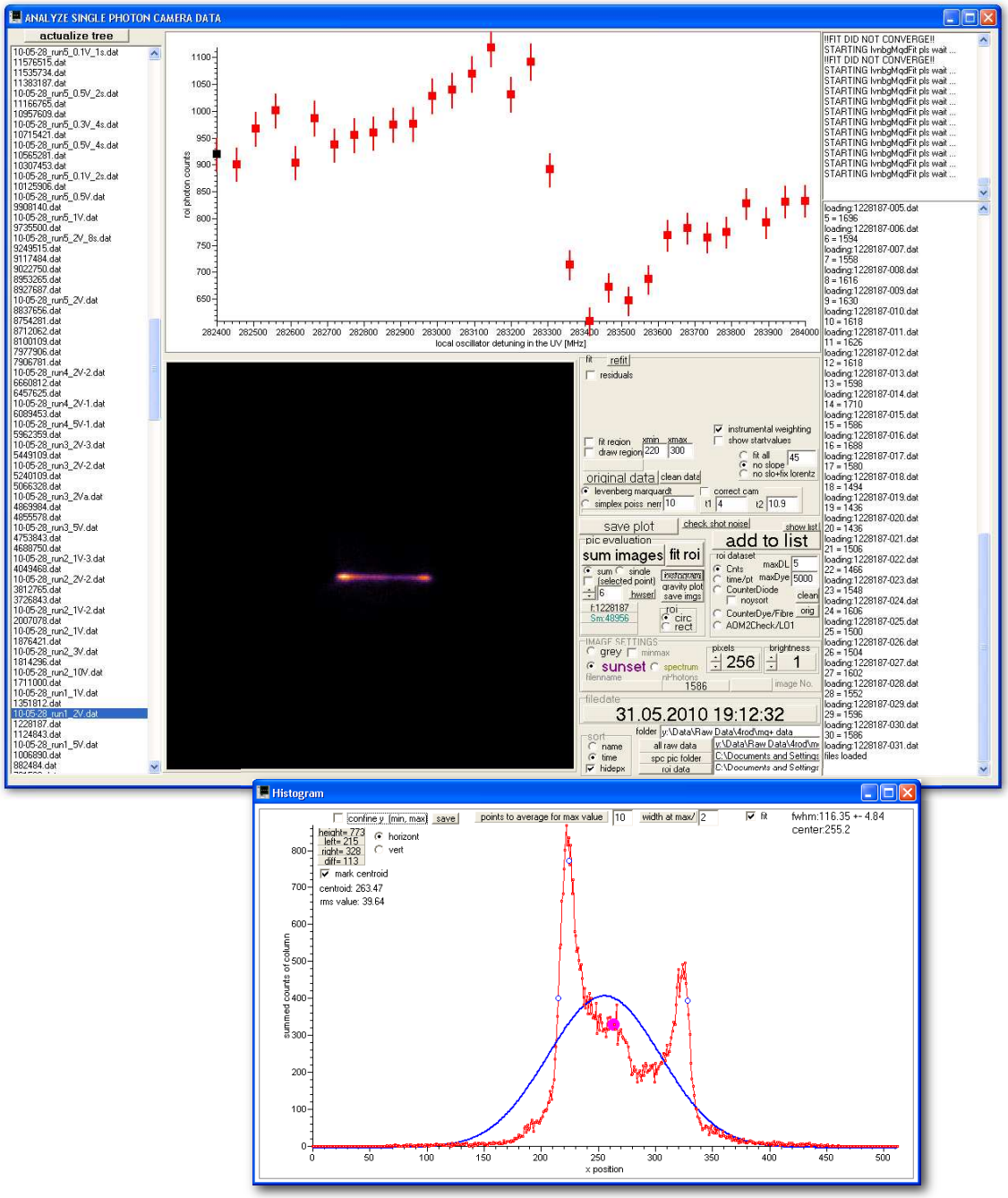

Figure 2.15.: The data analysis software suite. In the panel on the left, data files can be selected out of a folder list. Images are shown on the central panel, plotted data on top. The panels on the right contain file and evaluation data. Histograms and related data are displayed in a separate window.

3. A trapped-ion phonon laser

While amplification by stimulated emission has been observed for photons in the micro wave (maser) and the optical frequency region (laser), its mechanical analogue, stimulated emission of quanta of mechanical motion, phonons, has not been studied quantitatively yet. In the last years, there has been significant progress in theoretical studies of various systems like trapped ions [35], semiconductors [36], nanomechanics [37], nanomagnets [38], and others [39]. Findings of related effects have been reported, e.g. phonon amplification in a superlattice [40], and superradiance in Bose-Einstein condensates [41]. However, the complexity of most experimental realizations did not allow to unambiguously isolate phonon laser action.

Our system, a single trapped $^{24}Mg^{+}$ ion, has one mode of oscillation only, the center-of-mass mode. The motion is driven (phonons are generated) by a blue-detuned laser while a red-detuned laser provides damping of the oscillations. The system is well isolated and controllable, allows a detailed theoretical description and precise experimental investigation. We report that this system is subject to a threshold condition and amplification saturation similar to a Van-der-Pol oscillator [42, 43]. From our observations and the derivation of the rate equations for the generation and destruction of phonons, we deduce that we observe stimulated generation of phonons. Since our realization of a phonon laser does not emit phonons, we studied its dynamics under the influence of an external signal (Chapter 4). Injection locking indeed allowed the coherent manipulation of this trapped-ion phonon laser.

Our observations also shed light on the action of blue-detuned lasers. The role of a blue-detuned laser has widely been associated with heating. We demonstrate that a blue-detuned laser does not simply heat the ion motion but can give rise to surprisingly rich dynamics including regenerative oscillations, phonon laser action, and hysteresis.

In this chapter we introduce the theory behind the laser-driven oscillations of a trapped ion. We present the concept and observation of thermal motion in contrast to the following observation of coherent oscillations. Further, we discuss the stimulated generation of phonons in this system and report on the observation of hysteresis.

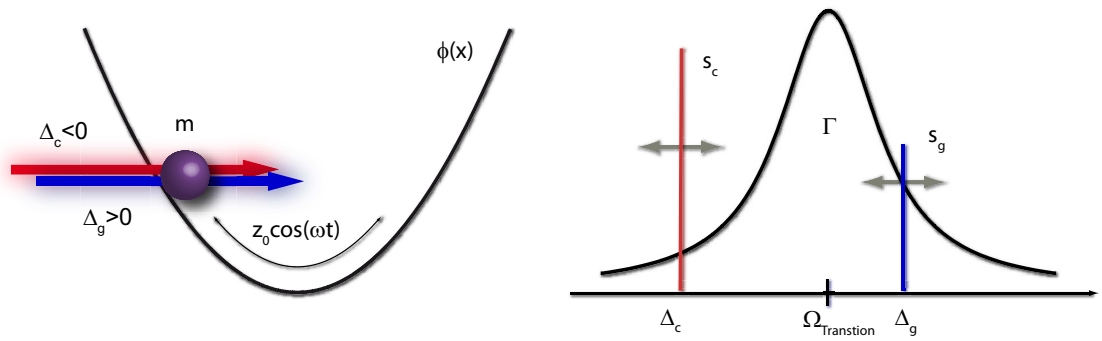

Figure 3.1.: Sketch of the trapped-ion phonon laser setup. Two lasers illuminate a trapped ion of mass m. One laser is red ($\Delta_c < 0$), the other blue ($\Delta_g > 0$) detuned relative to an atomic transition of width Γ. The laser frequencies are modulated due to the ion's motion.

3.1. Theory

Figure 3.1 shows a sketch of the experiment. An ion, trapped in a harmonic potential, is illuminated by two laser beams. One is red-detuned, the other one blue-detuned relative to an atomic resonance. The first one cools or damps the motion, the second one amplifies it. The main difference between the following treatment and the well-known theory of laser cooling [17] is that we also consider blue detuning and do not assume small velocities as in the final stages of laser cooling theory (Sec. 1.2).

In the following we restrict ourselves to a one-dimensional harmonic oscillator. This is justified as in our trap the axial confinement (in z-direction) is much weaker than the radial one.

3.1.1. One laser

Let's assume that the ion oscillates in the potential in axial, z-direction. Then position and velocity read

$$z(t) = z_0 \sin(\omega t) \tag{3.1}$$
$$v(t) = v_0 \cos(\omega t) \tag{3.2}$$

where $\omega = \omega_z$ is the oscillation frequency of the ion in axial direction. In the moving reference frame of the ion the laser detunings are not constant in time but oscillate as well (Eq. 3.3)

$$\delta_{eff,i} = \Delta_i - \vec{k} \cdot \vec{v} = \Delta_i - k v_0 \cos(\omega t) \tag{3.3}$$

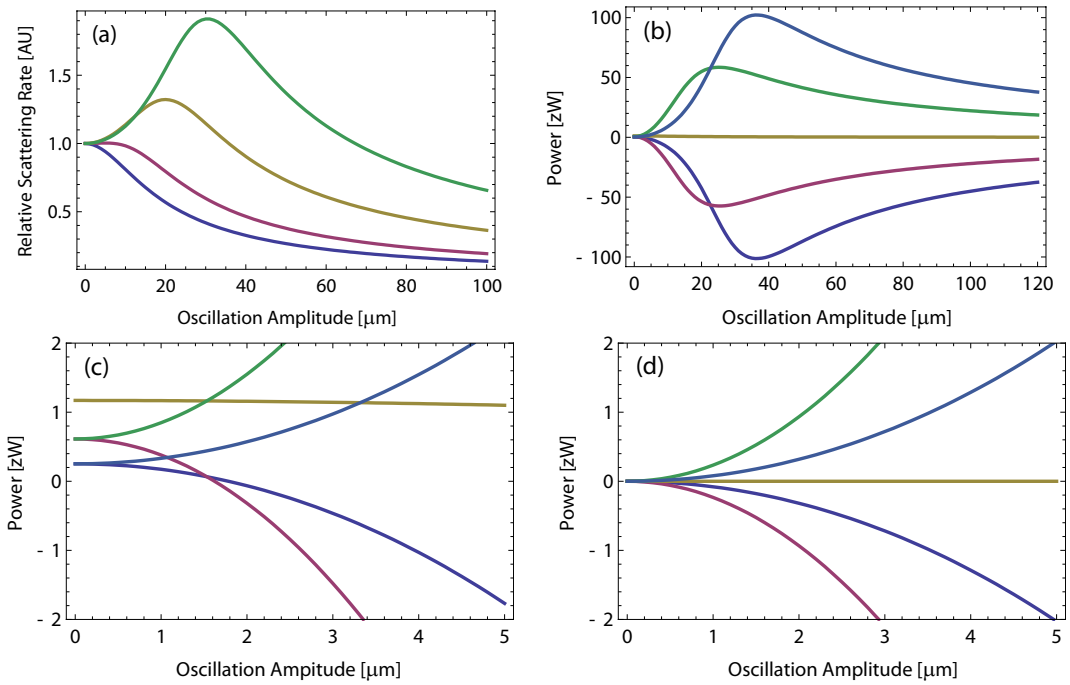

Figure 3.2.: Scattering rates and total average power (zW= 10^{-21} W) acting on the ion by a single laser beam. (a) Relative scattering rate versus ion oscillation amplitude for laser detunings ranging from $\Delta_i = 0$ to $|\Gamma|$. Note that except for $\Gamma = 0$, the scattering rate increases and peaks before decreasing again for larger oscillation amplitudes. (b) Total cycle-averaged power (Eq. 3.7) versus ion oscillation amplitude for $s_i = 0.1$ and detuning $\Delta_i = -\Gamma$ to $+\Gamma$. (c) Zoom into (b). Note that due to spontaneous emission, the power for small oscillation amplitudes is always positive. (d) Zoom into a plot of the damping/gain power only (Eq. 3.5) neglecting spontaneous emission (Eq. 3.6).

where $\Delta_i = 2\pi \cdot (\nu_{laser,i} - \nu_{transition})$ denote the detunings and k the wavevector of the laser beams. From this we obtain a time dependent scattering rate (Eq. 1.18) which we average over one oscillation period of the ion

$$\langle g(s_i, \delta_{eff,i}(t))\rangle_\omega = \frac{\omega}{2\pi}\int_0^{2\pi/\omega} dt \frac{\Gamma s_i/2}{1 + s_i + \frac{2(\Delta_i + k v_0 \cos(\omega t))^2}{\Gamma^2}}, \tag{3.4}$$

where s_i denotes the saturation parameter of the laser. The dependence of the scattering rate (Eq. 3.4) on the oscillation amplitude z_0 is shown in Fig. 3.2 a for detunings ranging from $\Delta_i = 0$ to $|\Gamma|$. For $\Delta_i = 0$ the scattering rate decreases monotonically, whereas for larger detunings, there is an increase first before decreasing as well. In the case of nonzero detuning, the scattering rate peaks at a nonzero oscillation amplitude where the oscillating Doppler shift induces a shift towards and away from the line center and, due to the Voigt line shape of the resonance, the

fluorescence increase overcompensates the fluorescence decrease one half-cycle later. As the Doppler shift increases with further increasing oscillation amplitude, the laser is detuned even across the line center, and the scattering rate drops. This modifies the force on the ion and, thus, the cycle-averaged power (Eq. 1.20) transmitted to the ion. Rewritten it reads

$$\langle P_{a,i}\rangle_\omega = \langle F_i(t)v(t)\rangle = \langle \hbar k g(s_i, \delta_{eff,i}(t)) v_0 \cos(\omega t)\rangle_\omega. \tag{3.5}$$

In the following, we assume the regime of Doppler cooling or weak-binding, where a second process has to be taken into account: The recoils of the photons emitted by spontaneous emissions, which "shake" the ion. It is directly related to the scattering rate and does not change sign with the detuning, thus on average adds energy to the ion's motion. The cycle-averaged power due to this process reads (Eq. 1.21)

$$\langle P_{s,i}\rangle_\omega = \langle (1+\xi)\frac{\hbar^2 k^2}{2m} g(s_i, \delta_{eff,i}(t))\rangle_\omega. \tag{3.6}$$

Note that this equation shows identical characteristics as the cycle averaged scattering rate introduced above (Fig. 3.2 a, Eq. 3.4). The total cycle averaged power of a laser beam is the sum of both contributions and reads

$$\langle P_{tot,i}\rangle_\omega = \langle P_{a,i}\rangle_\omega + \langle P_{s,i}\rangle_\omega. \tag{3.7}$$

Figure 3.2 b shows a plot of Eq. 3.7 for detunings from $-\Gamma$ to $+\Gamma$ for the D2 transition in $^{24}Mg^+$ ions (Appendix A) and $\omega = 2\pi \cdot 70$ kHz. The power increases as the oscillation amplitude increases due to the viscous nature of the laser force. For larger oscillation amplitudes the force decreases as the scattering rate decreases (compare to Fig. 3.2 a). The difference between Eqs. 3.7 and 3.5 is demonstrated in Figs. 3.2 c and d. While Fig. 3.2 d is a plot of Eq. 3.5 excluding spontaneous emission, Fig. 3.2 c is a zoom into Fig. 3.2 b where spontaneous emission is taken into account (Eq. 3.7). In Fig. 3.2 c the slight increase in power due to the spontaneous emission can be observed while the contribution of the cooling/gain power (Eq. 3.5) dominates for larger oscillation amplitudes (Fig. 3.2 b).

3.1.2. Two lasers

In the case of two lasers, the total power has four contributions. We denote the cooling-laser which we intend to use with negative (red) detuning with the index c, and the second, gain-laser with positive (blue) detuning with the index g. Only a single contribution, $\langle P_{a,c}\rangle_\omega$, damps the motion:

$$\langle P\rangle_\omega = \langle P_{a,c}\rangle_\omega + \langle P_{s,c}\rangle_\omega + \langle P_{a,g}\rangle_\omega + \langle P_{s,g}\rangle_\omega. \tag{3.8}$$

Solutions of this equation are located at the roots of $\langle P(z_0')\rangle_\omega = 0$. Further, an increase in oscillation amplitude across the root in power needs to be damped (the

power has to be negative) so that the oscillation amplitude decreases back and vice versa. Therefore only roots in the power with negative slope are stable. Thus, we require that $\partial_z \langle P(z) \rangle_\omega |_{z=z_0} < 0$.

Since no analytic solutions exist for this expression, numerical studies have been conducted and identified four dynamical regimes.

3.1.3. Dynamical regimes

Our approach to explore the dynamics is to keep all parameters except for the gain laser intensity constant. Hence, we study the dependence on the amplification. The parameter we are interested in is the time-averaged kinetic energy of the ion which is composed of a contribution from the oscillation and an incoherent part due to spontaneous emission. We observe the total kinetic energy by means of the root-mean-square (RMS) spread/oscillation amplitude of the ion.

For a given set of parameters, the point where the cooling power balances the heating power coincides with a certain intensity ratio $r = s_g/s_c$ of the two laser beams. If we neglect saturation and spontaneous emission, this critical intensity ratio r_t at the threshold can be found [24]:

$$r_t = \frac{|\Delta_c|}{\Delta_g} \left(\frac{\Delta_g^2 + (\Gamma/2)^2}{\Delta_c^2 + (\Gamma/2)^2} \right)^2 . \tag{3.9}$$

When the intensity ratio is below threshold, $r < r_t$, the ion equilibrates in a thermal distribution. Here the situation is similar to Sec. 1.2. The difference is that the motion is not only excited by the scattered photons from the red-detuned laser but from the blue-detuned laser as well. Therefore, the temperature will be higher.

Intuitively, one would expect that above threshold the ion will be driven out of the trap. In fact, the dynamics are more complex and two regimes can be identified [24]: if $\Delta_g \geq |\Delta_c|$, we call it domain $\mathcal{B}$, the motion becomes unstable above threshold. For $\Delta_g < |\Delta_c|$, the domain $\mathcal{A}$, the ion maintains stable oscillations for a certain range of r. Here, the motion is composed of a thermal, stochastic contribution which is due to spontaneous emission, and a stable, coherent part which is maintained by stimulated emission of phonons by the blue-detuned laser. For further increased intensity ratios, the motion becomes unstable as in domain $\mathcal{B}$. A characteristic of both domains is bistability between a thermal and a coherent state.

3.1.4. Domain $\mathcal{A}$

Figure 3.3 a shows the underlying mechanism in this domain for $\Delta_c = -2\pi \cdot 74$ MHz, $\Delta_g = +2\pi \cdot 25$ MHz, $\omega = 2\pi \cdot 70$ kHz, and $r = s_g/s_c$ ranging from 0.04 to 0.28. For small r the stable oscillation amplitudes ($\langle P \rangle_\omega = 0$) are small and increase with larger r. Figure 3.3 b is a plot of the oscillation amplitudes with a root in power,

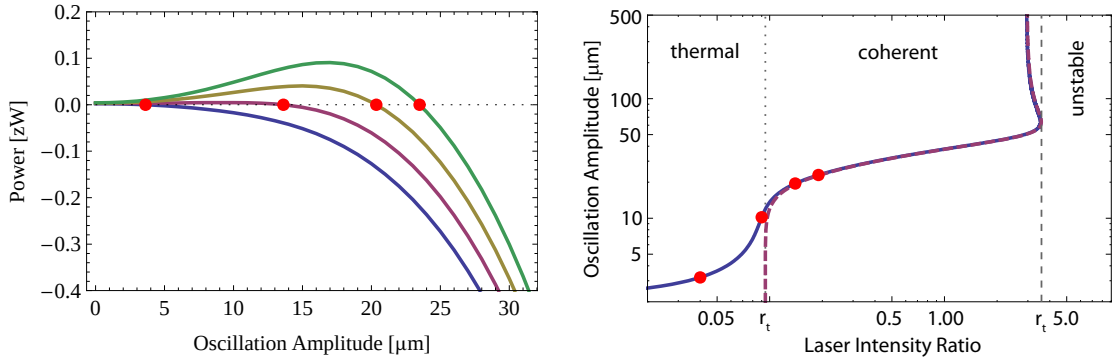

(a) (b)

Figure 3.3.: Dynamical domain $\mathcal{A}$ ($\Delta_c = -2\pi \cdot 74$ MHz, $\Delta_g = +2\pi \cdot 25$ MHz, $\omega = 2\pi \cdot 70$ kHz). (a) Plots of Eq. 3.8 for $r = s_g/s_c = 0.04$, 0.12, 0.2 and 0.28. The stable oscillation amplitude, indicated by the dots, increases for increasing intensity ratios. (b) Oscillation amplitudes where the total power is zero versus intensity ratio. The dashed line excludes spontaneous emission and allows to clearly identify the threshold to coherent oscillation. For higher intensity ratios the oscillation becomes unstable. The two vertical lines separate the three regimes: thermal, coherent, and unstable.

$\langle P \rangle_\omega = 0$, versus the corresponding intensity ratios r (full line). The dashed line is a solution excluding spontaneous emission to highlight the threshold. Note that the spontaneous emission smears out the threshold. With the intensity ratio at the threshold, r_t, and r_s where the motion becomes unstable, three dynamical regimes, thermal, coherent, and unstable can be identified. The behavior is qualitatively similar for all parameter combinations within this domain. However the "width" of the coherent plateau r_s/r_t decreases proportional to $|\Delta_c|/\Delta_g$ while the threshold steepness increases with both detunings increasing. On the transition between the two domains, the coherent plateau vanishes.

A remarkable feature of small $|\Delta_c|/\Delta_g > 1$ is bistability which implies hysteresis. No analytic expression could be found where hysteresis starts. Numerically, we find e.g. for $\omega = 2\pi \cdot 70$ kHz that hysteresis starts if $|\Delta_c| \gtrapprox 3/2\Gamma$ and $|\Delta_c| \gtrapprox \Gamma$. Figure 3.4 a and b show the mechanism for $\omega = 2\pi \cdot 70$ kHz, $\Delta_c = -2\pi \cdot 74$ MHz and $\Delta_g = +2\pi \cdot 60$ MHz: for a certain set of parameters, the mechanical power ($\langle P \rangle_\omega$) has three roots. Only the roots with a negative slope are locally stable: one in the thermal and one in the coherent regime. If no other external perturbation is present, the second stable point appears or disappears by slowly varying r, and the ion's oscillation amplitude changes to the according stable oscillation amplitude.

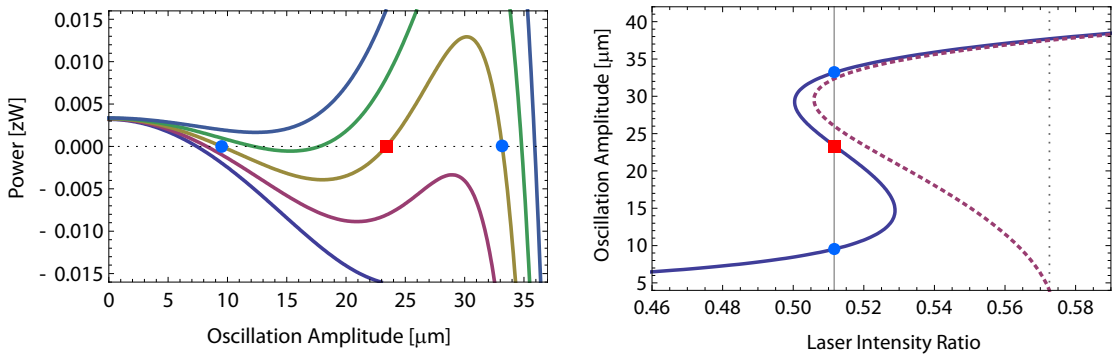

(a) (b)

Figure 3.4.: Bistability in domain $\mathcal{A}$ ($\Delta_c = -2\pi \cdot 74$ MHz, $\Delta_g = +2\pi \cdot 60$ MHz, $\omega = 2\pi \cdot 70$ kHz). (a) Plot of Eq. 3.8 for $r = 0.483$ to 0.55. A second and third root appear while two of them are stable (circles). (b) Bistability in the corresponding plot of oscillation amplitudes with a zero in power versus intensity ratio. The three roots for an exemplary intensity ratio are marked by circles (stable) and squares (unstable). The dashed line is a plot excluding spontaneous emission while the vertical dotted line marks the oscillation threshold r_t.

3.1.5. Domain $\mathcal{B}$

Except for the coherent plateau, the regimes identified in domain $\mathcal{A}$ appear in domain $\mathcal{B}$ as well but in a rather different fashion. As the plateau vanishes at the transition to this domain, the intensity ratio at threshold marks the onset of unstable motion. Figure 3.5 is a plot for $\Delta_c = -2\pi \cdot 60$ MHz, $\Delta_g = +2\pi \cdot 80$ MHz and $\omega = 2\pi \cdot 70$ kHz. A small region of bistability appears left of the threshold in a "knee". Decreasing $|\Delta_c|/\Delta_g$ pronounces the knee. The region of bistability in this knee is not accessible by slowly changing the intensity but with an external perturbation of either the intensity or the oscillation amplitude. For this reason it is difficult to experimentally access this bistability. However it is feasible to confirm the existence of this domain by showing that a stable oscillation amplitude is maintained for surprisingly high intensity ratios (Fig. 3.5 b).

3.2. Thermal distribution

To distinguish a thermal from a non-thermal oscillation we want to discuss and present observations of the basic properties of stochastic or thermal motion. We present measurements confirming its nature and show how this might find applications in the determination of the absolute ion temperature, the imaging point spread function, and the saturation parameter of the laser beam.

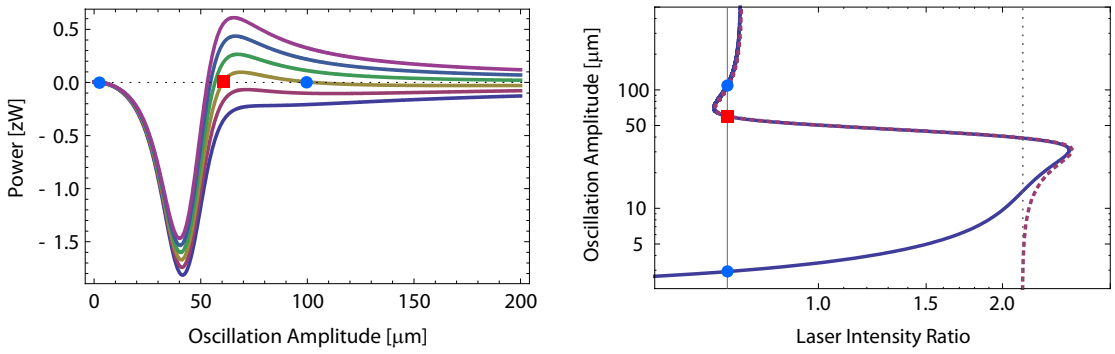

(a) (b)

Figure 3.5.: Bistability in domain $\mathcal{B}$ ($\Delta_c = -2\pi \cdot 60$ MHz, $\Delta_g = +2\pi \cdot 80$ MHz, $\omega = 2\pi \cdot 70$ kHz). (a) Cycle averaged power for $r = 0.6$ to 0.9. Note the small region of bistability. (b) Corresponding plot of all roots. The dashed line is calculated excluding spontaneous emission, the vertical dotted line marks the threshold r_t, the circles (stable) and squares (unstable) mark the roots in the power for a certain r (a) in the bistable regime.

Spatial probability distribution of a trapped ion

A laser-cooled ion has a "temperature" T (see also Sec. 1.2) in the trap potential ω. The corresponding average occupation number of the ion in a harmonic potential reads [17]

$$\overline{n} = \frac{1}{\exp\left(\frac{\hbar\omega}{k_b T}\right) - 1}. \tag{3.10}$$

For a temperature $T = 1$ mK and $\omega = 2\pi \cdot 50$ kHz we obtain $\overline{n} \approx 400$. Each motional state n is populated with a probability [17]

$$P_n = \frac{\overline{n}^n}{(\overline{n}+1)^{n+1}}. \tag{3.11}$$

We calculate the thermal distribution by summing up the individual quantum mechanical wave functions for $n = 0..20\ \overline{n}$. The resulting distribution is to a very good approximation Gaussian and agrees with the classical description of Brownian motion in a harmonic potential [44]. Here a harmonic oscillator of mass m, and temperature T in a harmonic potential ω will have a Gaussian distribution with a root-mean-square displacement z_{RMS}

$$E_{thermal} = E_{osc} \Rightarrow k_B T = m\omega^2 z_{RMS}^2 \Rightarrow z_{RMS} = \sqrt{\frac{k_b T}{m\omega^2}}. \tag{3.12}$$

For $T = 1$ mK and $\omega = 2\pi \cdot 17$ kHz, we obtain $z_{RMS} = 13\ \mu$m. Since our imaging system has a point spread function (PSF) of $\approx 2\ \mu$m, we are able to resolve this

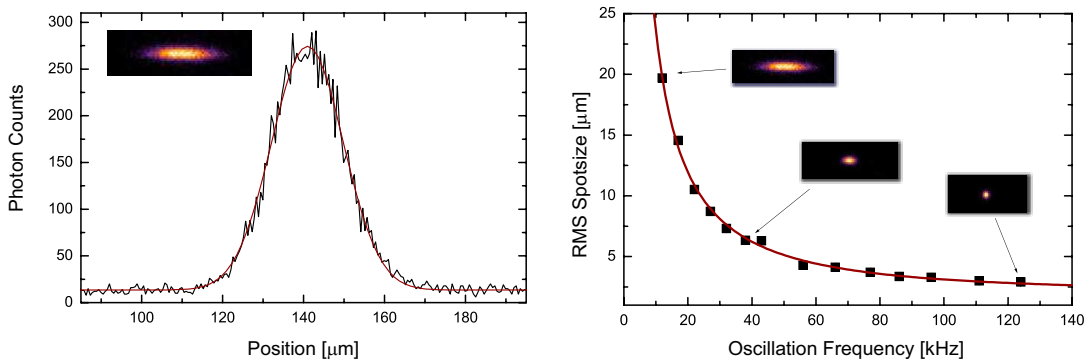

(a) (b)

Figure 3.6.: (a) Spatial probability distribution of the image of a single ion ($\omega = 2\pi \cdot 17$ kHz, $T \approx 1$ mK). It demonstrates the characteristics of a thermal distribution, the line is a Gaussian fit. (b) Temperature measurement using the thermal spread/distribution of the ion: measurement of the widths versus $\omega/2\pi$. The insets show examples of the corresponding images. From the fit of Eq. 3.12 we obtain an ion temperature of 1.1(1) mK and a camera PSF of 1.7(1) μm.

thermal distribution/spread. Assuming a Gaussian PSF the resulting width of the ion will be

$$z_{spread} = \sqrt{z_{PSF}^2 + z_{thermal}^2}. \tag{3.13}$$

If the temperature stays constant, the thermal distribution will change with varying ω.

To study this thermal distribution, we have performed experiments using the 4-rod ion trap (Sec. 2.1.2). Both laser beams (Sec. 2.2) have equal, negative detunings. The radial laser cools the radial motion of the ion, the axial laser the axial motion which we consider in the following. We take images with an integration time of 40 s for several axial oscillation frequencies ($\omega = \omega_z$, Sec. 1.1.2) which we define by the voltage on the two inner rings (Sec. 2.1.2). Figure 3.6 a shows a histogram of an exemplary ion image for $\omega = 2\pi \cdot 17$ kHz with a Gaussian fit. If we measure the widths for several ω, we obtain Fig. 3.6 b. The laser detuning was $\Delta = -2\pi \cdot 13.3$ MHz and the intensity $s \lessapprox 0.1$, the line is a fit of Eq. 3.12 to the data from which we obtain the ion temperature $T = 1.1(1)$ mK and the camera PSF $z_{PSF} = 1.7(2)$ μm. Note that the thermal spatial probability distribution allows to measure the absolute temperature of the trapped ion as well as the camera PSF.

Figure 3.7 a shows such absolute temperature measurements (Fig. 3.6 b) for several detunings where the squares are measured data and the circles are theoretical calculations using Eq. 1.22. The temperature depends on the detuning and the laser intensity (Fig. 1.5, Eq. 1.22). Qualitatively, the experiment follows the characteristics of theory but the temperature seems to have an offset. This is subject to further

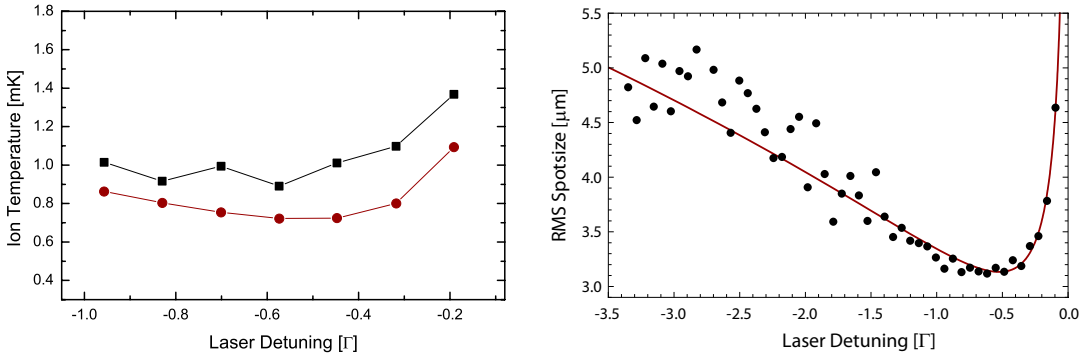

(a) (b)

Figure 3.7.: (a) Temperature measurements for various detunings (squares) and theoretical temperatures (circles). The offset is most likely due to the non-dipolar radiation characteristic and inappropriate laser polarization. (b) Measurement of the ion width (temperature) for $s \lessapprox 0.1$ depending on the detuning together with a fit of Eq. 1.22. The minimum width and therefore temperature can be identified at $\approx \Gamma/2$ as expected from Eq. 1.24.

studies and most likely due to the radiation characteristics ($\xi \neq 2/5$, Sec. 1.2) since the transition is not a perfect two-level system and we did not ensure the right polarization of the laser (Zeeman splitting of the sub levels). Another origin of the deviation might be (the coupling of) radial and axial micromotion. However this temperature measurement is much more precise than most other methods employed so far in the weak binding limit e.g. linewidth analysis [45] and rough estimates using the thermal distribution [46]. Also it confirms the presence and characteristics of thermal motion.

In a second measurement we consecutively varied the laser detuning. Figure 3.7 b shows a plot of the resulting RMS spread together with a fit of Eq. 3.13 (Eqs. 1.22, 3.12). We find excellent agreement with theory. From the fit we obtain the camera PSF $z_{PSF} = 1.87(5)$ μm and the saturation parameter $s = 0.079(4)$ with the statistical error bars of the fit. The minimal temperature, hence minimal thermal spread, is identified at $\approx \Gamma/2$ in agreement with Eq. 1.24. The slight systematic disagreement is most likely due to the varying radiation pressure from the laser, which pushes the ion into regions of higher micromotion. This is, to our knowledge, the first extensive measurement of the temperature dependence of the ion temperature on the cooling laser frequency.

We want to point out that these measurements are feasible due to the unique design of the 4-rod ion trap which allows to work with very weak axial confinement to optically resolve and study the thermal distribution.

These observations highlight the characteristics and usability of the thermal distribution. It is Gaussian and its width depends on the potential and the temperature.

Next, we want to present data of coherent oscillations, which have much different properties.

3.3. Observation of laser-driven ion oscillations

Following the theoretical treatment and the introduction of thermal motion in an ion trap we now want to present observations of laser-driven ion oscillations.

3.3.1. Experimental procedures

To explore the parameter space of the laser-driven ion oscillations, we follow a simple scheme: We record a set of images where the gain laser intensity is increased in approximately equal steps (compare to Fig. 3.3 b). All other parameters, the laser detunings, the oscillation frequency and the intensity of the cooling laser, are kept constant.

In these first measurements, we use the endcap trap (Sec. 2.1.1), whose trapping frequencies are $\omega_r \approx 2\pi \cdot 800$ kHz and $\omega = \omega_z \approx 2\pi \cdot 60$ kHz. The axial frequency $\omega = \omega_z$ changed from day to day by ± 10 kHz. Both lasers are stabilized in frequency and intensity. Since we cannot determine absolute intensities precisely enough we measure the intensity ratio $r = s_g/s_c$ instead. The intensity ratio is obtained by comparing the scattering rate of each beam at a common, negative detuning while their intensities are locked. Both beams are optimized for uniform intensity distribution over the trapping region with a long chain of ions using the histogram feature of the camera software (Sec. 2.4.1). After this adjustment, the driven ion oscillations are investigated on a single ion.

Each data point consists of an image and an intensity ratio. Image integration time is 40 s. The images are translated into histograms of which the RMS oscillation amplitudes are obtained using the evaluation software (Sec. 2.4.2).

3.3.2. Experimental data

Figure 3.8 shows as an example a series of images of the single ion where the blue-detuned gain laser is oriented in horizontal direction. The intensity ratio $r = s_g/s_c$ increases towards the bottom. A threshold from thermal to coherent oscillation is apparent with the emergence of a double-lobed pattern as the motion is driven by the blue-detuned gain laser. Since the ion spends more time at the turning points of the oscillation, the two bright lobes, they appear brighter. From the large image exposure time of 40 s which constitutes an average over $\approx 2 \cdot 10^6$ oscillation cycles, we deduce that this motion is stable and uniform. This implies that the gain by the blue-detuned laser saturates. The three insets in Fig. 3.8 show exemplary image histograms of the axial spatial probability distribution of the ion: Gaussian

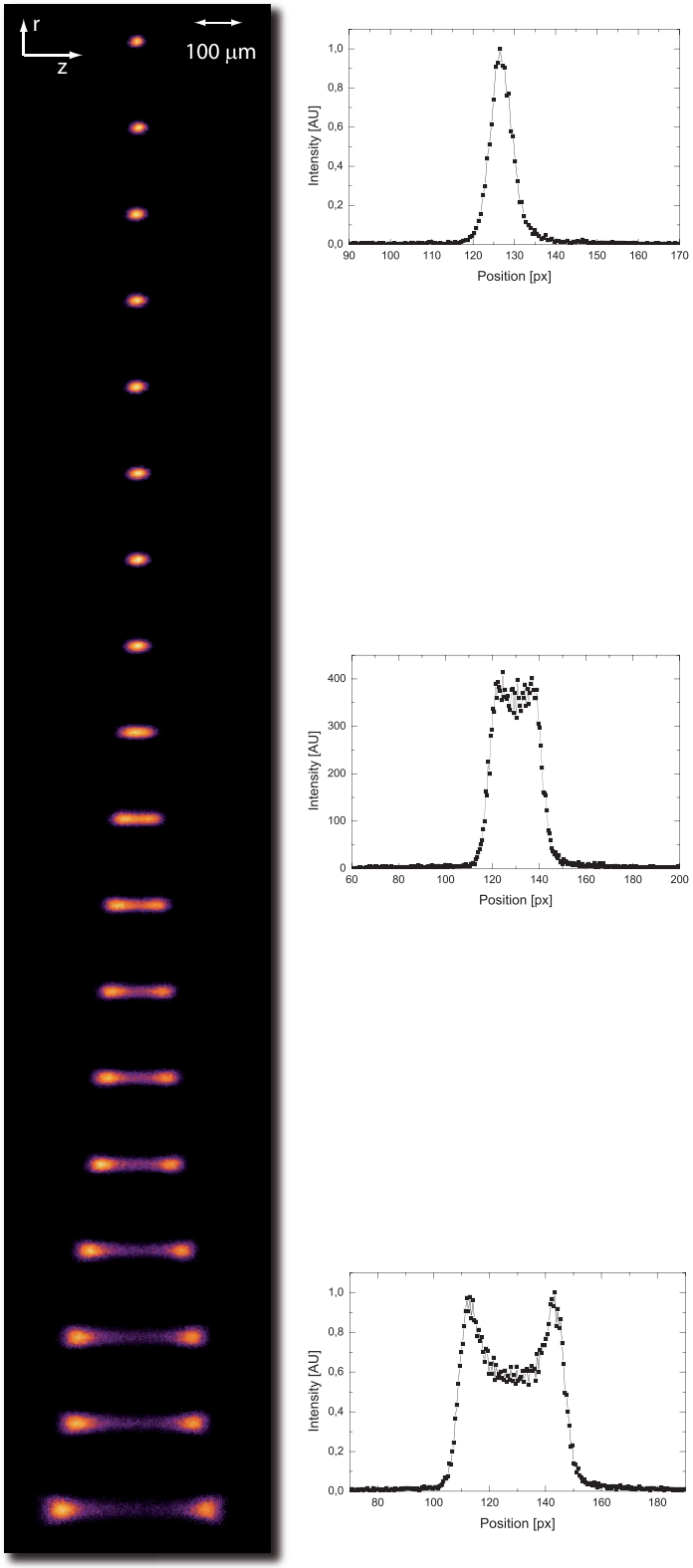

Figure 3.8: Series of images where the gain laser intensity is increased from top to bottom. The threshold from thermal to coherent motion is observed in the emergence of a double-lobed pattern. Since the ion spends more time at the turning points of the oscillation, the two lobes appear brighter. The insets on the right show exemplary image histograms highlighting the difference between the Gaussian thermal distribution below threshold and the double-lobed pattern characteristics of the coherent motion above threshold.

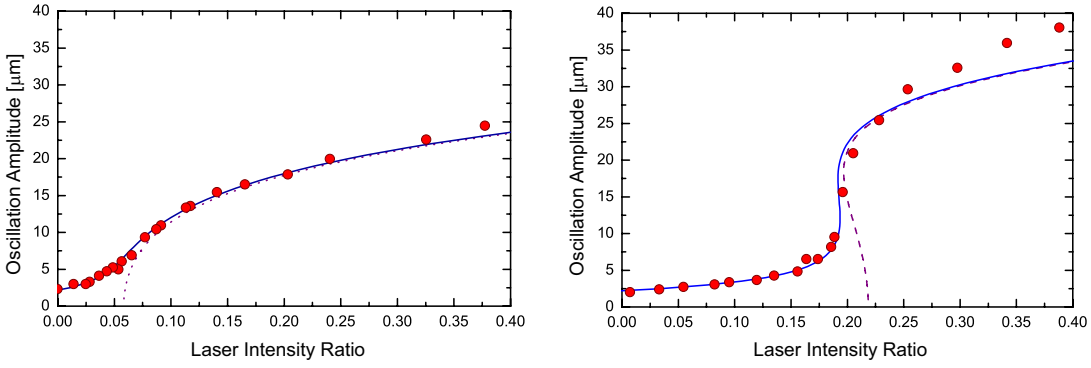

Figure 3.9.: Experimental data of the ion oscillation for $\omega = 2\pi \cdot 71$ kHz, $\Delta_c = -2\pi \cdot 74$ MHz, $\Delta_g = +2\pi \cdot 12$ MHz (a) and $\Delta_g = +2\pi \cdot 40$ MHz (b). The lines are calculated using ab initio theory without adjustable parameters (Sec. 3.1). For the dashed line we excluded spontaneous emission. The data is slightly shifted to compensate for the miscalibration of the intensity ratio axis. Note that the threshold is pronounced for larger Δ_g (b).

in the thermal regime (left), an intermediate state, and a double-lobed pattern in the coherent regime (right).

Figure 3.9 shows measured oscillation amplitudes in comparison with ab initio theory for $\omega = 2\pi \cdot 71$ kHz, $\Delta_c = -2\pi \cdot 74$ MHz, $\Delta_g = +2\pi \cdot 12$ MHz (Fig. 3.9 a) and $\Delta_g = +2\pi \cdot 40$ MHz (Fig. 3.9 b). The lines are the ab initio theory calculations (Sec. 3.1) where for the dotted lines spontaneous emission has been excluded. To match the calculations, we have shifted the data points to compensate for imperfect calibration of the intensity axis. This miscalibration is mostly due to the detector nonlinearities of our camera. For small amplitudes the agreement is excellent. Unfortunately we cannot maintain spatial uniformity of the laser beams for larger oscillation amplitudes. Here the laser intensity drops (approximately Gaussian intensity profile) which leads to oscillation amplitudes larger than expected by theory. Note that the threshold is pronounced for larger detuning Δ_g (Fig. 3.9 b).

3.3.3. Hysteresis

Looking at another interesting parameter region of the laser-driven ion oscillator we report on the observation of hysteresis. Here we slowly increased the intensity ratio from below threshold to above threshold and vice versa for small $|\Delta_c|/\Delta_g > 1$. Figure 3.10 shows a measurement with $\omega = 2\pi \cdot 68$ kHz, $\Delta_c = -2\pi \cdot 74$ MHz and $\Delta_g = +2\pi \cdot 50$ MHz. The dots are for increasing the intensity ratio r, the circles for the opposite direction. The hysteresis emerging from the nonlinearity of the Voigt line profile (Sec. 3.1.4) is clearly observable. Due to the very high oscillation

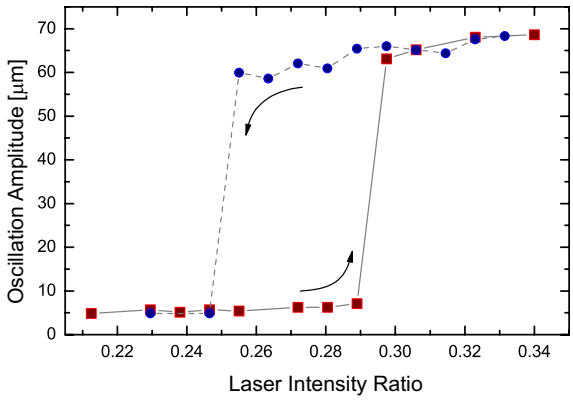

Figure 3.10.: Observation of hysteresis with $\omega = 2\pi \cdot 68$ kHz, $\Delta_c = -2\pi \cdot 74$ MHz and $\Delta_g = +2\pi \cdot 50$ MHz. For the squares we increased the intensity ratio starting below threshold to above threshold, for the circles vice versa.

amplitudes (compare to Fig. 3.8), we cannot maintain spatial uniformity of the laser intensities, thus ab initio theory delivers qualitative agreement only.

3.4. A trapped-ion phonon laser

The stable oscillations we observe by the double-lobed pattern are fundamentally different from a Gaussian thermal distribution (compare to Sec. 3.2). Similar to optical lasers, our system can be described semiclassically by means of a Van-der-Pol oscillator [43, 5]: It is subject to a threshold (2nd-order phase transition) from thermal motion to (coherent) oscillations, similar to the lasing threshold in optical lasers [43, 42, 29], and to amplification saturation. Here we want to outline an alternative approach to trapped-ion oscillators to show that our system can be described by a nonlinear Van der Pol equation that coincides with the theory outlined in Sec. 3.1. Further, we demonstrate that this coherent motion of the trapped ion is sustained by stimulated generation of phonons by the blue-detuned laser.

The equation of motion of the single trapped ion interacting with the two lasers reads [5]

$$m\ddot{z} = -m\omega^2 z + F_c + F_g + m\chi(t) \tag{3.14}$$

where the first term on the right hand side is the force due to the trapping potential, $F_c = \hbar k g(s_c, \delta_{eff,c}(v,t))$ and $F_g = \hbar k g(s_g, \delta_{eff,g}(v,t))$ (compare to Eq. 1.19) are the forces of the cooling and the gain laser beam, and $\chi(t)$ is a white-noise Langevin function that accounts for noise from several sources including spontaneous emission. Taking the time derivative of Eq. 3.14 and dividing by m we obtain the following nonlinear oscillator equation driven by $\chi(t)$ [5]

$$\ddot{v} + [\mathfrak{k}(v) - \mathfrak{g}(v)]\dot{v} + \omega^2 v = \dot{\chi}(t) \tag{3.15}$$

where $v = \dot{z}$ is the time dependent velocity of the ion in z-direction, ω is the frequency of the ion oscillation and $\mathfrak{k}(v) = \partial F_c/\partial v\mathrm{m}$ and $\mathfrak{g}(v) = \partial F_g/\partial v m$ are the derivatives with respect to v of the forces due to the cooling and gain laser (Eq. 1.19) [5]. This equation has the form of a Van der Pol oscillator [43, 5]. Next, we want to show that this approach coincides with the theory derived in Sec. 3.1.

Substituting $v = v_0 \cos(\omega t + \phi)$ with slowly time dependent v_0 and ϕ into Eq. 3.15, keeping only leading order terms (i.e., $\dot{v}_0 \ll \omega v_0$ and $\dot{\phi} \ll \omega$), we obtain [5]

$$\begin{aligned} \dot{v}_0 \sin(\omega t + \phi) + v_0 \dot{\phi} \cos(\omega t + \phi) = -\frac{1}{2\omega}\dot{\chi}(t) + \\ -\frac{1}{2}[\mathfrak{k}(v) - \mathfrak{g}(v)] \left(v_0 \sin(\omega t + \phi) - \frac{\dot{v}}{\omega} \cos(\omega t + \phi) \right). \end{aligned} \tag{3.16}$$

If we multiply this equation with $\sin(\omega t + \phi)$ and $\cos(\omega t + \phi)$, respectively, and integrate over one oscillation cycle, using the slowly varying approximation where

$$\begin{aligned} &\int_t^{t+2\pi/\omega} dt' \dot{v}_0(t') \sin^2(\omega t' + \phi(t')) \approx \\ &\quad \approx \dot{v}_0(t) \int_t^{t+2\pi/\omega} dt' \sin^2(\omega t' + \phi(t)) = \frac{\pi}{\omega}\dot{v}(t) \end{aligned} \tag{3.17}$$

$$\begin{aligned} &\int_t^{t+2\pi/\omega} dt' v_0(t') \dot{\phi}(t') \sin^2(\omega t' + \phi(t')) \approx \\ &\quad \approx v_0(t)\dot{\phi}(t) \int_t^{t+2\pi/\omega} dt' \cos^2(\omega t' + \phi(t)) = \frac{\pi}{\omega} v_0(t)\dot{\phi}(t) \end{aligned} \tag{3.18}$$

$$\begin{aligned} &\int_t^{t+2\pi/\omega} dt' \mathfrak{g}[v_0(t') \cos(\omega t' + \phi(t')] \sin^2(\omega t' + \phi(t')) \approx \\ &\quad \approx \int_0^{2\pi/\omega} dt'' \mathfrak{g}[v_0(t) \cos(\omega t'')] \sin^2(\omega t''), \end{aligned} \tag{3.19}$$

we obtain the equation of motion and the phase equation [5]

$$\dot{v} = -\frac{1}{2}[\mathfrak{K}(v_0) - \mathfrak{G}(v_0)]v_0 + \zeta(t) \tag{3.20}$$

$$\dot{\phi} = \frac{1}{2\omega}[\mathfrak{K}'(v_0) - \mathfrak{G}'(v_0)]\dot{v}_0 + \zeta'(t). \tag{3.21}$$

Here the cycle-averaged amplification, damping and Langevin forces read [5]

$$\begin{pmatrix} \mathfrak{G}(v_0(t)) \\ \mathfrak{K}(v_0(t)) \end{pmatrix} \equiv \frac{\omega}{\pi}\int_0^{2\pi/\omega} dt' \begin{pmatrix} \mathfrak{g}(v_0(t)\cos(\omega t')) \\ \mathfrak{k}(v_0(t)\cos(\omega t')) \end{pmatrix} \sin^2(\omega t') \tag{3.22}$$

$$\begin{pmatrix} \mathfrak{G}'(v_0(t)) \\ \mathfrak{K}'(v_0(t)) \end{pmatrix} \equiv \frac{\omega}{\pi}\int_0^{2\pi/\omega} dt' \begin{pmatrix} \mathfrak{g}(v_0(t)\cos(\omega t')) \\ \mathfrak{k}(v_0(t)\cos(\omega t')) \end{pmatrix} \cos^2(\omega t') \tag{3.23}$$

$$\zeta(t) = -\frac{\omega}{2\pi}\int_t^{t+2\pi/\omega} dt' \dot{\chi}(t')\sin(\omega t') \tag{3.24}$$

$$\zeta'(t) = -\frac{\omega}{2\pi\bar{v}_0}\int_t^{t+2\pi/\omega} dt' \dot{\chi}(t')\cos(\omega t') \tag{3.25}$$

where $\bar{v}$ is the time-averaged amplitude. Note that $\mathfrak{K}(0) = \mathfrak{k}(0)$ and $\mathfrak{G}(0) = \mathfrak{g}(0)$. By partial integration, we obtain the following equivalent form of $\mathfrak{G}$ and $\mathfrak{K}$

$$\begin{pmatrix} \mathfrak{G}(v_0) \\ \mathfrak{K}(v_0) \end{pmatrix} \equiv \frac{\omega}{\pi m v_0}\int_0^{2\pi/\omega} dt' \begin{pmatrix} F_g(v_0\cos(\omega t')) \\ -F_c(v_0\cos(\omega t')) \end{pmatrix} \cos(\omega t'), \tag{3.26}$$

with $F_i = \hbar k g(s_i, \delta_{eff,i})$ (Eq. 1.19) as above. If we multiply Eq. 3.20 with mv_0, we obtain the dynamical equation for the cycle-averaged oscillator energy $E = mv_0^2/2$ [5]

$$\dot{E} = -[\mathfrak{K}(E) - \mathfrak{G}(E)]E + \mathfrak{S}_c + \mathfrak{S}_g, \tag{3.27}$$

where we normalized the cycle-averaged Langevin function $\zeta(t)$ with the well-known scattering powers due to the blue- and red-detuned laser ([2], Eq. 1.21), $\mathfrak{S}_c = \langle P_{s,c}\rangle_\omega$, and $\mathfrak{S}_g = \langle P_{s,g}\rangle_\omega$ (compare to Eq. 1.21). An alternative approach to derive the oscillator energy would be to begin with operator Langevin equations for all quantities. Since $\mathfrak{K}(E)E = \langle P_{s,c}\rangle_\omega$ and $\mathfrak{G}(E)E = \langle P_{a,g}\rangle_\omega$ (Eq. 3.5), Eq. 3.27 is equal to Eq. 3.7. Therefore our approach to the trapped-ion phonon laser taken in Sec. 3.1 coincides with the approach above, the trapped-ion phonon laser can be described by means of a Van der Pol oscillator or a laser oscillator [5] in agreement with our observations (Secs. 3.3 and 4.1).

The Hamiltonian for the interaction of the blue-detuned laser with the ion (in the resolved sideband, small-signal-regime limit) is $H = Va\sigma^+(b + b^\dagger) + h.a.$ [17], with the interaction potential $V = \hbar\Omega_R k\sqrt{\hbar/8m\omega}$ where Ω_R is the vacuum Rabi frequency, the phonon (photon) destruction operator b (a), and the two-level Pauli raising operator σ^+. An illustration of the according generation and destruction of phonons in our system is sketched in Fig. 3.11; A blue-detuned photon can generate or destroy a center-of-mass phonon. With the scattering rate $g(s_g, \delta_g)$ (Eq. 3.4), and using Fermi's golden rule [47], we obtain the rate equations [5]:

$$R^+ = \beta g(s_g, \Delta_g - \omega)(n+1) \tag{3.28}$$

$$R^- = \beta g(s_g, \Delta_g + \omega)(n). \tag{3.29}$$

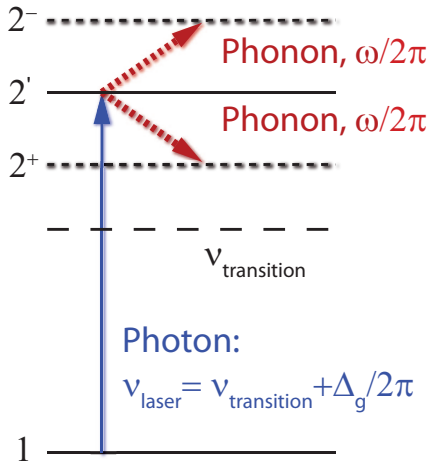

Figure 3.11.: Generation and destruction of phonons by a blue-detuned laser photon.

Here R^+ is the rate for the generation, R^- the rate for the destruction of a phonon. Furthermore, $\beta = \hbar k^2/2m$ and n is the number of phonons in the oscillation mode. Note that R^+ consists of two parts: a stimulated part which is proportional to n and a constant, spontaneous part. Subtracting the two rates, the phonon number rate equation reads

$$\dot{n} = (R^+ - R^-) = \beta \left[g(s_g, \Delta_g - \omega) - g(s_g, \Delta_g + \omega) \right] \; n + \xi \tag{3.30}$$

with $\xi = \beta g(s_g, \Delta_g - \omega)$, the spontaneous phonon generation rate. The coefficient n in Eq. 3.30 incorporates the phonon amplification. We consider that this is also the case in the weak binding limit, where the change in phonon number reads [5]

$$\dot{n}_{wb} = \lim_{\omega \to 0} (R^+ - R^-) = \mathfrak{g}(v = 0) \; n + \xi = \mathfrak{G}(v = 0) \; n + \xi. \tag{3.31}$$

where $\mathfrak{g}$ and $\mathfrak{G}$ incorporate the gain due to the amplification laser (Eqs. 3.22, 3.15) [5] and $\mathfrak{g}(0) = \mathfrak{G}(0)$ as identified in (Eq. 3.22). The fact that the change in phonon number $\dot{n}$ is proportional to the phonon number present in the mode n, $\dot{n}_{wb} \sim \dot{n} \propto n$, shows that the amplification is the result of stimulated generation of phonons. If phonons are present in the mode already, the new phonon is emitted in phase with the existing phonon, amplification by stimulated emission is obtained. If the phonons would be emitted spontaneously, no amplification but random heating would take place and a thermal distribution would be observed (Sec. 3.2). In this context, this system is similar to a Raman laser [48], the stimulated phonons are emitted into a (Stokes) sideband. Note that in such a system inversion is not required for laser operation.

Summary

We have demonstrated the following parallels to an optical laser:

- Threshold from thermal motion to coherent oscillations
- The oscillation starts from noise and is sustained by stimulated emission
- The oscillation is stable due to gain saturation,

and the following differences:

- No phonons are emitted - laser without output coupler
- No population inversion - similar to Raman laser.

We find excellent agreement of experiment and theory and want to point out that based on the simplicity and controllability of our system, this has been the first reported observation of phonon laser action.

Recently, phonon laser action has been observed in coupled microtoroids [49] which form a two level phonon laser. Furthermore, coherent phonon amplification has been reported for GaAs/AlAs superlattices [50]. Both experiments support the findings of this work that phonon laser action is indeed possible and promise the development of an interesting new field.

4. Injection locking and the detection of ultra-weak forces

In this chapter we present theory and observation of injection locking of a trapped-ion phonon laser to an external signal. This implies the detection of ultraweak forces which is discussed and demonstrated in the second part.

4.1. Injection locking of a trapped-ion phonon laser

When injecting a weak harmonic signal, a stronger self-sustained oscillator at sufficiently close frequency can be forced to (phase) synchronize with the injected signal. This has first been described in mechanical clocks by Christiaan Huygens in 1665 [51]. In fact, this process plays a crucial role in nature [52], including e.g. the time-scale adjustment of the circadian system to light [53] or the synchronization of the cardiac system to a pacemaker [54]. Apart from that, it has found numerous applications in science and technology in systems as diverse as organ pipes [55], solid-state oscillators [56], optomechanical rf oscillators [57], and optical lasers [58].

The intention to reveal further parallels between a trapped-ion phonon laser and an optical laser, and to coherently manipulate this phonon laser from outside gave rise to the idea of injection locking of this oscillator to an external signal. These measurements should answer two questions: First, can we deepen the analogy to an optical laser with injection locking as well, and second, can we coherently manipulate this phonon laser from outside.

In this section, we outline the general theory of injection locking and provide a derivation of the central injection locking equation, the Adler equation, for a trapped-ion phonon laser. Further, we present our observations on injection locking of a trapped-ion phonon laser to an external signal based on motional spectra and relative phase measurements.

4.1.1. General theory of injection locking

An excellent overview of the theory of injection locking is given in [29]. Here, we compile a compact review. Consider a self-excited or regenerative oscillator of free-running frequency ω_0, amplitude A_0 and intrinsic linewidth γ_e. A weak signal of

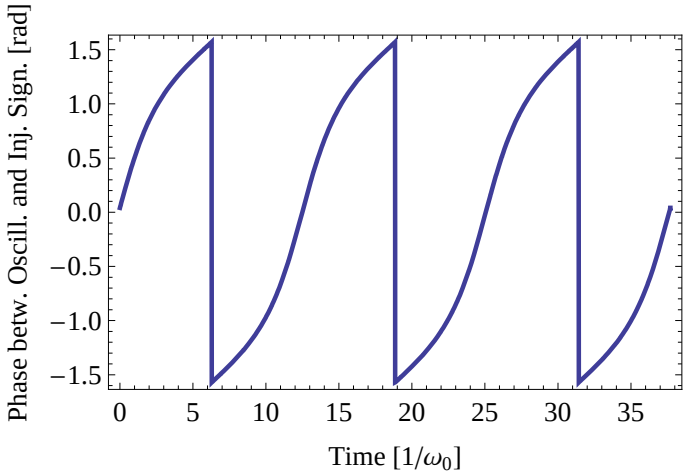

Figure 4.1.: Plot of Eq. 4.5 far outside the locking range ($\omega_i = \omega_0/2$ and $\omega_m = \omega_0/100$).

frequency ω_i and amplitude A_i ($A_i \ll A_0$) is injected into the regenerative oscillator. For $\omega_i \neq \omega_0$, the injected signal is amplified by something similar to

$$|g(\delta)|^2 \approx \frac{\gamma_e^2}{\delta^2} \tag{4.1}$$

where the detuning $\delta = \omega_i - \omega_0$ is the frequency difference between the injected signal and the free-running oscillator. From this follows that as the detuning decreases, the injected signal takes more of the limited gain provided by the regenerative oscillator. The gain at the free-running component decreases accordingly. As the oscillation at the free-running frequency drops below threshold, oscillation at the injected frequency prevails–the oscillator is injection locked to the external signal. Since $A_i \ll A_0$, the amplitude of the oscillator stays approximately unchanged in this process. This allows to focus the discussion on the phase of the oscillator.

The Adler equation

The phase $\phi(t)$ between the regenerative oscillator and the injected signal in the transient as well as in the steady state is described by the Adler equation [59]

$$\frac{d\phi(t)}{dt} + \delta = -\omega_m \sin(\phi(t)), \tag{4.2}$$

where ω_m denotes half the locking range. For most systems it reads [29, 57, 59]

$$\omega_m = \gamma_e \frac{A_i}{A_0} = \frac{m}{Q_e}\frac{A_i}{A_0}. \tag{4.3}$$

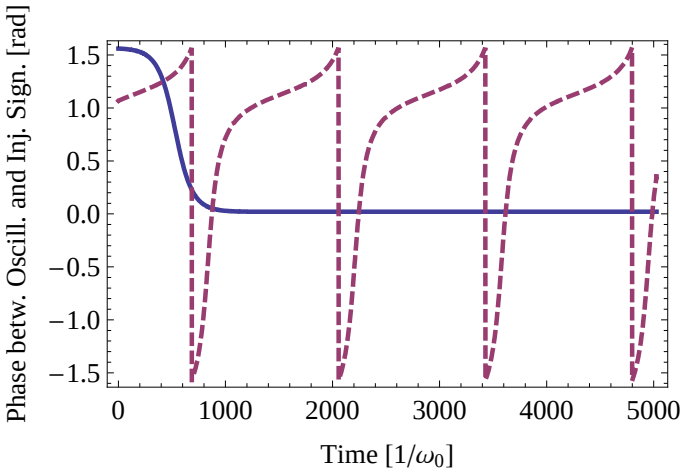

Figure 4.2.: Evaluation of Eq. 4.5 for ω_i very close to the locking range (dashed) and inside the locking range $\omega_i = \omega_0$ (full) with $\omega_m = \omega_0/100$. A phase pull-in behavior close to the locking range manifests itself in an asymmetry while inside the phase is fixed after a short period of time.

Apart from the mass m and the inverse intrinsic quality factor Q_e it is proportional to the ratio of the two amplitudes. An expression for ω_m in terms of conveniently measurable quantities of our system will be derived in Sec. 4.1.2.

Inside the locking range ($|\delta| < \omega_m$) the phase is expected to be constant thus $d\phi(t)/dt = 0$. With this assumption, a solution of Eq. 4.2 inside the locking range can be found to read

$$\phi(\delta) = \arcsin\left(-\frac{\delta}{\omega_m}\right). \tag{4.4}$$

The phase varies from $\pi/2$ to $-\pi/2$ with δ being tuned from $-\omega_m$ to $+\omega_m$ and changes sign at $\delta = 0$.

Outside the locking range ($|\delta| > \omega_m$), a solution of Eq. 4.2 yields a time-dependent phase of the oscillator [29]

$$\phi(t) = 2\arctan\left[-\frac{\omega_b}{\delta}\tan\frac{\omega_b(t-t_0)}{2} - \frac{\omega_m}{\delta}\right], \tag{4.5}$$

where t_0 incorporates the initial conditions and the time-averaged phase advance reads $|\langle d\phi/dt\rangle| = \omega_b = \sqrt{\delta^2 - \omega_m^2}$. This indicates a pulling of the oscillator frequency ω towards the injected frequency ω_i

$$\omega = \omega_i - \mathrm{sgn}(\delta)\omega_\mathrm{b} \approx \omega_0 + \frac{\omega_\mathrm{m}^2}{2\delta}. \tag{4.6}$$

The approximation holds for large detunings. Figure 4.1 shows the phase dynamics following Eq. 4.5 for ω_i far outside the locking range where no influence of the injected

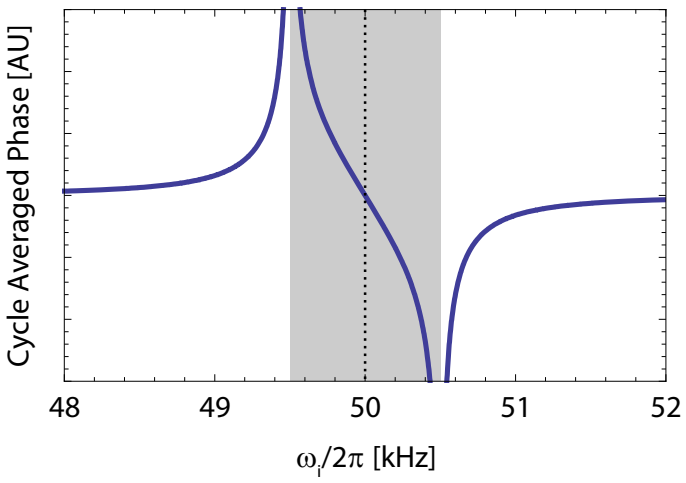

Figure 4.3.: Integration of Eq. 4.5 over one oscillation period. The shaded area marks the locking range, the dotted line ω_0. The phase pull-in behavior outside the locking range as well as a arcsin dependence inside the locking range is apparent.

signal can be observed. In Fig. 4.2 the dashed line is plotted for the injected signal very close to the locking range while for the full line $\omega_i = \omega_0$. Close to the locking range, the phase pull-in behavior manifests itself in an asymmetry of the relative phase evolution. Inside the locking range, the phase is fixed after a short period of time.

In our experiments, we observe the time-averaged phase difference. Integrating Eq. 4.5 over one oscillation cycle, the time-averaged phase dependence is found (Fig. 4.3). With ω_i outside the locking range (shaded) the phase pull-in behavior is apparent while inside the locking range the relative phase follows an arcsin according to Eq. 4.4.

4.1.2. Theory of injection locking of a trapped-ion phonon laser

For some of the quantities used in the discussion of injection locking so far, there are no straightforward correspondences in a trapped ion (A_i). We therefore re-derived the Adler equation for our system.

We start with the nonlinear equation of motion of the trapped-ion phonon laser, Eq. 3.15 [5]

$$\ddot{v} + [\mathfrak{k}(v) - \mathfrak{g}(v)]\dot{v} + \omega_0^2 v = \dot{\chi}(t). \tag{4.7}$$

Here, we have replaced ω with the free-running frequency ω_0 of the oscillator. We assume that the noise term due to spontaneous emission, $\chi(t)$ incorporates an injected force $F(t) = eE_i \cos(\omega_i t)$ instead, where E_i is the electric field amplitude at

the position of the ion and ω_i is the frequency of the injected signal. For simplicity we neglect spontaneous emission. The derivative of $\chi(t) = F(t)$ reads

$$\dot{\chi}(t) = \dot{F}(t) = -\frac{eE_i\omega_i}{m}\sin(\omega_i t). \tag{4.8}$$

For the injection-locked oscillator we use the following ansatz (Sec. 3.4)

$$v(t) = v_0\cos(\omega_i t + \phi) \tag{4.9}$$

with time dependent v_0 and ϕ. In the injection-locked case $\dot{\phi} = 0$, and for the free-running oscillator $\dot{\phi} = \omega_0 - \omega_i$. The derivatives read

$$\begin{aligned}
\dot{v}(t) &= \dot{v}_0\cos(\omega_i t + \phi) - v_0(\omega_i + \dot{\phi})\sin(\omega_i t + \phi) && (4.10)\\
\ddot{v}(t) &= \ddot{v}_0\cos(\omega_i t + \phi) - 2\dot{v}_0(\omega_i + \dot{\phi})\sin(\omega_i t + \phi) \\
&\quad -v_0\ddot{\phi}\sin(\omega_i t + \phi) - v_0(\omega_i + \dot{\phi})^2\cos(\omega_1 t + \phi). && (4.11)
\end{aligned}$$

When inserted into Eq. 4.7, we obtain

$$\begin{aligned}
&\cancel{\ddot{v}_0(t)\cos(\omega_i t + \phi)} - 2\dot{v}_0\left(\omega_i - \cancel{\dot{\phi}}\right)\sin(\omega_i t + \phi) \\
&\cancel{-v_0\ddot{\phi}\sin(\omega_i t + \phi)} - v_0\left(\omega_i^2 + \dot{\phi}\left(2\omega_i + \cancel{\dot{\phi}}\right)\right)\cos(\omega_i t + \phi) \\
&+[\mathfrak{k}(v) - \mathfrak{g}(v)]\left(\dot{v}\cos(\omega_i t + \phi) - v_0\left(\omega_i + \cancel{\dot{\phi}}\right)\right)\sin(\omega_i t + \phi) \\
&+v_0\omega_0^2\cos(\omega_i t + \phi) = -\frac{eE_i\omega_i}{m}\sin(\omega_i t). && (4.12)
\end{aligned}$$

As pursued in [29], Chapter 24.4, we use the slowly varying amplitude and phase approximation $\dot{v}_0 \ll \omega_i v_0$, $\dot{\phi} \ll \omega_i$, $\ddot{v}_0 \ll \omega_i\dot{v}_0$ and $\ddot{\phi} \ll \omega_i\dot{\phi}$ whose contribution we crossed out above. We obtain

$$\begin{aligned}
&\dot{v}_0\sin(\omega_i t + \phi) + v_0\dot{\phi}\cos(\omega_i t + \phi) + v_0\frac{\omega_i^2 - \omega_0^2}{2\omega_i}\cos(\omega_i t + \phi) \\
= \quad &-\frac{1}{2}[\mathfrak{k}(v) - \mathfrak{g}(v)]\left(v_0\sin(\omega_i t + \phi) - \frac{\dot{v}}{\omega_i}\cos(\omega_i t + \phi)\right) \\
&+\frac{eE_i}{2m}\sin(\omega_i t). && (4.13)
\end{aligned}$$

This matches Eq. 3.16 except for the the last term with the external force and the term with $\frac{\omega_i^2-\omega_0^2}{2\omega_i}$ which can be approximated by

$$\frac{\omega_i^2 - \omega_0^2}{2\omega_i} = \frac{(\omega_i + \omega_0)(\omega_i - \omega_0)}{2\omega_i} \approx \frac{2\omega_i(\omega_i - \omega_0)}{2\omega_i} = \omega_i - \omega_0. \tag{4.14}$$

Following Sec. 3.4, we multiply Eq. 4.13 with $\sin(\omega_i t + \phi)$ and $\cos(\omega_i t + \phi)$, respectively, and average over one oscillation cycle by integration

$$\int_0^{2\pi/\omega_i} dt \sin^2(\omega_i t + \phi) dt = \int_0^{2\pi/\omega_i} \cos^2(\omega_i t + \phi) = \pi/\omega_i \tag{4.15}$$

$$\int_0^{2\pi/\omega_i} dt \sin(\omega_i t + \phi)\cos(\omega_i t + \phi) = 0, \tag{4.16}$$

and obtain

$$\dot{v}_0 = -\frac{1}{2}[\mathfrak{K}(v) - \mathfrak{G}(v)]v_0 + \frac{eE_i\omega_i}{2\pi m}\eta_s \tag{4.17}$$

$$\dot{\phi} + \omega_i + \omega_0 = \frac{1}{2\omega_i}[\mathfrak{K}(v) - \mathfrak{G}(v)]\frac{\dot{v}_0}{\bar{v}_0} + \frac{eE_i\omega_i}{2\pi m\bar{v}_0}\eta_c \tag{4.18}$$

(compare to Eq. 3.20) where the average velocity $\bar{v}_0$ is related to the basic parameters of the oscillator by $\bar{v}_0 \approx z_0\omega_0$, and

$$\eta_s = \int_0^{2\pi\omega_i} dt \sin(\omega_i t + \phi)\sin(\omega_i t) \approx \frac{\pi}{\omega_i}\cos(\phi) \tag{4.19}$$

$$\eta_c = \int_0^{2\pi\omega_i} dt \cos(\omega_i t + \phi)\sin(\omega_i t) \approx -\frac{\pi}{\omega_i}\sin(\phi). \tag{4.20}$$

The latter approximations hold for $\omega_i \approx \omega_0$. In the steady state, the net gain of the oscillator vanishes [5]

$$[\mathfrak{K}(v) - \mathfrak{G}(v)s_g] \approx 0. \tag{4.21}$$

This is similar to the approximation in chapter 29.2, Eq. 15 of [29]. Accordingly, Eq. 4.18 reads

$$\dot{\phi} + \omega_i - \omega_0 = -\frac{eE_i}{2mz_0\omega_0}\sin(\phi). \tag{4.22}$$

The result is the Adler equation (compare to Eq. 4.2) for a single trapped-ion oscillator with half of the locking range

$$\omega_m = \frac{eE_i}{2mz_0\omega_0} \tag{4.23}$$

which depends on the injected signal amplitude E_i, the oscillation amplitude of the oscillator z_0, its free-running frequency ω_0, and its e/m. Compared to Eq. 4.3, we find the dependence on the quality factor absorbed in the oscillation amplitude which depends on the intensities and the detunings of the damping and the exciting laser. We present an experimental validation of Eq. 4.23 in Sec. 4.1.5.

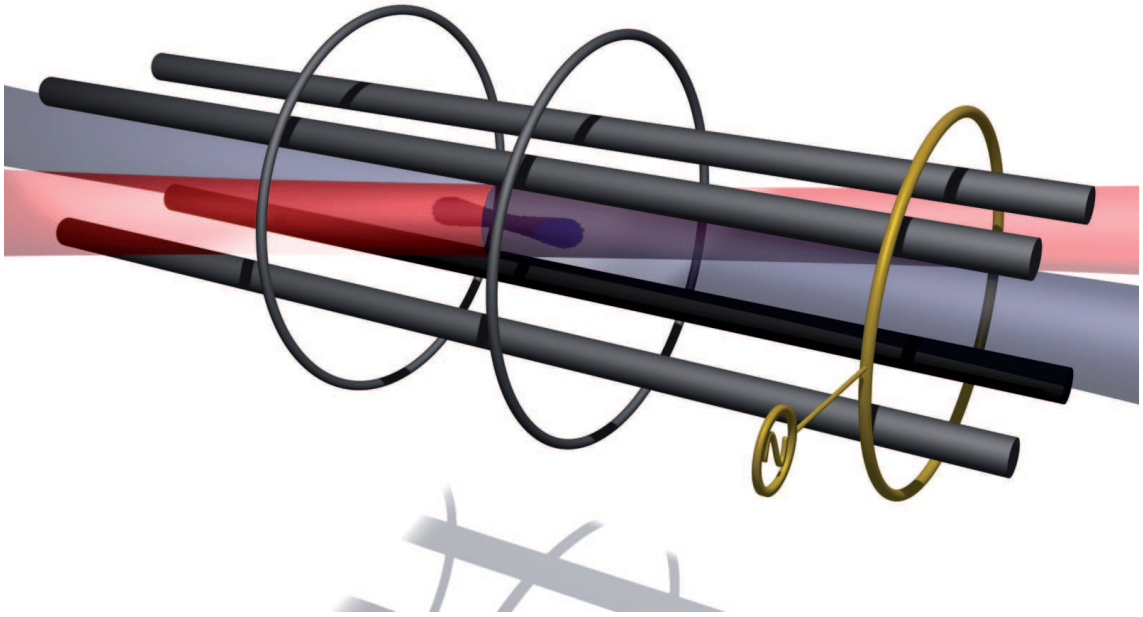

Figure 4.4.: Setup for injection locking. The blue- and red-detuned lasers drive the trapped-ion phonon laser while an external signal is injected via the outer ring electrode.

4.1.3. Experimental procedures

All experiments on injection locking have been conducted in the four-rod ion trap (Sec. 2.1.2, Fig. 4.4). If not noted differently, the trap is operated with a radial oscillation frequency of $\omega_r \approx 2\pi \cdot 1.4$ MHz (Sec. 1.1.1) and an axial frequency $\omega_0 = \omega_z \approx 2\pi \cdot 50$ kHz (Sec. 1.1.2). We work with laser detunings of $\Delta_c = -2\pi \cdot 70$ MHz and $\Delta_g = +2\pi \cdot 10$ MHz with the laser intensities set such that the ion oscillates with an amplitude of ≈ 30 μm with the characteristic double-lobed pattern (Chapter 3, Fig. 3.8). The injected signal is generated by a Stanford Research DS345 synthesizer whose output is connected to the right (from the viewpoint of the camera) outer ring-electrode of the ion trap (Fig. 4.4). We have determined that 1 V applied to this ring generates an electric field of $E_i = 0.37$ mV/m ($F = eE_i = 60(10) \cdot 10^{-24}$ N) on the position of the ion (more details in Sec. 4.2.1).

Note that another method to inject an external signal is modulating the intensity or frequency of one of the laser beams [60]. We have demonstrated this procedure with our setup. With this method, e.g., an exotic mode (which requires spatial field gradients) in an ion chain or crystal could be excited or injection locked with a (focused) laser beam.

4.1.4. Oscillation spectra

With the position sensitive camera readout technique (Sec. 2.3.2), we obtain frequency spectra of the trapped-ion oscillation. Figure 4.5 shows three exemplary spectra obtained for ω_i in and outside the locking range which is marked by the shading. The amplitude of the injected signal was $U_i = 5$ V, each spectrum constitutes an average for ≈ 50 s to improve the signal-to-noise ratio. However, in a single spectrum acquired within less than a second all features are identifiable. In Fig. 4.5 a, taken for ω_i far outside the locking range, the injected signal is visible as an instrumental resolution limited (5 Hz) Lorentzian peak on the left. The free-running component of the oscillator is located approximately in the middle of the shaded locking range and has a width corresponding to a quality factor of ≈ 1400. Comparing Fig. 4.5 a and Fig. 4.5 b, where the injected frequency is set closer to the locking range, reveals three interesting features

- The injected signal has been amplified at the expense of the injected signal in agreement with Eq. 4.1
- Following Eq. 4.6 the frequency of the free-running component has been pulled towards the injected signal
- The linewidth of the free-running component has increased, which implies that the corresponding quality factor has dropped to ≈ 400. This is because the free-running component operates closer to threshold as the injected signal has taken over some of the gain. Similar to the Schawlow-Townes limit of optical lasers the linewidth is proportional to the inverse power [47].

In the last spectrum, Fig. 4.5 (c), the injected frequency is chosen inside the locking range. Here the oscillator is injection locked, and only an instrumental resolution limited component prevails.

Figure 4.6 a shows a detailed analysis of frequency pulling. We recorded additional spectra and extracted the oscillator frequency in each spectrum with a Lorentzian fit excluding the points in the spectra due to the injected signal. In the figure, the free-running frequency is marked by the dotted horizontal line, the locking range by the shaded area. The dotted line is a plot of $\omega = \omega_i$ and the full line represents a fit of Eq. 4.6 to the data points outside the locking range. From the fit we obtain the free-running frequency $\omega_0 = 2\pi \cdot 50\,475(1)$ Hz and half the locking range $\omega_m = 2\pi \cdot 168(3)$ Hz with statistical error bars.

In another measurement we studied the linewidth of the oscillator depending on the oscillation amplitude to confirm the observations of Fig. 4.5 a and b. Here, the injected signal has been turned off and we varied the gain laser intensity (similar to Sec. 3.3). Figure 4.6 b shows the result. The line is a fit of $c_1 + 1/c_2 z_0^2$ where c_1 and c_2 are fit parameters. This $1/z_0^2$ dependence of the linewidth on the oscillation amplitude, is similar to the Schawlow-Townes limit in optical lasers [47].

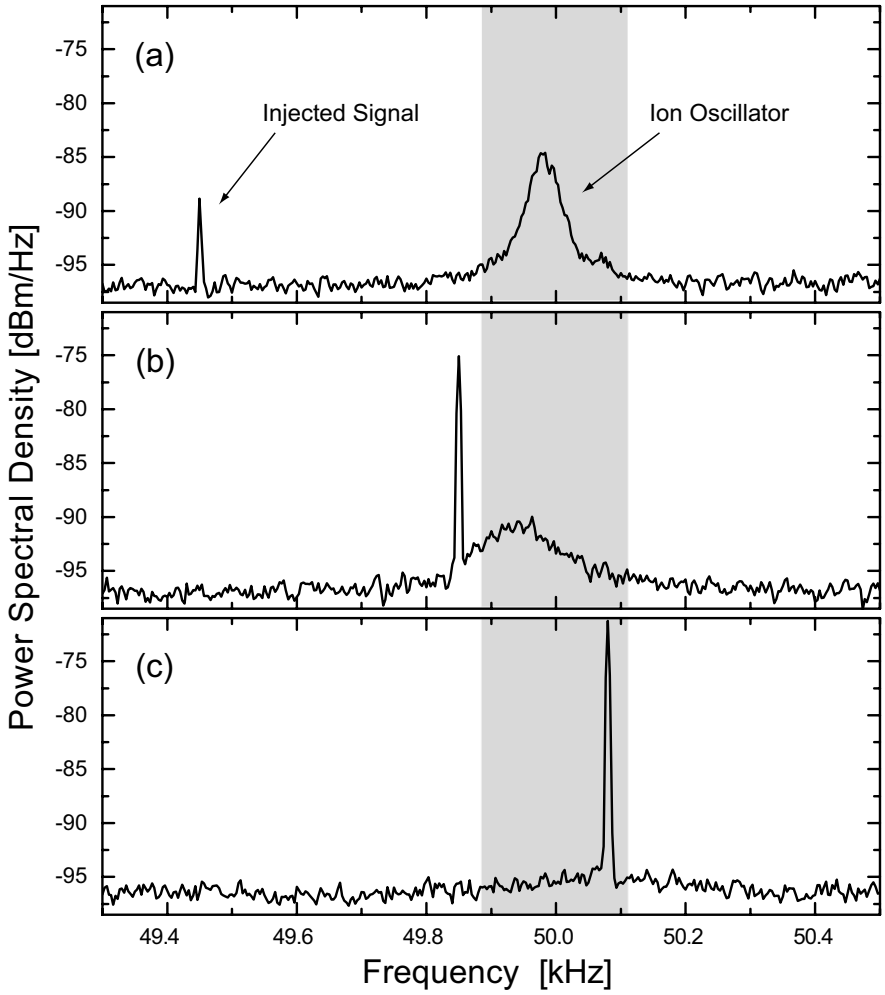

Figure 4.5.: Motional spectra of the trapped-ion phonon laser with an injected signal in and outside the locking range (shaded area). (a) Injected signal outside the locking range. The motional spectrum of the phonon laser is visible in the shaded area, the injected signal as an instrumental resolution limited (5 Hz) peak on the left. In (b), the injected frequency is set closer to the locking range. Three features covered by theory can be observed: The injected signal is amplified at the expense of the free-running oscillator (Eq. 4.1), the frequency of the oscillator is pulled towards the injected signal (Eq. 4.6), and its width has increased. For (c), ω_i was chosen to be inside the locking range. Here only the amplified injected signal prevails.

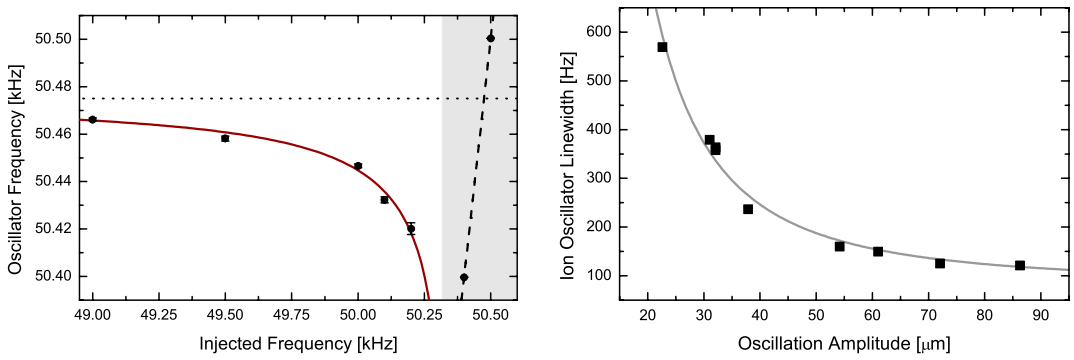

(a) (b)

Figure 4.6.: (a) Detailed analysis of frequency pulling. Measured ion oscillation frequencies $\omega/2\pi$ are plotted versus $\omega_i/2\pi$ with the injection locking range indicated by a shading. The dotted line indicates the free-running frequency $\omega_0/2\pi$ while the dashed line is a plot of $\omega = \omega_i$. Excellent agreement with Eq. 4.6 is found in a fit to the data points outside the locking range (full line). (b) Measurement of the oscillator linewidth depending on the oscillation amplitude. We find the expected $1/z_0^2$ dependence (full line) similar to the Schawlow-Townes limit in optical lasers [47].

The oscillator spectra allow to observe the spectrum of the phonon laser and provide a surprisingly detailed insight into the injection locking dynamics. We have identified frequency pulling, gain competition, and line broadening, which all can be subject to further investigations.

4.1.5. Phase analysis of the ion's motion

A further way to investigate injection locking is to observe the phase of the ion oscillator. This is done by stroboscopic imaging of the ion oscillator (Sec. 2.3.3).

Each data point consists of an injected frequency ω_i and a stroboscopic image. We project the two dimensional ion images onto the oscillation axis and calculate the center of gravity (COG) of the distribution. From the COG within the locking range we derive the relative phase (compare to Eq. 4.4) according to

$$\phi = \arcsin\left(\frac{z}{z_0}\right) \tag{4.24}$$

where z_0 is the root mean square oscillation amplitude and z denotes the COG, both in pixels.

Fig. 4.7 shows a plot of the extracted COG for a measurement consisting of 200 frequency data points taken in random order. Each image has been integrated for 2 s and thus represents an average over $\approx 10^5$ oscillation cycles. The locking range

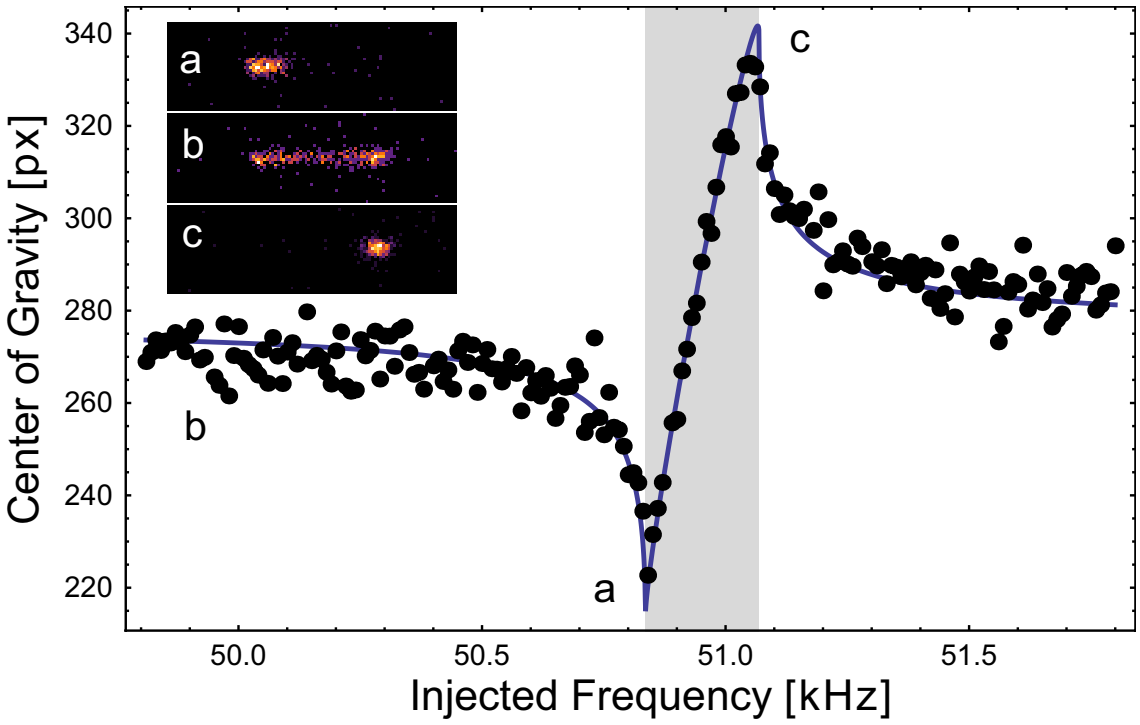

Figure 4.7.: Measurement of the phase between the injection locking signal and the trapped-ion phonon laser using stroboscopic imaging (Sec. 2.3.3). The center of gravity of the ion images is plotted versus the injected frequency, the line is a fit of a time-averaged solution of the Adler equation (Eq. 4.22) to the data. The images outside the locking range (b) show the characteristic double-lobed pattern. Inside the locking range, (a) and (c), the double-lobed pattern collapses to a spot.

is in between the two extrema in the COG and marked by a shading. The insets show exemplary stroboscopic ion images. Outside the locking range, (b), the characteristic double-lobed pattern is observed. Approaching the locking range the double-lobed pattern is increasingly asymmetric due to the phase pull-in behavior of the oscillator. In the context of the spectra presented above (Sec. 4.1.4), we interprete this as that the free-running oscillation diminishes in favor of the injected signal (Fig. 4.5 a/b). Inside the locking range, the double-lobed pattern collapses to a spot, (a) and (c). From the fit of a time-averaged solution of the Adler equation (Eq. 4.22), we extract the free-running frequency $\omega_0 = 2\pi \cdot 50.95$ kHz, the locking range $2\omega_m = 2\pi \cdot 233.3$ Hz, an unintentional phase delay of our electronics of 12°, the oscillation amplitude of 34 μm, and the COG offset of 277 pixels.

Experimental validation of the locking range formula

Using the phase sensitive stroboscopic imaging, we have validated the formula for the locking range (Eq. 4.23)

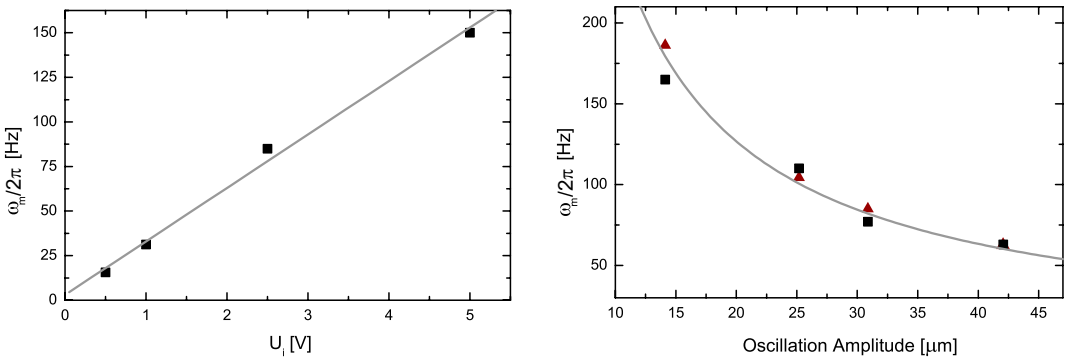

(a) (b)

Figure 4.8.: (a) Confirmation of the linear dependence of ω_m on $U_i \propto E_i$. (b) Absolute determination of the locking range using phase measurements for several oscillation amplitudes calculated with Eq. 4.25 using Sec. 4.2.1 to obtain $E_i = CU_i$ (triangles), and obtained directly from the phase maxima (squares). The line is a $1/z_0$ fit (Eq. 4.25).

$$\omega_m = \frac{eE_i}{2m\omega_0 z_0}. \tag{4.25}$$

Figure 4.8 a shows the extracted locking ranges for $U_i \propto E_i$ ranging from 0.5 V to 5 V confirming the linear dependence. Figure 4.8 b depicts the $1/x$ dependence of the locking range on the oscillation amplitude for $\omega_0 = 2\pi \cdot 38$ kHz. The triangles are an absolute calculation using Eq. 4.25 together with a calibration of the electric field ($E_i = 2.0$ mV/m, Sec. 4.2.1). For the data points represented by the squares, the locking range is directly obtained from the phase maxima of the COG (compare to Fig. 4.7), the line is a $1/x$ fit. Furthermore, we have tested and confirmed the dependence on ω_0. Within the experimental accuracy we find good agreement between experiment and theory.

Conclusions

We have demonstrated injection locking of an almost ultimately small and simple system, a single ion, a single trapped-ion phonon laser. This substantiates the understanding of our trapped-ion phonon laser and provides insight to the phenomena of injection locking. Considering that the forces and fields necessary to injection lock a single ion are very small, we propose the detection of ultra-weak forces and fields using this system.

4.2. Force detection

During the last decades, weak forces have usually been detected with more and more delicate atomic force microscopy (AFM) cantilevers reaching sensitivities in the sub-aN (atto=10^{-18}) range [61]. Measuring forces with a single trapped ion has been considered theoretically in the Wineland/Leuchs group [62]. They propose to use ground state cooled ions and detect external forces by an increased heating rate. Shortly after us [4], the Bollinger group in Boulder has reported a force measurement using Doppler velocimetry in an ensemble of 60 Be^+ ions in a Penning trap with a minimal detected force of 170 yN (yocto=10^{-24}) [63]. Such novel, atomic scale force detectors might be useful for new force detection ideas like the detection of a single nuclear spin as we will discuss in Chapter 5.1.

In this section we present a force measurement down to 5 yN using the injection locking signature in a single trapped ion. We report on the force calibration measurements, discuss the requirements to obtain high sensitivity, and present our results on the minimal detected force.

4.2.1. Force calibration

The ions in the trapping center of our 4-rod trap (Sec. 2.1.2) are well shielded from a field on the injection ring. First estimates to determine the electric field at the location of the ion have been performed using numerical field calculations using a three dimensional model of the trap (Sec. 2.1.2). The strong shielding due to the electrode structure implies a small electric field and thus is numerically challenging. By averaging over the numerical imperfections, we have determined the electric field at the trap center generated by a potential of 1 V on the outer ring electrode to be 0.23 mV/m.

A more precise calibration can be obtained experimentally by measuring the displacement of the trapped ion by a large dc voltage on the injection ring electrode. We consecutively ramp up the voltage on the outer (injection) ring and take an image for each voltage setting. We obtain the ion position from the centroid of a Gaussian fit to the image histogram (Sec. 2.4.2). Figure 4.9 shows as an example a measurement for $\omega_0 = 2\pi \cdot 71$ kHz. From this plot we obtain a linear slope C_s. The force and C_s are related by

$$F = m\omega_0^2 z = m\omega_0^2 C_s B U_{dc}, \tag{4.26}$$

where B is the pixels to μm conversion factor (Sec. 2.3.1). With this we obtain a force of 61.4(1) yN/V with the statistical error of the fit. This implies an electric field of 0.383(1) mV/m for 1 V applied to the outer ring. dc and ac stray fields change the axial and radial confinement. Therefore the forces exerted on the ion differ e.g. for different oscillation frequencies and different micromotion compensation voltages. To take these variations into account, we have taken force calibration

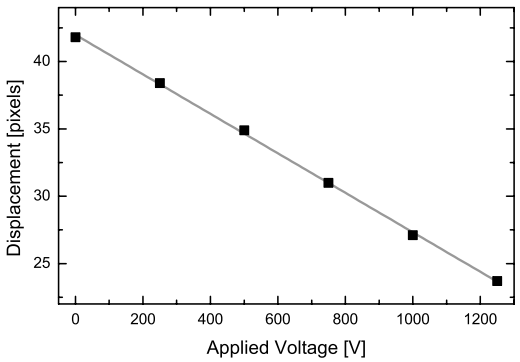

Figure 4.9.: Force calibration. The displacement of the ion by a large dc voltage on the injection ring. With the slope of a linear fit (line) and Eq. 4.26, we obtain a force of 61.4(1) yN/V.

measurements for various parameters. The corresponding general value we deduce is $E_{i,\ 1V} = 0.37(1)$ mV/m, which corresponds to a force on a singly-charged ion of 60(10) yN/V.

4.2.2. Detecting the weakest forces

We found that we could detect the weakest forces using the phase-sensitive stroboscopic imaging method. Ultimately, we expect that the sensitivity will be limited by the trade-off between phase noise due to spontaneous emission, which demands low photon scattering rates and the signal-to-noise ratio of the acquired images, which demands high scattering rates. We additionally experienced technical restrictions due to the stability of the experimental conditions, for example the stability of the free running frequency. Empirically, we found optimum conditions for:

1. Large oscillation amplitude
2. Small laser intensities
3. Fast linear scan speed
4. Large locking range

Loosely speaking the motion comprises of a thermal and an oscillatory contribution. The signal is encoded in the oscillatory part. We thus choose a large oscillation amplitude to minimize the relative contribution of the thermal motion of the ion and the finite resolution of the imaging system ($z_0 > z_{spread}$, compare to Eqs. 3.13, 4.24, and Fig. 4.7). A large oscillation amplitude simply scales the signal-to-noise. Note that according to Eq. 4.25 the locking range scales with $1/z_0$, thus No. 1 conflicts with point No. 4 above. That low laser intensities are beneficial indicates that noise

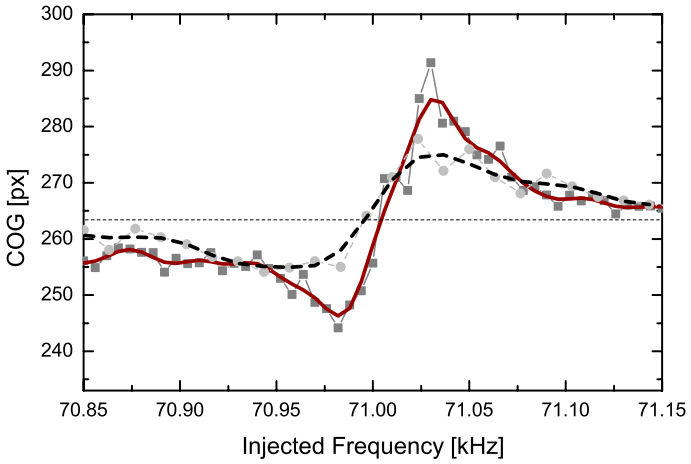

Figure 4.10.: Signal-to-noise (SN) dependence of the injection locking signature on the laser power. Compared to the circles (the thick dashed line is a smoothed average), we chose half the scattering rate but twice the image exposure time for the squares (full lines). The increase in SN in the latter case due to decreased phase noise is evident. The total number of photons/image was ≈ 350.

due to the laser photon scattering recoil is a limiting factor. Apart from the displacement due to scattered photons in the order of μm, which induces phase noise of the oscillator, the temperature and therefore the size of the thermal distribution increases with the laser power (Eq. 1.22). But if the count rate drops below ≈ 100 photons/image, the signal-to-noise begins to decrease since the position of the collapsed ion on the image is not clearly identified any more. Figure 4.10 with $U_i = 1$ V shows a measurement where the oscillation amplitude and all other parameters are held constant except for the laser intensity. The squares (the thick line is a floating average) have half the scattering rate but twice the image exposure time compared to the circles (dashed). The effect on the signal-to-noise is evident. Scanning the frequency fast and linear as well as a large locking range are insensitive to drifts and instabilities of the free-running frequency, which is subject to the following sources of noise:

- Laser intensities
- DC confinement (voltage on the inner rings)
- Axial rf confinement (rf amplitude).

The oscillation amplitude and the damping depend on the laser intensities. While the fluctuations in the damping directly translate into a change in ω_0, the changes in oscillation amplitude only indirectly affect ω_0: Most prominently, the nonuniform spatial distribution of the laser beams induces a change in damping for different

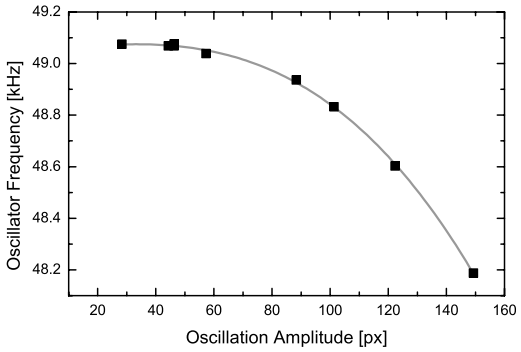

Figure 4.11.: Measured dependence of the free-running frequency on the oscillation amplitude. The line is a polynomial fit.

oscillation amplitudes. Simple intensity stabilization schemes of UV laser beams do not allow to establish a stability better than a few %[1]. From Fig. 3.9, we obtain the noise in the oscillation amplitude due to the intensity fluctuations in the same order. To analyze the change of the free-running frequency, we have tracked ω_0 for several oscillation amplitudes in the data recorded for Fig. 4.6 b. The free-running frequency decreases as the oscillation amplitude increases (Fig. 4.11). The line is a polynomial fit. From this fit, we obtain a change in oscillation frequency of $\approx 10^{-5}$ which is in the order of 1 Hz at 100 kHz.

The specified precision of the power supply used for the axial dc confinement is $< 1 \cdot 10^{-4}$. With this, we obtain a variation in axial frequency in the order of 1 Hz at 70 kHz. The noise contribution originating from the axial rf confinement depends largely on the position of the ion in the trap and has not yet been subject to extensive studies. We estimate this noise to be roughly in the same order of magnitude as the other contributions.

From these considerations we conclude that in the present setup the oscillator free-running frequency is stable to ≈ 1 Hz in 1 s. In order to still resolve the dispersion shaped feature in and outside the locking range we require that the locking range has to be larger than ≈ 1 Hz. To detect ultraweak forces this restricts the other parameters entering Eq. 4.25; we need to have small oscillation amplitude, mass, and free-running frequency. Since the thermal as well as the phase noise contribution increases $\propto 1/m\omega_0$ (Eq. 3.12), we see a tradeoff between visibility of the signal (oscillation amplitude) and these parameters.

To summarize: the limitations we face include the stability of the free-running frequency and phase noise. Optimal parameters in the present setup are moderate laser intensities (≈ 100 Hz image count rate), oscillation amplitude (>20 μm), and free-running frequency (≈ 70 kHz).

[1] private communication N. Kolachewski and unpublished measurements in our lab. Using an integration sphere would most likely improve the stability.

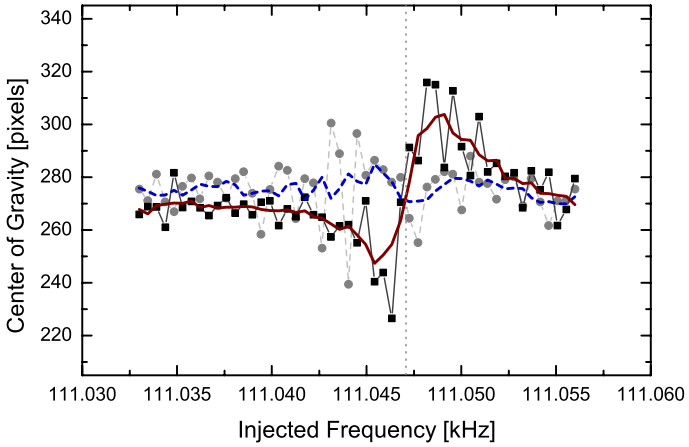

Figure 4.12.: A force measurement with (squares, line) and without the injected signal present (circles, dotted) to demonstrate the signal-to-noise of our minimal force measurement data. The detected force is 6(1) yN at an oscillation frequency of 111 kHz. The vertical line indicates the free-running frequency.

4.2.3. Measurement of ultraweak forces

Adapting to the optimization scheme outlined above, we have taken phase sensitive measurements with very weak injected signals. Figure 4.12 demonstrates the signal-to-noise of such measurements. The image exposure time for each data point is 1 s. The circles and the dotted line are a measurement with the injected signal turned off, the squares and the full line are a measurement with a force of 6(1) yN at $\omega_0 = 2\pi \cdot 111$ kHz ($z_0 \approx 51$ μm, ≈ 120 photons/image, 1 s integration time/image). Thick lines are floating averages to guide the eye. These ultraweak force measurements could only be obtained when ω_i was scanned in one direction since ω_0 drifts by ≈ 1 Hz/min. If we measure the data points in random order, the signal is washed out. The locking range is estimated to be ≈ 2 Hz which is compatible with a locking range obtained with Eq. 4.25. For smaller values of the locking range, the contrast of the dispersion shaped pattern disappears most likely due to fluctuations and drift of the free-running frequency as discussed in Sec. 4.2.2.

Figure 4.13 shows the weakest detected force of 5(1) yN ($z_0 \approx 34$ μm, ≈ 80 photons/image, 1 s integration time/image), which corresponds to an electric field of 31(5) μV/m. A thick line constitutes a floating average to guide the eye. The signal is clearly identifiable and the locking range is ≈ 2 Hz, which is in the order of $10^{-5}\omega_0/2\pi$.

This force is as small as the force due to Earth's gravity on ten ^{24}Mg atoms. While this is orders of magnitude less than the most sensitive AFM [61], it is by far not the weakest force ever detected [64]. However, our measurement is close to the theoretical limits derived for trapped-ion force detection [62, 63], and we improve on a similar measurement [63] by ≈ 30 times. A single trapped ion is a novel atomic

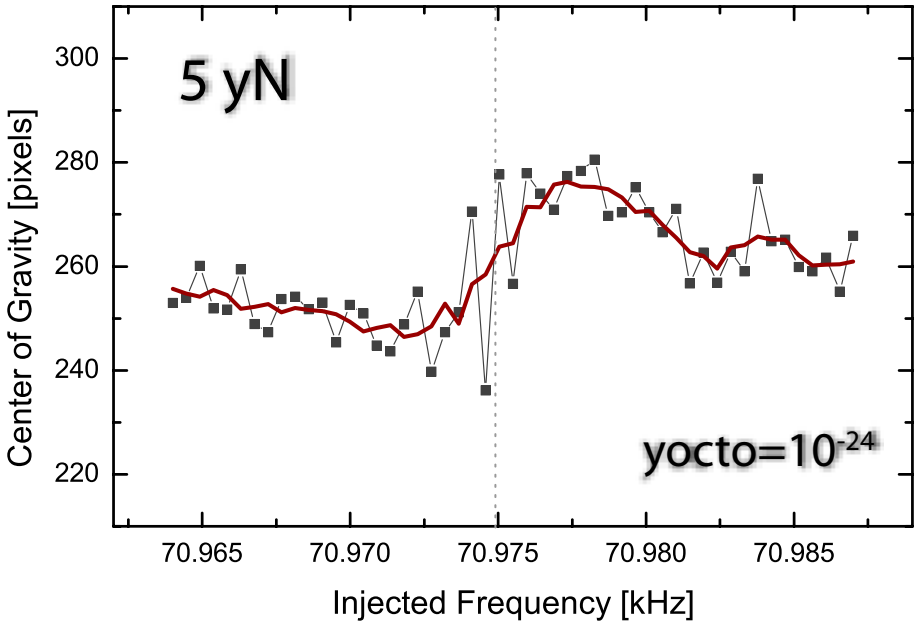

Figure 4.13.: Signal of the weakest detected force of 5(1) yN at 71 kHz. The locking range is ≈ 2 Hz. The vertical line marks the free-running frequency.

scale force/field detector, which might allow the realization of exciting new ideas, as we will discuss in the next chapter.

To give another comparison of the smallness of the force, consider that a force of 6 yN displaces a $^{24}Mg^{+}$ ion in a potential of 111 kHz by only 0.7 nm (Eq. 4.26). This sub nanometer displacement is 3000 times smaller than the thermal distribution of our ion and our imaging resolution (Eq. 3.12), and 80 times smaller than the extent of the ground state wave function of $^{24}Mg^{+}$.

5. Outlook

We have presented a trapped-ion phonon laser and its analogy to an optical laser. Injection locking of this system to an external signal showed its potential to serve as an ultra-sensitive detector for oscillating forces. In this chapter we will present possible applications for trapped-ion force sensors, most prominently our idea to detect a single nuclear spin. Finally, we discuss how the sensitivity of our measurements could be increased.

The surprising sensitivity to external fields and forces is not unchallenged by other detection methods. Note that, e.g., experiments of free-falling electrons reported far higher sensitivities [64]. Besides sensitivity, the more interesting question is the applicability of a system to an interesting problem.

In a theoretical work on force detection [62], the NIST group proposed the measurement of heating rates of different materials to solve the mystery of anomalous heating in miniaturized ion traps [65]. The force measurement in the Bollinger group [63] adds the sensitivity to displacement of these novel trapped-ion ion detectors. Our idea is the detection of nuclear spin flips of a single charged particle.

5.1. Detection of nuclear spin flips of a single charged particle

Magnetic force microscopy (MFM) cantilevers and similar devices which are usually employed for the measurement of small numbers of spins are to our knowledge limited to ≈ 1200 nuclear spins or a single electron spin [66, 67, 68]. We propose to detect a single nuclear spin unperturbed by any solvent or a crystal structure in a solid by the force in an inhomogeneous magnetic field. The nuclear spin could be detected in highly charged ions or molecules where the electronic structure is not directly accessible with present laser technology. The particle could be any charged particle to which a laser coolant partner for simultaneous trapping is available. This can be highly charged ions as well as molecules and highly charged larger particles [69].

Figure 5.1 illustrates the basic idea. The target ion is co-stored and oscillating with a manipulation/readout ion. We suggest to use a surface electrode trap for easier introduction of external elements. A force is exerted on the ion due to its nuclear magnetic spin in an inhomogeneous magnetic field generated, e.g., by a tiny current loop. The force depends on the nuclear spin of the ion. If a microwave field changes the spin with a Rabi-frequency close to the free-running frequency of the

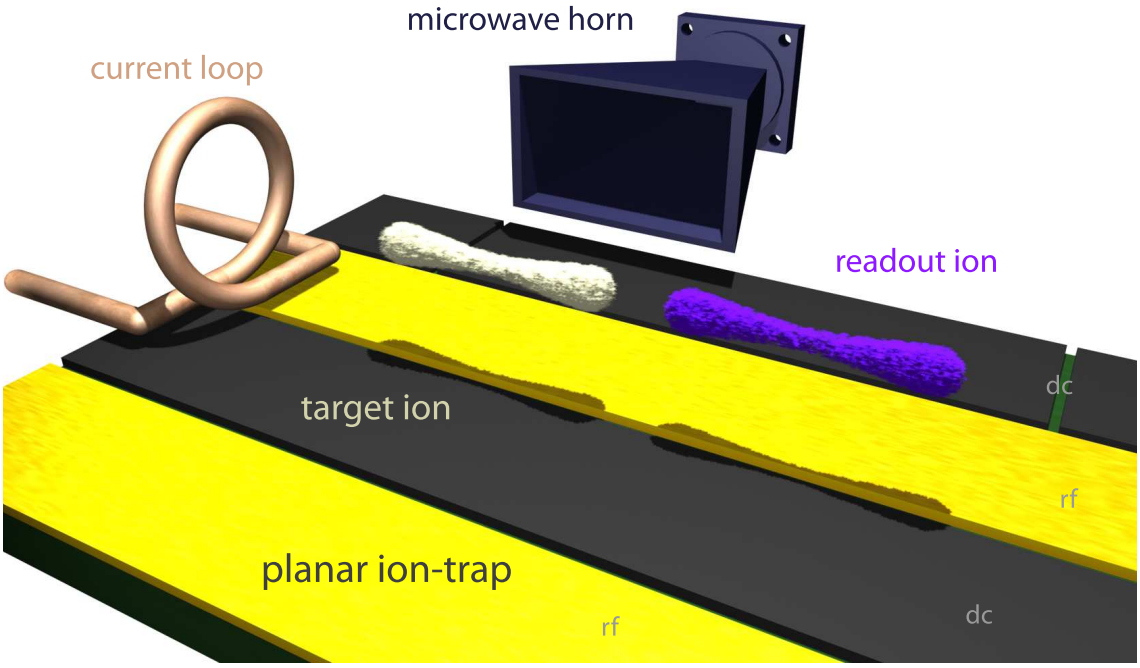

Figure 5.1.: Schematic of a conceivable setup for the detection of nuclear spin flips using injection locking. A force on the co-stored target ion is exerted in the inhomogeneous magnetic field of a tiny current loop. A microwave horn drives nuclear spin flips at a Rabi frequency close to the free-running frequency of the ions and injection-locks their motion which can be detected in the phase of the ion oscillation.

ion pair's center-of-mass mode, the corresponding oscillating force injection locks the motion which is detected in the phase of the oscillator.

The force on a nuclear spin in an inhomogeneous magnetic field in z-direction (the ion's oscillation direction) reads

$$F = \mu \frac{dB}{dz} \tag{5.1}$$

with the magnetic field gradient dB/dz and the magnetic moment

$$\mu = \mu_n g m_i \tag{5.2}$$

where g denotes the g-factor, m_i the nuclear spin, and μ_n the nuclear magneton. In nuclear physics usually the value gm_i is measured. Typical values are in the order of 1 to 10 [70, 71]. The nuclear magneton reads $\mu_n = 5.051 \cdot 10^{-27}$ J/T. Note that μ_n is 1836 times smaller than the Bohr magneton μ_B.

Inhomogeneous magnetic fields can be generated in several ways. The most simple

realization is a straight wire close to the ion and at right angle with respect to the oscillation direction z. According to Biot-Savart, we obtain

$$B = \frac{\mu_0}{2\pi}\frac{I}{z} \tag{5.3}$$

where I denotes the current, z the distance from the wire, and μ_0 is the vacuum permeability. The gradient of the magnetic field in radial direction reads

$$\frac{dB}{dz} = -\frac{\mu_0}{2\pi}\frac{I}{z^2}. \tag{5.4}$$

With a current of 10 A through the wire at a distance 100 μm from the ion we obtain a magnetic field gradient of 200 T/m.

More intricate would be the implementation of a tiny current loop close to the ion where the magnetic field in z-direction vertical to the loop plane reads

$$B = \frac{\mu_0}{2} I \frac{r^2}{(r^2+z^2)^{3/2}} \tag{5.5}$$

with r denoting the radius of the loop. The gradient in the axial, z-direction is

$$\frac{dB}{dz} = -\frac{3\mu_0}{4} I \frac{zr^2}{(r^2+z^2)^{5/2}} \tag{5.6}$$

and has a maximum at $z \approx 0.0002\ r$ where it reaches $2I/\mathrm{A}$ T/m. Therefore in this example, one could obtain ≈ 40 T/m.

Also conceivable is the use of a tiny permanent magnet. For distances $\gtrapprox 5$ times larger than the largest dimension of the magnet it can be approximated as a dipole. Then the magnetic field is

$$B = \frac{\mu_0 M}{2\pi z^3} \tag{5.7}$$

and its gradient

$$\frac{dB}{dz} = -\frac{3}{2\pi}\frac{\mu_0 M}{z^4} \tag{5.8}$$

where M reads

$$M = B_r V/\mu_0. \tag{5.9}$$

The magnetization B_r of permanent magnets can be as large as 1.4 T[1] and V is the volume of the permanent magnet. For a circular magnet with a radius of 10 μm and a length of 100 μm, we calculate a gradient of 200 T/m in a distance of 100 μm from the tip.

[1] http://www.supermagnete.de/data_table.php

Plugging these values into Eq. 5.1 we obtain

$$F \approx 10 \times 5.051 \cdot 10^{-27} J/N \times 200\ T/m \approx 10 \cdot 10^{-24} N \tag{5.10}$$

which is 10 yN. With the forces we have detected in our present setup, 5 yN (Sec. 4.2.3), and the limits on the order of $\approx 1 \cdot 10^{-24}$ given in [62, 63] this seems feasible. However, the details of an actual experiment, how to generate such magnetic field gradients, as well as which ion candidates are interesting still have to be investigated.

A promising start to a realization of this experiment could be the simulation of nuclear spin flips with their electronic counterparts. Here the forces will be $\mu_B/\mu_n = 1836$ times larger, hence more easily detectable. The detection scheme and the setup as well as the limitations could be explored.

5.2. Conclusions

We have presented a trapped-ion phonon laser for the first time. This system shows conclusive parallels to an optical laser such as a threshold to coherent oscillation sustained by coherent generation of phonons, gain saturation, line narrowing, and injection locking. Further studies of our particular phonon laser could be performed by observing these phenomena in more complex systems like ion chains and crystals. Besides that, one could find out about possible phonon outcoupling mechanisms.

Furthermore, we have demonstrated injection locking of this trapped-ion phonon laser to an external signal. With our techniques to obtain oscillator spectra and phase information of the oscillator we were able to study this system to a high level of detail in and outside the locking range. We observe amplification of the injected signal by the oscillator, gain competition between the oscillator and the injected signal, line broadening, the arcsin phase dependence inside the locking range, and frequency and phase pulling all in excellent agreement with theory.

Since the slope of the dispersion-shaped phase signature inside the locking range (Figs. 4.7 and 4.13) is very steep, a slight change in mass will change the free-running frequency which we observe in a change in phase. Therefore we suggest that this system might find applications in mass spectrometry [60]. Masaki Hori from CERN proposed a very exciting idea: the detection of γ decays in a real time mass change. Mass spectrometry employing injection locking of a trapped-ion phonon laser is discussed in detail in Appendix B.

From a calibration of the fields and forces which induce injection locking, we demonstrate that we detect forces as weak as 5(1) yN. With this sensitivity, the detection of nuclear spin flips of a single trapped ion appears feasible.

However, several improvements in the setup must be implemented to increase the sensitivity. Most important is the modification of the phase detection scheme. Here, the arrival time of each photon can be measured instead of selecting a phase

window. From this phase information, the image can be recalculated to obtain the phase. In the present phase window scheme we use only $\approx 5\%$ of all detected photons (Sec. 2.3.3). Thus, we expect major improvements in signal to noise if we use 100% instead. Furthermore, the locking range could be increased to be independent of fluctuations in the oscillator free-running frequency by a factor of 2.5 using Be^+ instead of Mg^+ ions. Also, the stability of the oscillator free-running frequency could be improved by stabilizing the dc voltage sources, the rf voltage in the trap, and the laser intensities, the latter e.g. by using integrating spheres.

With these upgrades we expect a considerable increase in sensitivity which would further strengthen the applications we propose for this system as there are mass spectrometry (Appendix B) and force detection e.g. of nuclear spin flips of a single trapped particle.

A. Fundamental constants and Magnesium data

All data taken from the NIST database[1].

Fundamental constants:

Quantity	Symbol	Value	Unit
speed of light in vacuum	c	299 792 458	m s^{-1}
magnetic constant	μ_0	$4\pi \times 10^{-7}$	N A^{-2}
Planck constant	h	$6.626\ 068\ 96(33) \times 10^{-34}$	m^3 kg^{-1} s^{-2}
Boltzmann's constant	k_b	$1.380\ 650\ 3(24) \times 10^{-23}$	J K^{-1}
atomic mass unit	u	$1.660\ 538\ 78(8) \times 10^{-23}$	kg
Bohr magneton	μ_B	$9.274\ 009\ 15(23) \times 10^{-24}$	J T^{-1}
nuclear magneton	μ_n	$5.050\ 783\ 24(13) \times 10^{-27}$	J T^{-1}

Physical properties of the ^{24}Mg atom:

Quantity	Symbol	Value	Unit
atomic number	Z	12	
total nucleons	Z+N	24	
relative abundance		78.99	%
atomic mass	m	$3.985\ 293\ 072 \times 10^{-27}$	kg
melting point	T_m	923	K

The $3^2s_{1/2} \longrightarrow 3^2p_{3/2}$ transition of the $^{24}Mg^+$ ion atom:

Quantity	Symbol	Value	Unit
transition frequency	$\nu_{transition}$	1 072 082 934.33(16) [2]	MHz
vacuum wavelength	λ	279.6355099	nm
natural linewidth	Γ	41.8(4) [72]	MHz
saturation intensity	I_s	2480	W m^{-2}

[1] http://physics.nist.gov/cuu/index.html

B. Mass spectrometry with a trapped-ion phonon laser

A change of the free-running frequency of an injection locked oscillator is observable in a change of its phase with respect to the injected signal which translates into a shift of the center of gravity in the stroboscopic imaging. This way we should be able to detect tiny changes in the mass of an ion or perform precise mass measurements, similar to [60]. From the estimations in Sec. 4.2.2, we are currently limited to a change or stability of $\delta f/f \approx 2 \cdot 10^{-5}$ corresponding to a mass sensitivity of $\delta m/m \approx 4 \cdot 10^{-5}$ (two ions).

The best reported mass resolution in an ion trap is $1.4 \cdot 10^{-4}$ [60] on which we could, in principle, improve. Our sensitivity would be sufficient to measure the relative mass difference of the mass doublet $^{40}Ca^{18}O^+$ and $^{42}Ca^{16}O^+$, which is expected to be $1.4 \cdot 10^{-4}$ [73].

A different, even more interesting application for mass spectrometry would be the detection of γ decay events from a metastable nuclear state by the mass change of the nucleus. A possible experiment could be conducted as follows: A radioactive charged ion species with a relatively short lifetime in the order of less than a day is loaded together with a manipulation/drive/readout ion. Note that in the case of two simultaneously trapped ions the axial oscillation frequency changes according to [60]

$$f_+ = \sqrt{(1+\mu) + \sqrt{1-\mu+\mu^2}}\, f_0 \tag{B.1}$$

where $\mu = m_1/m_2$, m_1 and m_2 are the masses of the respective ions. The ions are laser-driven to oscillate with the drive ion, the injected signal is set to the edge of the expected locking range for the doubly charged radioactive ion (in the case e.g. of a β^- decay). After the β^- decay into the metastable state, the ion charge increases by one, it injection locks and we observe a change in phase in the stroboscopic images. As the following γ decay takes place, we again see a change in ω_0, thus in the phase.

Unfortunately only very few atomic species have metastable states with suitable properties. A problem is the recoil from the first decay, α, β^-, or β^+ (electron capture), which depends on the exact decay chain. Furthermore, the metastable state has to be populated to a reasonable amount (by the decay of a suitable parent ion), and have a lifetime longer than our detection speed (in the order of one second). Finally the mass change due to the γ emission should be large enough to be detected.

MS ion	$\tau_{1/2,GS}$	E_γ keV	$\tau_{1/2,MS}$	$\delta f/f$ $\times 10^{-6}$	E_{kin} eV	Par. ion	dec.	$E_{dec.}$ MeV	$\tau_{1/2,P}$	% MS
^{38}Cl	32.2m	671	0.7s	8.6	6	^{38}S	β^-	2.93	170m	<0.3
^{52}Mn	5.6d	378	21m	3.3	1.4	^{52}Fe	EC, β^+	3	8.28h	100
^{87}Y	79.8h	381	13.4d	1.7	0.9	^{87}Zr	EC	3.7	1.68h	100
^{89}Y	stable	909	16s	3.8	4.96	^{89}Zr	EC	2.8	78h	99
^{90}Zr	stable	2319	0.8s	9.7	31.5	^{90}Nb	EC	6.1	14.6h	100
^{91}Y	58.5d	556	49.7m	2.3	2.1	^{91}Sr	β^-	2.71	9.6h	56
^{97}Nb	72.1m	743	52.7s	2.7	3	^{97}Zr	β^-	2.66	16.9h	93
^{136}Ba	stable	2000	0.3s	3.9	15	^{136}Cs	β^-	2.5	13d	11

Table B.1.: Possible candidates for a γ-decay detection experiments. The frequency change $\delta f/f$ is calculated for $^{136}Ba^+$ as trapping partner. Problematic values are highlighted in red, good values in cyan. GS: ground state, MS: metastable state, Par/P: parent, dec: decay.

From [74] we obtain several candidates for metastable transitions (Tab. B.1): ^{38}Cl and ^{136}Ba have some problems with the branching ratio to the metastable state. For ^{90}Zr, the kinetic energy from the γ recoil might be a little bit too large (this decreases the probability to keep the ion trapped after the first decay) and for all candidates, the frequency change will be in the order of several times 10^{-6}, about one order of magnitude below the present sensitivity. Most promising is the signal of ^{38}Cl and ^{90}Zr which if simultaneously trapped with $^{138}Ba^+$ ions (eq. B.1) will be subject to a frequency change of $\approx 1 \cdot 10^{-5}$ which is on the edge of being detectable with our present setup.

To conclude, this is a promising and interesting experiment but requires more work on the sensitivity limits and stabilization of the free-running frequency. A further challenge of such an experiment would be the implementation of radioactive ion species loading.

C. Electronics and software

Here we present some of the electronics used in this work.

C.1. Position discriminator

The position discriminator (Fig. C.1) consists of four comparator units (=, Texas Instruments TLC274 quadrupole differential comparator) which compare the camera position signals U_x and U_y to four voltages which define a region for photon acceptance. With several AND conjunctions (&, Texas Instruments SN74HC00 quadrupole 2-input positive-NAND gates), we combine the logic signals. Finally, the camera trigger signal is conjuncted with the outcome and the accepted trigger signals are sent to a spectrum analyzer.

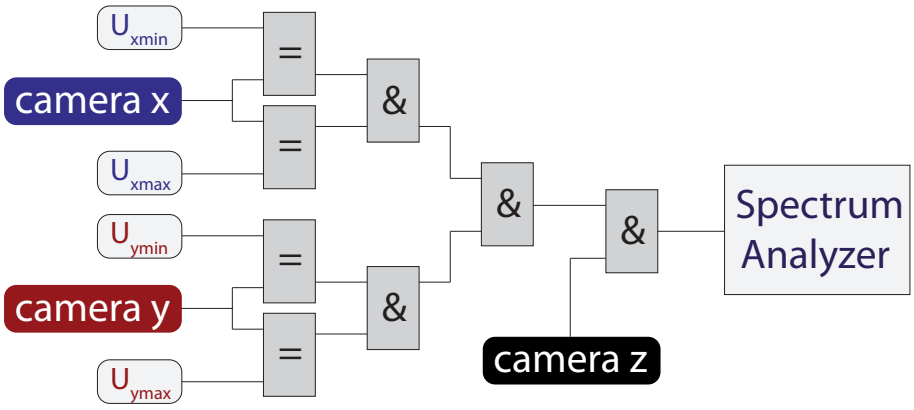

Figure C.1.: Position discriminator.

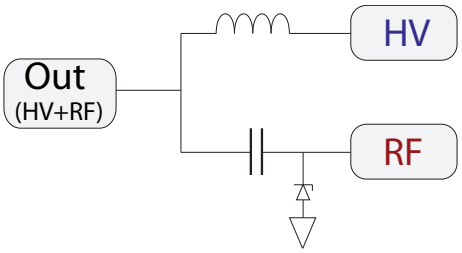

Figure C.2.: DC + RF adding circuit.

C.2. Bias-tee

This circuit (Fig. C.2) adds a rf signal to a dc voltage. A coil shields the HV power supply from the rf, while a capacitor and a Zehner diode protect the rf power supply from the HV. With $L = 1$ μH and $C = 1$ μF (capable of bearing 1 kV) the addition of a rf signal with a frequency > 5 kHz and an amplitude of < 20 Vpp to a 1 kV dc voltage is possible with this circuit.

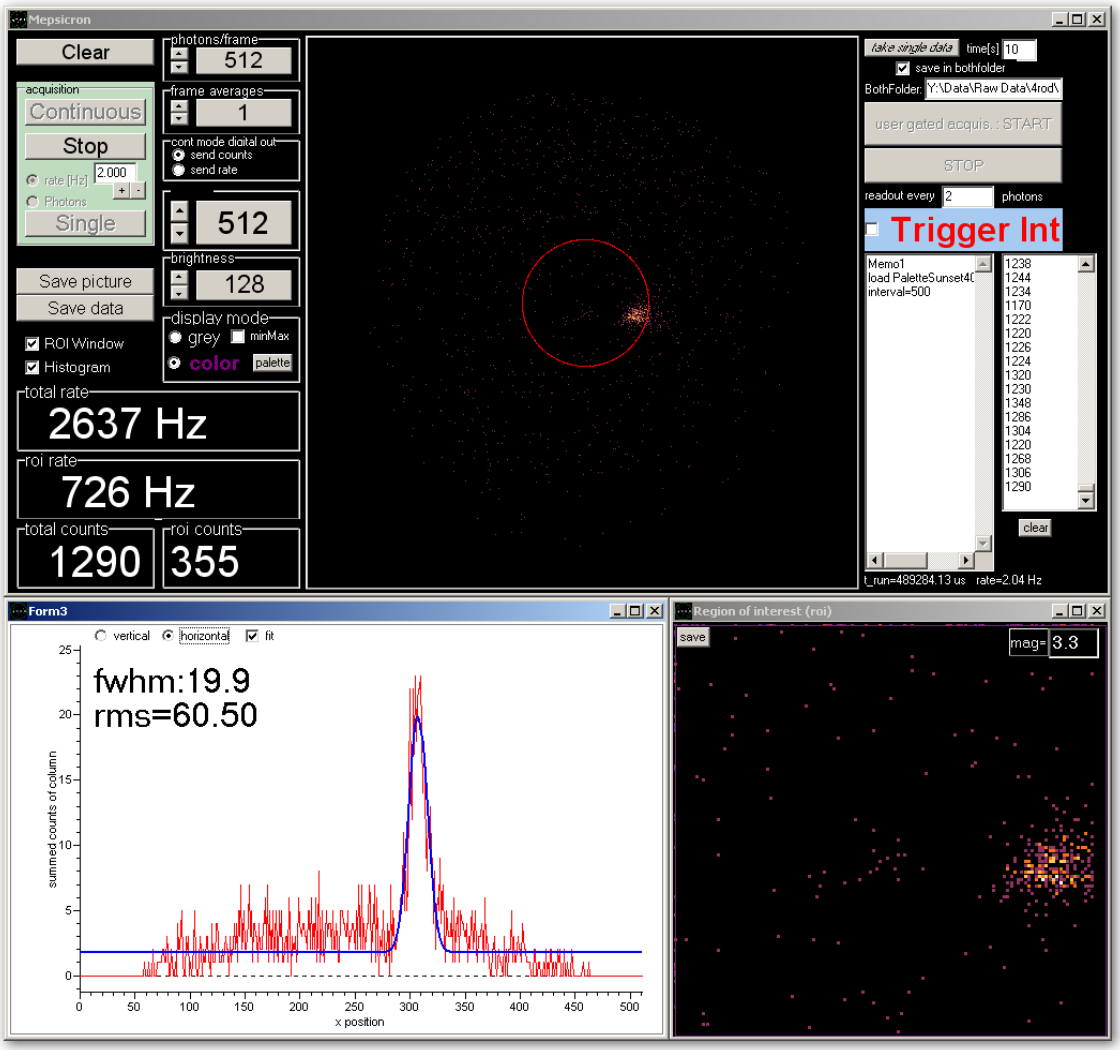

Figure C.3.: Mepsicron camera readout software.

C.3. Camera readout software

The software we developed for camera readout (Fig. C.3) controls a Meilhaus Mepsicron ME4600 multi IO card which acquires the camera data. The frontend is organized as follows. On the left, the real-time features can be started and modified. Two checkboxes toggle the histogram and region of interest zoom windows. The image resolution and color or gray scale palettes can be chosen. The big checkbox on the right allows to prepare the software to be operated in the slaved mode controlled by the "Mg+ 2" software (Sec. C.4) over the bus system (sec. 2.4.1). However, it will continue its current state (e.g. video mode) until it is remotely slaved and return if the slaved mode ends. The status of the system and supplementary information are shown on the panels on the right side.

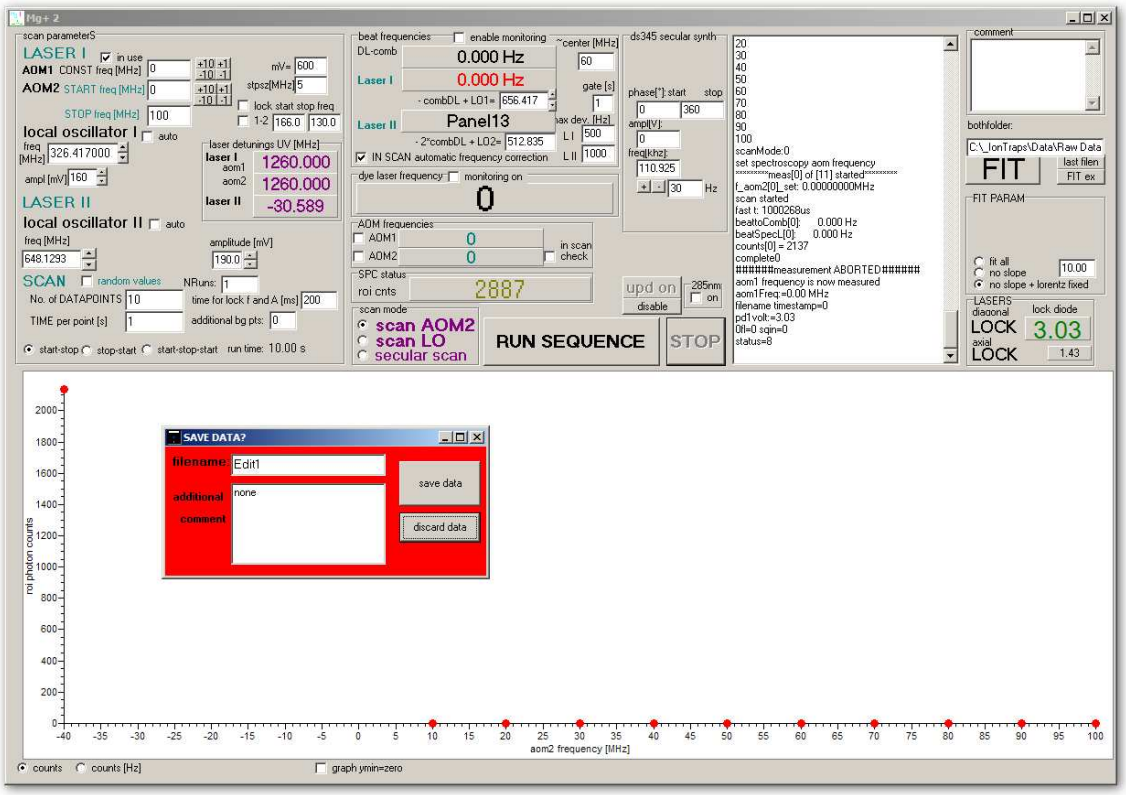

Figure C.4.: "Mg+ 2" experiment control software.

C.4. Measurement software

To perform measurements and control the system, we developed the "Mg+ 2" software. The frontend (Fig. C.4) is organized as follows: basic scan and the laser

parameters are set and displayed on the left panel. On the central panel the status of the frequency locks and the count rate from the Mepsicron software are displayed. During the scans, data and status information are displayed in the larger panel on the right.

Bibliography

[1] V. Batteiger, S. Knünz, M. Herrmann, G. Saathoff, H. A. Schüssler, B. Bernhardt, T. Wilken, R. Holzwarth, T. W. Hänsch, and Th. Udem, "Precision spectroscopy of the 3s-3p fine-structure doublet in Mg^+," *Phys Rev. A*, vol. 80, no. 2, p. 022503, 2009.

[2] M. Herrmann, V. Batteiger, S. Knünz, G. Saathoff, Th. Udem, and T. W. Hänsch, "Frequency metrology on single trapped ions in the weak binding limit: The $3s_{1/2}$-$3p_{3/2}$ transition in $^{24}Mg^+$," *Phys. Rev. Lett.*, vol. 102, no. 1, p. 013006, 2009.

[3] V. Batteiger, *Title t.b.a.* PhD thesis, Ludwig-Maximilians-Universität, Munich, Germany, 2011.

[4] S. Knünz, M. Herrmann, V. Batteiger, G. Saathoff, T.W. Hänsch, K. Vahala, and Th. Udem, "Injection locking of a trapped-ion phonon laser," *Phys. Rev. Lett.*, vol. 105, no. 1, p. 013004, 2010.

[5] K. Vahala, M. Herrmann, S. Knünz, V. Batteiger, G. Saathoff, T.W. Hänsch, and Th. Udem, "A phonon laser," *Nat. Phys.*, vol. 5, p. 682, 2009.

[6] M. Herrmann, M. Haas, U.D. Jentschura, F. Kottmann, D. Leibfried, G. Saathoff, C. Gohle, A. Ozawa, V. Batteiger, S. Knünz, N. Kolachevsky, H.A. Schüssler, T.W. Hänsch, and Th. Udem, "Feasibility of coherent xuv spectroscopy on the 1s-2s transition in singly ionized helium," *Phys. Rev. A*, vol. 79, no. 5, p. 052505, 2009.

[7] W. Paul, O. Osberghaus, and E. Fischer, "Ein Ionenkäfig," *Forschungsberichte des Wirtschafts- und Verkehrsministeriums von Nordrhein-Westfalen*, pp. 1–42, 1958.

[8] Norman F. Ramsey, Hans G. Dehmelt, and Wolfgang Paul, "Nobel Lecture, 'for the development of the ion trap technique'." http://www.nobelprize.org/.

[9] T. W. Hänsch and A. L. Schawlow, "Cooling of gases by laser radiation," *Opt. Commun.*, vol. 13, pp. 68–69, 1975.

[10] D. J. Wineland and D. H. Dehmelt, "Proposed 10^{-14} $\Delta\nu/\nu$ laser fluorescence spectroscopy on Ti^+ mono-ion oscillator III," *Bull. Am. Phys. Soc.*, vol. 20, p. 637, 1975.

[11] W. Neuhauser, M. Hohenstatt, P. Toschek, and H. Dehmelt, "Optical-sideband cooling of visible atom cloud confined in parabolic well," *Phys. Rev. Lett.*, vol. 41, pp. 233–236, 1978.

[12] D. Wineland, R. E. Drullinger, and F. L. Walls, "Radiation-pressure cooling of bound resonant absorbers," *Phys. Rev. Lett.*, vol. 40, pp. 1639–1642, 1978.

[13] M. Kasevich and S. Chu, "Laser cooling below a photon recoil with three-level atoms," *Phys. Rev. Lett.*, vol. 69, p. 1741, 1992.

[14] D. Kielpinski, C. Monroe, and D. J. Wineland, "Architecture for a large-scale ion-trap quantum computer," *Nature*, vol. 417, pp. 709–711, 2002.

[15] A. Friedenauer, H. Schmitz, J. T. Glueckert, D. Porras, and T. Schaetz, "Simulating a quantum magnet with trapped ions," *Nat. Phys.*, vol. 4, pp. 757–761, 2008.

[16] C. W. Chou, D. B. Hume, J. C. J. Koelemeij, D. J. Wineland, and T. Rosenband, "Frequency comparison of two high-accuracy Al^+ optical clocks," *Phys. Rev. Lett.*, vol. 104, p. 070802, 2010.

[17] D. Leibfried, R. Blatt, C. Monroe, and D. Wineland, "Quantum dynamics of single trapped ions," *Rev. Mod. Phys.*, vol. 75, p. 281, 2003.

[18] F. G. Major, V. N. Gheorghe, and G. Werth, *Charged Particle Traps*. Berlin: Springer, springer series on atomic, optical, and plasma physics ed., 2005.

[19] D. R. Denison, "Operating parameters of a quadrupole in a grounded cylindrical housing," *J. Vac. Sci. Tech.*, vol. 8, no. 1, pp. 266–269, 1971.

[20] S. Knünz, "Magnesium ions in radio frequency trap," Diploma's thesis, Ludwig-Maximilians-Universität, Munich, Germany, 2007.

[21] M. J. Madsen, W. K. Hensinger, D. Stick, J. A. Rabchuk, and C. Monroe, "Planar ion trap geometry for microfabrication," *Appl. Phys. B*, vol. 78, pp. 639–651, 2004.

[22] S. Stenholm, "The semiclassical theory of laser cooling," *Rev. Mod. Phys.*, vol. 58, no. 3, p. 699, 1986.

[23] D. J. Wineland and W. M. Itano, "Laser cooling of atoms," *Phys. Rev. A*, vol. 20, no. 4, p. 1521, 1979.

[24] M. Herrmann, *Precision spectroscopy and optomechanics of single trapped ions in the weak-binding limit*. PhD thesis, Ludwig-Maximilians-Universität, Munich, Germany, 2008.

[25] D. J. Berkeland, J. D. Miller, J. C. Bergquist, W. M. Itano, and D. J. Wineland, "Minimization of ion micromotion in a paul trap," *J. of Appl. Phys.*, vol. 83, no. 10, p. 5025, 1998.

[26] A. Friedenauer, F. Markert, H. Schmitz, L. Petersen, S. Kahra, M. Herrmann, Th. Udem, T. W. Hänsch, and T. Schätz, "High power all solid state laser system near 280 nm," *Appl. Phys. B*, vol. 84, no. 3, pp. 371–373, 2006.

[27] C. Estienne, "A pulsed dye laser for photo-ionization of magnesium atoms," Master's thesis, Swiss Federal Institute of Technology, Zürich, Switzerland, 2009.

[28] B. Bernhardt, T. W. Hänsch, and R. Holzwarth, "Implementation and characterization of a stable optical frequency distribution system," *Opt. Expr.*, vol. 17, no. 19, pp. 16849–16860, 2009.

[29] A. E. Siegman, *Lasers*. Sausalito, CA: University Science Books, 1986.

[30] J. Alnis, A. Matveev, N. Kolachevsky, Th. Udem, and T. W. Hänsch, "Subhertz linewidth diode lasers by stabilization to vibrationally and thermally compensated ultralow-expansion glass Fabry-Pérot cavities," *Phys. Rev. A*, vol. 77, no. 5, p. 053809, 2008.

[31] R. W. P. Drever, J. L. Hall, F. V. Kowalski, J. Hough, G. M. Ford, A. J. Munley, and H. Ward, "Laser phase and frequency stabilization using an optical resonator," *Appl. Phys. B*, vol. 31, no. 2, pp. 97–105, 1983.

[32] A. Sharma and J. G. Walker, "Paralyzable and nonparalyzable deadtime analysis in spatial photon counting," *Rev. Sci. Instrum.*, vol. 63, no. 12, p. 5784, 1992.

[33] D. F. V. James, "Quantum dynamics of cold trapped ions with application to quantum computation," *Appl. Phys. B*, vol. 66, pp. 181–190, 1998.

[34] W. H. Press, B. P. Flannery, S. A. Teukolsky, and W. T. Vetterling, *Numerical Recipes in Pascal*. New York: Cambridge Univ. Press, 2 ed., 1989.

[35] S. Wallentowitz, W. Vogel, I. Siemers, and P. E. Toschek, "Vibrational amplification by stimulated emission of radiation," *Phys. Rev. A*, vol. 54, pp. 943–946, 1996.

[36] H. C. Liu, C. Y. Song, Z. R. Wasilewski, and A. J. SpringThorpe, C. Dharmawardana, G. C. Aers, D. J. Lockwood, and J. A. Gupta, "Coupled electron-phonon modes in optically pumped resonant intersubband lasers," *Phys. Rev. Lett.*, vol. 90, p. 077402, 2003.

[37] I. Bargatin and M. L. Roukes, "Nanomechanical analog of a laser: Amplification of mechanical oscillations by stimulated zeeman transitions," *Phys. Rev. Lett.*, vol. 91, p. 138302, 2003.

[38] E. M. Chudnovsky and D. A. Garanin, "Phonon superradiance and phonon laser effect in nanomagnets," *Phys. Rev. Lett.*, vol. 93, no. 25, p. 257205, 2004.

[39] J. Chen and J. B. Khurgin, "Feasibility analysis of phonon lasers," *IEEE J. Quant. Ele.*, vol. 39, pp. 600–607, 2003.

[40] A. J. Kent, R. N. Kini, N. M. Stanton, M. Henini, B. A. Glavin, V. A. Kochelap, and T. L. Linnik, "Acoustic phonon emission from a weakly coupled superlattice under vertical electron transport: Observation of phonon resonance," *Phys. Rev. Lett.*, vol. 96, p. 215504, 2006.

[41] W. Ketterle and S. Inouye, "Collective enhancement and suppression in Bose–Einstein condensates," *C. R. Acad. Sci. Paris*, vol. 2, no. 4, pp. 339–380, 2001.

[42] M. Sargent, M. O. Scully, and W. E. Lamb, *Laser Physics*. Reading, Mass.: Addison-Wesley, 1974.

[43] B. Van der Pol, "A theory of the amplitude of free and forced triode vibrations," *Radio Rev.*, vol. 1, pp. 701–710, 1920.

[44] G. E. Uhlenbeck and L. S. Ornstein, "On the theory of the Brownian motion," *Phys. Rev.*, vol. 36, p. 823, 1930.

[45] W. Nagourney, G. Janik, and H. Dehmelt, "Linewidth of single laser-cooled $^{24}Mg^{+}$ ion in radiofrequency trap," *Proc. Natl. Acad. Sci. USA*, vol. 80, pp. 643–646, 1983.

[46] W. Neuhauser, M. Hohenstatt, H. Dehmelt, and P. E. Toschek, "Localized visible Ba^{+} mono-ion oscillator," *Phys. Rev. A*, vol. 22, no. 3, p. 1137, 1980.

[47] A. Yariv, *Quantum Electronics*. Sausalito, CA: Wiley, 1989.

[48] S. M. Spillane, T. J. Kippenberg, and K. J. Vahala, "Ultralow-threshold raman laser using a spherical dielectric microcavity," *Nature*, vol. 415, pp. 621–623, 2002.

[49] I. S. Grudinin, H. Lee, O. Painter, and K. J. Vahala, "Phonon laser action in a tunable two-level system," *Phys. Rev. Lett.*, vol. 104, no. 8, p. 083901, 2010.

[50] R. P. Beardsley, A. V. Akimov, M. Henini, and A. J. Kent, "Coherent terahertz sound amplification and spectral line narrowing in a stark ladder superlattice," *Phys. Rev. Lett.*, vol. 104, no. 8, p. 085501, 2010.

[51] M. Bennett, M. F. Schatz, H. Rockwood, and K. Wiesenfeld, "Huygens's clocks," *Proc. R Soc. A*, vol. 458, p. 563, 2002.

[52] A. S. Pikovsky, M.G. Rosenblum, and J. Kurths, *Synchronization - A Universal Concept in Nonlinear Sciences*. Cambridge, England: Cambridge University Press, 2001.

[53] A. T. Winfree, *The Geometry of Biological Time*. New-York: Springer, 1980.

[54] R. Wilders and H. J. Beating, "Beating irregularity of single pacemaker cells isolated from the rabbit sinoatrial node," *Biophys. J.*, vol. 65, no. 6, pp. 2601–2613, 1993.

[55] M. Abel, K. Ahnert, and S. Bergweiler, "Synchronization of sound sources," *Phys. Rev. Lett.*, vol. 103, no. 11, p. 114301, 2009.

[56] K. Kurokawa, "Injection locking of microwave solid-state oscillators," *Proc. of the IEEE*, vol. 61, no. 10, pp. 1386–1410, 1973.

[57] M. Hossein-Zadeh and K. J. Vahala, "Observation of injection locking in an optomechanical rf oscillator," *Appl. Phys. Lett.*, vol. 93, no. 19, p. 191115, 2008.

[58] H. L. Stover and W. H. Steier , "Locking of laser oscillators by light injection," *Appl. Phys. Lett.*, vol. 8, no. 4, p. 91, 1966.

[59] R. Adler, "A study of locking phenomena in oscillators," *Proc. of the IRE*, vol. 34, no. 6, pp. 351–357, 1946.

[60] M. Drewsen, A. Mortensen, R. Martinussen, P. Staanum, and J. L. Sørensen, "Nondestructive identification of cold and extremely localized single molecular ions," *Phys. Rev. Lett.*, vol. 93, p. 243201, 2004.

[61] H. J. Mamin and D. Rugar, "Sub-attonewton force detection at millikelvin temperatures," *Appl. Phys. Lett.*, vol. 79, p. 3358, 2001.

[62] R. Maiwald, D. Leibfried, J. Britton, J. C. Bergquist, G. Leuchs, and D. J. Wineland, "Stylus ion trap for enhanced access and sensing," *Nat. Phys.*, vol. 5, p. 551, 2009.

[63] M. J. Biercuk, H. Uys, J. Britton, A. P. VanDevender, and J. J. Bollinger, "Ultrasensitive detection of force and displacement using trapped ions," *Nat. Nanotech.*, vol. 5, pp. 646–650, 2010.

[64] F.C. Witteborn and W.M. Fairbank, "Experimental comparison of the gravitational force on freely falling electrons and metallic electrons," *Phys. Rev. Lett.*, vol. 19, p. 1049, 1967.

[65] L. Deslauriers, S. Olmschenk, D. Stick, W. K. Hensinger, J. Sterk, and C. Monroe, "Scaling and suppression of anomalous heating in ion traps," *Phys. Rev. Lett.*, vol. 97, no. 10, p. 103007, 2006.

[66] D. Rugar, R. Budakian, H. J. Mamin, and B. W. Chui, "Single spin detection by magnetic resonance force microscopy," *Nature*, vol. 430, p. 329, 2004.

[67] H. J. Mamin, M. Poggio, C. L. Degen, and D. Rugar, "Nuclear magnetic resonance imaging with 90-nm resolution," *Nat. Nanotech.*, vol. 2, p. 301, 2007.

[68] C. Degen, "Microscopy with single spins," *Nat. Nanotech.*, vol. 3, p. 643, 2008.

[69] D. Offenberg, C. B. Zhang, Ch. Wellers, B. Roth, and S. Schiller, "Translational cooling and storage of protonated proteins in an ion trap at subkelvin temperatures," *Phys. Rev. Lett.*, vol. 78, no. 6, p. 061401, 2008.

[70] R. A. Haberstroh, T. I. Moran, and S. Penselin, "Direct measurement of the nuclear magnetic dipole moment of ^{165}Ho with the atomic beam magnetic resonance method," *Z. Phys.*, vol. 252, pp. 421–427, 1972.

[71] P. T. Callaghan, M. Kaplan and N. J. Stone, "The magnetic dipole moment of ^{55}Co," *Nucl. Phys. A*, vol. 201, pp. 561–569, 1973.

[72] W. Ansbacher, Y. Li, and E. H. Pinnington, "Precision lifetime measurement for the 3p levels of mg ii using frequency-doubled laser radiation to excite a fast ion beam," *Phys. Lett. A*, vol. 139, p. 165, 1989.

[73] G. Audi and A. H.Wapstra, "The 1993 atomic mass evaluation : (i) atomic mass table," *Nucl. Phys.*, vol. 565, pp. 1–65, 1993.

[74] R. B. Firestone, *Table of Nuclides*. New York: Wiley, 8 ed., 1996.

Danksagung

Zuerst bedanke ich mich bei Herrn Prof. Theodor W. Hänsch für das Vertrauen, das tolle Umfeld, seine Leidenschaft für die Physik und die brillanten Ideen.

Prof. Hermann Gaub will ich für die Erstellung des Zweitgutachtens danken.

Thomas Udem hat herausragend zur Perfektion all der während meiner Zeit in Garching angegangenen Projekte beigetragen und mich immer wieder durch seine Begeisterung für die Physik im allgemeinen und der Programmiererei im speziellen motiviert.

Maximilian Herrmann hat durch seine Ideen, Geduld, Sprachkunst und seinen Optimismus außerordentlich zu dieser Arbeit beigetragen.

Ohne meinen engsten Mitstreiter und geschätzten Freund Valentin Batteiger wäre das ganze wohl nicht möglich gewesen. Deine Obsession für Physik und Laser ebenso wie deine Arbeit und Ideen waren mit ausschlaggebend für das gelingen dieser Arbeit. Ich hoffe du hast genau soviel Spaß gehabt wie ich.

Guido Saathoff hat durch seine Kompetenz und Erfahrung zur Lösung vieler Probleme beigetragen. Camille Estienne war immer für eine Diskussion im Labor zu haben.

Janis Alnis möchte ich für seine Hilfe beim Design und Aufbau der Referenzcavity und seiner Inspiration zu einer spielerischen Herangehensweise an die hier auftretenden Probleme danken.

Besonders hervorheben möchte ich auch die Mitarbeit von Helmut Brückner, Wolfgang Simon und Karl "Charly" Linner die mit ihrem umfangreichen Schatz an Wissen und Erfahrungen vieles erst möglich gemacht haben.

Das Organisationstalent von Ingrid Hermann und Gabriele Gschwendtner hat es mir ermöglicht, mich ganz auf meine Arbeit zu konzentrieren und Schaden von mir abgewendet.

Ich möchte mich bei allen bedanken die außerdem zu dieser Arbeit beigetragen haben Masaki Hori, Ronald Holzwarth, Tobias Wilken und Birgitta Bernhard.

Michael Krüger, John Breuer und Takuro Ideguchi danke ich für die "groß"artige Bürogemeinschaft.

Dem Team Ringberg-Express (Andreas Vernaleken, Jim Bergquist, Thomas Udem und Akira Ozawa) möchte ich für die Begeisterung an der Radfahrerei danken.

Dank meiner großartigen Kollegen der AG Hänsch und vielen anderen am MPQ werde ich den Aufenthalt hier immer in positiver Erinnerung behalten.

Zuletzt möchte ich für die Unterstützung durch meine Freunde und Familie danken.